

8-2018

A Pseudo-rigorous LiDAR System Calibration Approach and a Strategy for Stability Analysis

Megan M.G. Miller
Purdue University

Follow this and additional works at: https://docs.lib.purdue.edu/open_access_dissertations

Recommended Citation

Miller, Megan M.G., "A Pseudo-rigorous LiDAR System Calibration Approach and a Strategy for Stability Analysis" (2018). *Open Access Dissertations*. 2026.
https://docs.lib.purdue.edu/open_access_dissertations/2026

This document has been made available through Purdue e-Pubs, a service of the Purdue University Libraries.
Please contact epubs@purdue.edu for additional information.

**A PSEUDO-RIGOROUS LIDAR SYSTEM CALIBRATION
APPROACH AND A STRATGEY FOR STABILITY ANALYSIS**

by

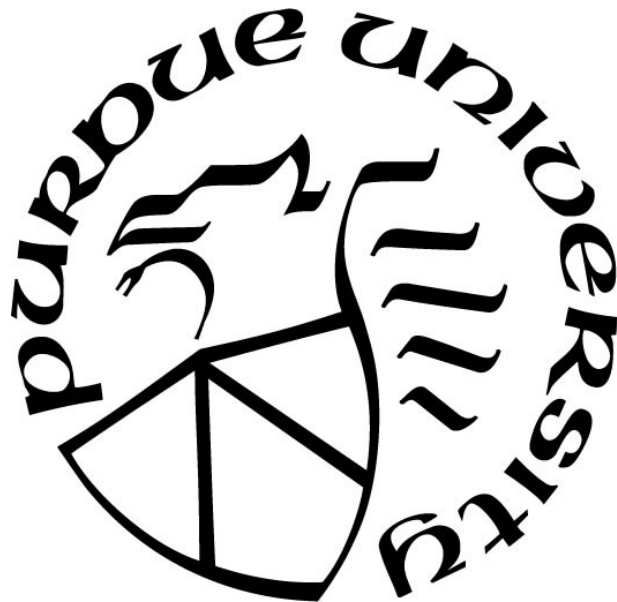
Megan M. G. Miller

A Dissertation

Submitted to the Faculty of Purdue University

In Partial Fulfillment of the Requirements for the degree of

Doctor of Philosophy



Department of Civil Engineering

West Lafayette, Indiana

August 2018

**THE PURDUE UNIVERSITY GRADUATE SCHOOL
STATEMENT OF DISSERTATION APPROVAL**

Dr. Ayman Habib, Chair

Lyles School of Civil Engineering

Dr. James Bethel

Lyles School of Civil Engineering

Dr. Melba Crawford

Lyles School of Civil Engineering

Dr. Henry Theiss

Integrity Applications Incorporated

Approved by:

Dr. Dulcy Abraham

Head of the Departmental Graduate Program

ACKNOWLEDGMENTS

It is important to me to acknowledge my advisor, mentors, friends, and family for being with me and supporting me throughout my Ph.D. journey. I am profoundly grateful for my advisor, Dr. Ayman Habib. His attentiveness to the many dynamics of our research group and each individual student's progress as a researcher and as a professional is unmatched. I would not have been able to produce the work here without his guidance, clarity, and support.

I am also very fortunate to have had several mentors who helped me to broaden my goals and deepen my understanding of Geomatics; namely, Dr. Edward Mikhail, Dr. Henry Theiss, Dr. Melba Crawford, Dr. Jim Bethel, Professor Carl Shangraw, and Nathaniel Ovans.

Finally, I would like to acknowledge my mother Lisa Start-Spinner for being my number one fan, my brother Jared Miller and best friend Niccole Erickson for their companionship in my studies, as well as my fiancé and dearest friend Dr. Guido Ritelli for his never-ending support.

TABLE OF CONTENTS

LIST OF TABLES	vi
LIST OF FIGURES	ix
LIST OF ACRONYMS	xi
1. INTRODUCTION	1
1.1 Background	1
1.2 Challenges in LiDAR System Calibration	2
1.3 Research Objectives	3
1.4 Dissertation Outline.....	5
2. LITERATURE REVIEW	6
2.1 Overview	6
2.2 Generation of LiDAR Point Clouds	6
2.1 Quality Assurance (QA) and Quality Control (QC) of LiDAR Mapping.....	12
2.2 LiDAR System Calibration and Stability Analysis Background	15
2.3 Strategy of LiDAR System Calibration	19
2.3.1 Theoretical Basis of LiDAR Calibration	19
2.3.2 LiDAR Data Collection Strategy.....	22
2.3.3 Calibration Primitives.....	31
2.4 System Calibration Procedures	35
2.4.1 Rigorous (<i>R</i>) LiDAR System Calibration.....	35
2.4.2 Pseudo-rigorous LiDAR System Calibration	38
2.4.2.1 Quasi-Rigorous (<i>QR</i>) Calibration Procedures	39
2.4.2.2 Simplified (<i>S</i>) Calibration Procedures	43
2.4.3 Rigorous and Pseudo-rigorous Calibration Strategies.....	60
3. METHODOLOGY FOR ADDRESSING RESEARCH OBJECTIVES.....	62
3.1 Overview	62
3.2 Quasi-Rigorous/Quasi-Simplified (<i>QRQS</i>) Calibration	62
3.2.1 Assumptions and Math Model.....	63
3.2.2 Synthesizing Raw Measurements	67
3.2.3 Calibration Strategy	69
3.3 LiDAR System Calibration Stability Analysis.....	70

3.3.1	Stability Analysis Overview	71
3.3.2	Stability Analysis Strategy	72
4.	RESULTS OF THE QUASI-RIGOROUS/QUASI-SIMPLIFIED (QRQS) CALIBRATION AND STABILITY ANALYSIS	77
4.1	Overview	77
4.2	Results of the Quasi-Rigorous/Quasi-Simplified (<i>QRQS</i>) Calibration using a UAV based LiDAR System.....	77
4.2.1	Platform and Sensors	77
4.2.2	Calibration Results and their Quantitative and Qualitative Comparison with Existing Calibration Approaches	81
4.3	Performance of the Quasi-Rigorous/Quasi-Simplified (<i>QRQS</i>) Approach and Existing Calibration Approaches Before and After Deviating from their Assumptions	85
4.3.1	Rigorous Data Simulation.....	86
4.3.2	Deviating from the Parallel Flight Lines Assumption.....	89
4.3.3	Performance of the Quasi-Rigorous/Quasi-Simplified (<i>QRQS</i>) Calibration with Non-Parallel Flight Lines	91
4.3.4	Deviating from the Low Terrain Relief Assumption.....	93
4.3.5	Deviating from the Vertical Scanner Assumption.....	95
4.3.6	Investigating the Number of Control Points.....	99
4.3.7	Summary of Performance Tests.....	103
4.4	Results of the Stability Analysis	103
4.4.1	Stable Stability Analysis Results	104
4.4.2	Unstable Stability Analysis Results.....	105
5.	CONCLUSIONS, CONTRIBUTIONS, AND RECOMMENDATIONS FOR FUTURE WORK.....	108
5.1	Research Conclusions	108
5.2	Research Contributions	109
5.3	Recommendations for Future Work.....	112
	REFERENCES	114

LIST OF TABLES

Table 2-1: Impact of System Parameter Biases on Each Component of the Reconstructed Coordinate (Habib et al., 2009a).....	26
Table 2-2: Biases that Impact the <i>X</i> Coordinate and their Dependencies.....	27
Table 2-3: Biases that Impact the <i>Y</i> Coordinate and their Dependencies.....	28
Table 2-4: Biases that Impact the <i>Z</i> Coordinate and their Dependencies.....	28
Table 4-1: Uncertainty of the LiDAR System Measurements.....	80
Table 4-2: Results for the <i>16-beam R</i> , <i>1-beam R</i> , <i>S</i> , <i>QR</i> , and <i>QRQS</i> Approaches using the VLP-16 PUCK Hi-Res LiDAR on a UAV Platform	82
Table 4-3: Qualitative Analysis of Point Cloud Coordinates on the North-South (N-S) and East-West (E-W) Huts Before Calibration and After Calibration for the <i>16-beam R</i> , <i>1-beam R</i> , <i>S</i> , <i>QR</i> , and <i>QRQS</i> Approaches.....	83
Table 4-4: RMSE of the Difference between Adjusted/Reconstructed Coordinates from each Calibration Approach and the Reconstructed Coordinates from the <i>16-beam R</i>	85
Table 4-5: Uncertainty of the LiDAR System Components for Simulated Data	87
Table 4-6: Configuration of Strip-pairs for Simulated Data.....	87
Table 4-7: Evaluated Accuracy (RMSE of Differences between True & Bias-Free Coordinates) and Expected Accuracy (via Error Propagation) at Various Scan Angles	89
Table 4-8: The Estimated <i>S</i> Calibration Parameters with Parallel and Non-Parallel Flight Lines.....	90
Table 4-9: RMSE Analysis of <i>S</i> Calibration Results with Parallel and Non-Parallel Flight Lines.....	91
Table 4-10: The Estimated <i>QRQS</i> Calibration Parameters with Parallel and Non-Parallel Flight Lines	92
Table 4-11: RMSE Analysis of <i>QRQS</i> Calibration Results with Parallel and Non-Parallel Flight Lines	92
Table 4-12: The Estimated <i>S</i> Calibration Parameters Before and After Deviation from the Low Terrain Relief Assumption	93

Table 4-13: RMSE Analysis of the S Calibration Procedure Before and After Deviation from the Low Terrain Relief Assumption.....	94
Table 4-14: The Estimated S Calibration Parameters Before and After Deviation from the Vertical Scanner Assumption	96
Table 4-15: RMSE Analysis of the S Calibration Procedure Before and After Deviation from the Vertical Scanner Assumption.....	96
Table 4-16: The Estimated QR Calibration Parameters Before and After Deviation from the Vertical Scanner Assumption.....	97
Table 4-17: RMSE Analysis of the QR Calibration Procedure Before and After Deviation from the Vertical Scanner Assumption.....	97
Table 4-18: The Estimated QRQS Calibration Parameters Before and After Deviation from the Vertical Scanner Assumption.....	98
Table 4-19: RMSE Analysis of the QRQS Calibration Procedure Before and After Deviation from the Vertical Scanner Assumption	98
Table 4-20: QR Calibration Results While Varying the Number of Control Points	99
Table 4-21: RMSE Analysis of QR Calibration Results While Varying the Number of Control Points	100
Table 4-22: QRQS Calibration Results While Varying the Number of Control Points .	100
Table 4-23: RMSE Analysis of QRQS Calibration Results While Varying the Number of Control Points	101
Table 4-24: R Calibration Results While Varying the Number of Control Points	101
Table 4-25: RMSE Analysis of R Calibration Results While Varying the Number of Control Points	102
Table 4-26: Calibration Results from Hypothetical Times.....	104
Table 4-27: Stability Analysis RMSE Values of all Point Clouds from a Stable LiDAR System.....	104
Table 4-28: Stability Analysis RMSE Values of Individual Point Clouds from a Stable LiDAR System.....	105
Table 4-29: Stability Analysis RMSE Values of all Point Clouds from an Unstable LiDAR System.....	106

Table 4-30: Stability Analysis RMSE Values of Individual Point Clouds from an Unstable LiDAR System.....	106
Table 5-1: Calibration Rigor Score of Existing Calibration Approaches (Red) and the New <i>Quasi-Rigorous/Quasi-Simplified</i> Approach (Blue)	110

LIST OF FIGURES

Figure 2.1: Coordinate Systems and Vectors in the LiDAR Point-Positioning Equation (adapted from Habib et al., 2008)	8
Figure 2.2: The Laser beam (lb) Coordinate System with Respect to the Laser unit (lu) Coordinate System at Various α and β Scan Angles	12
Figure 2.3: LiDAR System Calibration Strategy to Minimize Discrepancies between Overlapping Point Clouds (a) and Control Surfaces (b) (adapted from Bang, 2010)	21
Figure 2.4: Laser unit Coordinates and their Relation to the Range and Mirror Angle Measurements	24
Figure 2.5: Illustration of the Flying Direction Dependent Terms, (βt , $\sin(\beta t)$), and $x(t)$), other than the Double Signage Term.....	29
Figure 2.6: Optimal/Minimal Flight Configuration for Airborne LiDAR System Calibration (adapted from Bang, 2010)	31
Figure 2.7: Point-patch Pair	32
Figure 2.8: Formation of the uvw Modified Coordinate System for ICPatch Weight Modification (adapted from Bang, 2010)	34
Figure 2.9: Synthesizing the System Raw Measurements for the QR Calibration Procedure (adapted from Bang, 2010)	43
Figure 2.10: An Object Point and its Measurements Observed from the Two Different Scenarios of Overlapping Strips flown in Opposite Directions (A & B_L , A & B_R) (adapted from Bang, 2010)	49
Figure 2.11: An Object Point and its Measurements Observed from Overlapping Strips Flown in the Same Direction (adapted from Bang, 2010)	54
Figure 2.12: Implementation of the R , QR , and S Calibration Procedures	61
Figure 3.1: Minimum Bounding Rectangle Procedure for Determining Flight Direction	68
Figure 3.2: Synthesizing the System Raw Measurements for the QRQS Calibration Procedure	68
Figure 3.3: Workflow of the QRQS Calibration Procedure	70

Figure 3.4: Workflow of the Stability Analysis Procedure for the R Calibration Approach	73
Figure 3.5: Workflow of the Stability Analysis Strategy for the <i>Pseudo-rigorous</i> Calibration Approaches	74
Figure 4.1: Alignment of Original and Virtual Coordinate Systems on the UAV LiDAR System used in this Analysis	78
Figure 4.2: Flight Trajectories and Test Field Containing Geometric Targets (huts) as seen in 3D Point Clouds and Orthophoto	80
Figure 4.3: Orientation of VLP-16 PUCK Hi-Res Laser Beams.....	81
Figure 4.4: Simulated Point Clouds and Trajectories Deviated from Being Parallel by 30° (planimetric view).....	86
Figure 5.1: Requirements vs Rigors Score of the New and Existing Calibration Methods	111

LIST OF ACRONYMS

GNSS	Global Navigation Satellite System
EQC	External Quality Control
IMU	Inertial Measurement Unit
INS	Inertial Navigation System
IQC	Internal Quality Control
QA	Quality Assurance
QC	Quality Control
QR	Quasi-Rigorous
QRQS	Quasi-Rigorous/Quasi-Simplified
R	Rigorous
RMSE	Root-Mean-Square Error
S	Simplified
UAV	Unmanned Aerial Vehicle

ABSTRACT

Author: Miller, Megan, M.G. PhD

Institution: Purdue University

Degree Received: August 2018

Title: A Pseudo-rigorous LiDAR System Calibration Approach and a Strategy for Stability Analysis.

Major Professor: Ayman Habib

With LiDAR systems being a crucial technology for near real-time mapping and spatial analysis, the user community needs standardized LiDAR system calibration procedures that are robust for the wide range of users and scenarios. More specifically, a comprehensive calibration approach should entail rigor in automation for matching and handling the irregularity of LiDAR data, as well as generality in terms of type of terrain used and of raw measurement availability. Most times, the sensor model and raw measurements are unavailable to the end user, and therefore *rigorous* LiDAR system calibration is not possible. For this scenario, *pseudo-rigorous* methods have been developed that synthesize the raw measurements from the point cloud (and in some cases the trajectory) using certain assumptions (e.g. parallel flight lines). This work introduces a new *pseudo-rigorous* calibration approach called the *Quasi-Rigorous/Quasi-Simplified*. The existing *pseudo-rigorous* approaches include the *Simplified* and *Quasi-Rigorous*. The *Quasi-Rigorous/Quasi-Simplified* approach requires less raw measurements than the *Quasi-Rigorous* and it can be used for any type of terrain and can incorporate control unlike the *Simplified* approach. In addition to this new calibration approach, there is a performance analysis to test the robustness of the new and existing *pseudo-rigorous* approaches in non-ideal conditions, as well as a stability analysis strategy to analyze LiDAR system calibration results from two different dates. The stability analysis strategy quantifies the variation in system parameters over time and serves as an important Quality Assurance tool for consistently producing accurate point clouds throughout the lifespan of a LiDAR mapping system. The experimental results show the successful implementation of the new *Quasi-Rigorous/Quasi-Simplified* approach with real and simulated data and compares the results with existing *rigorous* and *pseudo-rigorous* approaches. After inspecting the point cloud alignment and adjusted coordinates, it was shown that the *Quasi-Rigorous/Quasi-Simplified* approach is successful in significantly reducing the impact of systematic errors

even though it makes several assumptions. Also, when compared to the existing *Simplified* and *Quasi-Rigorous pseudo-rigorous* approaches, the *Quasi-Rigorous/Quasi-Simplified* approach provides maximum capability while maintaining minimal assumptions and no requirements for raw measurements. In the performance analysis, it was shown that the *Quasi-Rigorous/Quasi-Simplified* and existing *pseudo-rigorous* calibration approaches are robust under non-ideal conditions, and a 52-100 *Percent Improvement* was observed even in the extreme cases. Using simulated data, the stability analysis results show how to implement the strategy as a Quality Assurance tool given a stable and an unstable stability analysis outcome. In addition to this, the new calibration approach, and the previous *pseudo-rigorous* calibration approaches, were successfully used to calibrate a multi-beam spinning LiDAR (VLP-16). This has not previously been done since the *pseudo-rigorous* calibration methods are developed specifically for single-beam linear scanning LiDAR systems.

1. INTRODUCTION

1.1 Background

Airborne light detection and ranging (LiDAR) systems are now a prominent tool for direct acquisition of accurate dense point clouds. A LiDAR system refers to the laser-ranging and integrated direct geo-referencing units. The direct geo-referencing unit integrates a Global Navigation Satellite System (GNSS) and an Inertial Navigation System (INS) to provide the platform position and orientation at a high frequency. In addition to each component of the LiDAR system having had many advances in the past decade, airborne platforms used for data collection have had significant advances and changes. Altogether, this progress has accelerated the growing use and application of LiDAR systems because they are now more accurate, readily available, and not as costly. With the large user community and its continual increase, development of standard operating procedures for LiDAR system calibration will ensure that the systems consistently meet industry standards. LiDAR system calibration accurately decouples and estimates system parameters, thus minimizing the impact of systematic errors on the resulting point cloud. The calibration process requires a rigorous mathematical model that relates all system parameters and measurements from each system component in order to calculate ground coordinates. In addition to that, the model should include parameters that account for systematic errors within the LiDAR system. There are several different approaches to LiDAR system calibration; their strategies differ vastly and none of them simultaneously address all of the inherent challenges that arise when working with LiDAR mapping systems. Most times, *rigorous* LiDAR system calibration is not possible because the raw measurements are unavailable, and *pseudo-rigorous* approaches that synthesize the raw measurements from the point cloud (and in some cases the trajectory) are used. The topic of stability analysis of LiDAR system calibration in the LiDAR community is yet to be addressed and is very timely now that systems are becoming more compact and readily available.

1.2 Challenges in LiDAR System Calibration

LiDAR system calibration compares overlapping point clouds and control information in order to reduce or remove the impact of systematic errors on the resulting point cloud. There are various ways to approach calibration, and they are all driven by the absence or availability of raw measurements (the raw measurements being referred to are the integrated GNSS/INS position and orientation information, and the LiDAR unit measurements of two angles and a range). The existing approaches to eliminate and/or reduce the effect of systematic errors are categorized as either system-driven (calibration) or data-driven (strip adjustment). System-driven approaches are superior because they constrain point cloud reconstruction to the geometric relationship that exists between the GNSS/INS unit, LiDAR scanning mechanism, and ground coordinate of the LiDAR footprint (i.e. the sensor model). While system-driven approaches preserve the link to the sensor model, data-driven approaches arbitrarily fit data strips together through a transformation model that may not scale appropriately to the entire dataset. The data-driven approaches for eliminating discrepancies are never a suitable substitute to using system-driven procedures, but they are sometimes employed because the end user does not have access to the raw measurements. Typically, the data provider has sole access to the raw measurements and their LiDAR system calibration is sometimes considered a trade secret. Overall, there is a need for standardized LiDAR system calibration procedures which are system-driven even in the absence of raw measurements and are also general for the wide range of users.

Another challenge in LiDAR system calibration arises from the irregular nature of LiDAR data and in the primitive selection for comparing overlapping strips. With irregular data, distinct control and tie points are not easily identifiable making it more difficult to preserve the link to the sensor model therefore that link is often sacrificed, and the procedure is no longer system-driven. Although distinct points are not readily available in LiDAR data, points are generally a superior primitive choice (as opposed to lines or planes) in calibration since the goal of calibration is to refine the system parameters of the sensor model. The only time this is not true is when the unknown parameters of interest are extended to include the parameters defining such primitives (but this is not often the case).

There have been various types of system-driven calibration approaches developed that appropriately handle the irregularity of LiDAR data, but many have an unfavorable reliance on control surfaces (as opposed to using overlapping strips), urban settings, manual operations, and/or preprocessing of data to extract certain linear/planar features. These dependencies and limitations have to do with the overall strategy of the calibration algorithm, and an ideal algorithm will have automated procedures and minimal requirements for control and urban settings. Also, some of the existing approaches have chosen to only focus on the angular biases found in the boresight rotation matrix defining the orientation of the LiDAR unit with respect to the IMU body frame. These approaches that focus on angular biases are important developments because these boresight biases tend to have the largest impact on the resulting point cloud, but it is not a complete solution to the other biases that might be present in the LiDAR system. Overall, a LiDAR system calibration approach that simultaneously addresses the inherent challenges along with an automated strategy and minimum dependencies on control and type of terrain cover is non-existent.

1.3 Research Objectives

The following research objectives address the need of the LiDAR mapping community for a comprehensive, standardized LiDAR system calibration approach which simultaneously addresses the inherent challenges. The objectives include the development of a new calibration strategy, a performance analysis of *pseudo-rigorous* approaches, and development of a strategy for performing a stability analysis on LiDAR system parameters.

- Develop a new calibration approach that is generic for the many types of users and holds the following characteristics:
 - Operates without access to raw measurements,
 - Uses point primitives to preserve the link to the sensor model,
 - Has an automated procedure that accounts for the irregularity of LiDAR point clouds,

- Has a reliance on overlapping strips instead of expensive control surfaces,
 - Is ground cover independent (does not require urban settings with various geometric shapes from buildings and other man-made features),
 - Estimates all system parameters; which includes both the linear and angular mounting parameters as well as the internal characteristics of the LiDAR unit, and
 - Is able to incorporate control into the calibration math model.
- Assess the performance of the new and existing *pseudo-rigorous* approaches under non-ideal conditions that deviate from the underlying assumptions of their respective math models. More specifically, the analysis will individually inspect each deviation from an assumption with the following assessments:
 - Side by side comparison of the estimated system parameters/biases before and after deviating from the specific assumption,
 - RMSE of the difference between the resulting point cloud coordinates and true coordinates for the following 4 cases:
 - Non-deviated, before calibration,
 - Non-deviated, after calibration,
 - Deviated, before calibration,
 - Deviated, after calibration, and
 - Quantify the percent improvement after calibration for the non-deviated and deviated scenario to understand the impact that the non-ideal scenario has on the ability of the calibration algorithm to improve the accuracy of the data.
- Develop a stability analysis strategy which can be utilized as a QA tool for consistent production of accurate point clouds over the lifespan of a LiDAR mapping system. The developed stability analysis strategy will have the following characteristics:
 - Quantifies variation of system parameters over time,
 - Guides the process of determining optimal calibration frequency, and

- Operates with or without access to raw measurements (by synthesizing the measurements in the latter case).

1.4 Dissertation Outline

Chapter 2 contains the literature review and provides the background information pertaining to the above research objectives. First, the details of LiDAR point cloud generation are discussed. Then, there is a discussion on QA procedures to be taken before data collection, as well as the QC procedures after collection. This leads into the background of LiDAR system calibration; then the strategy of LiDAR calibration algorithms is discussed in terms of the theoretical basis, the data collection strategy, and the primitives. Then, *rigorous* and *pseudo-rigorous* calibration approaches are discussed and derived with a focus on the ones to which the *Quasi-Rigorous/Quasi-Simplified (QRQS)* experimental results will be compared. Chapter 3 introduces the methodology for addressing the research objectives. For the new *QRQS* calibration approach, the assumptions are detailed and development of the math model follows from those assumptions. Then, the details of the methods used to synthesize the raw measurements and of the calibration strategy are discussed. For the stability analysis strategy, first, the general outline for both the *rigorous* and *pseudo-rigorous* calibration approaches is explained. Then, steps involved for synthesizing the raw measurements in the *pseudo-rigorous* stability analysis are detailed. Finally, the stability analysis strategy is covered. Chapter 4 shows the experimental results of the new calibration approach, the performance analysis, and the application of the stability analysis strategy. Chapter 5 provides the conclusions, research contributions, and recommendations for future work.

2. LITERATURE REVIEW

2.1 Overview

There are numerous research efforts that address the topic of Quality Assurance (QA) and Quality Control (QC) for point clouds derived from LiDAR systems. Although all of the QA and QC steps are important to ensure accurate point clouds, calibration is the most prominent and is extremely important in order to ensure positional accuracy of the final product. The existing approaches for LiDAR system calibration and the many processes entailed within it will be covered in the following sections. Before getting to the specific discussion of calibration, there is a review on the generation of LiDAR point clouds and then an overview of all the QA and QC procedures.

2.2 Generation of LiDAR Point Clouds

The laser unit emits a laser pulse, records the amount of time that pulse takes to reflect off of a surface and return to the unit, and then it calculates a range based on that time. The laser ranging theorem, detailed physical principles, and fundamental concepts are well documented in Baltsavias (1999). This type of laser ranging system is classified as a time-of-flight (ToF) unit; there are also triangulation based laser ranging units that do not use the time-of-flight (Wehr and Lohr, 1999), but these types of lasers will not be discussed here. The distance calculated is between the laser beam firing point and the footprint on the ground. The footprint is where the laser beam hits the surface of the scanned object. The scan pattern of a laser unit is either linear or elliptical depending on the mechanics of the unit. For airborne LiDAR systems, the scanning mirror motion in addition to the forward motion of the platform effectively scans a strip of land below. Some LiDAR systems (e.g. from commercial providers such as OpTech, RIEGL, LEICA) have a full waveform digitizer that records several returns from the emitted pulse, as opposed to only gathering the last return from the emitted pulse. These types of LiDAR systems are useful for mapping scenes such as tree canopies because the laser is able to penetrate through the canopy level and has multiple returns before the last return (Shan and Toth, 2009).

Specifications of the LiDAR collection are chosen carefully because they have the potential to affect both the positional accuracy and the accuracy of the recorded intensity value. The vertical accuracy of LiDAR point cloud coordinates is better (e.g., smaller RMSE) than the horizontal accuracy (Filin, 2001), and is actually quite accurate when compared to other mapping approaches (May and Toth, 2007). Accuracy values are affected by many factors, which include the accuracy of the GNSS/INS position and orientation integration process, and the accuracy of the system parameters (depends on whether or not they have been derived through a rigorous calibration). The intensity information that is associated with each point is the ratio between the strength of the reflected light and the emitted light (Coren and Sterzai, 2006). LiDAR intensity data is heavily dependent on the reflectance properties of the object and is usually used for some post-processing activities such as segmentation and classification (Wang and Tseng, 2004). Although the validity of the intensity information is usually a concern of the laser unit manufacturer, some calibration solutions use intensity values to facilitate calibration (Ravi et al., 2018). Habib et al. (2011) provides research on the intensity correction and evaluation process. The point density is also an important factor which is dependent on the LiDAR specifications because it determines the level of detail an object will have in the final dataset.

The common approach to determine the coordinate values of each LiDAR pulse involves many coordinate systems and is well documented in Habib et al. (2009a) and Shan and Toth (2009). The coordinate systems involved in LiDAR data collection are discussed before deriving the math model that relates all system parameters and measurements to the ground coordinate. The notation of spatial offsets and rotations are detailed below in order to clearly denote with what coordinate systems they are affiliated.

- a) \mathbf{r}_a^b , a 3 x 1 vector, denotes the spatial offset between point \mathbf{a} and point \mathbf{b} . When point \mathbf{a} is the origin of a coordinate system, \mathbf{r}_a^b represents the coordinates of that origin expressed in terms of coordinate system \mathbf{b} as a reference
- b) \mathbf{R}_a^b , a 3 x 3 matrix, denotes the rotational matrix to apply in order to transform from coordinate system \mathbf{a} to coordinate system \mathbf{b}

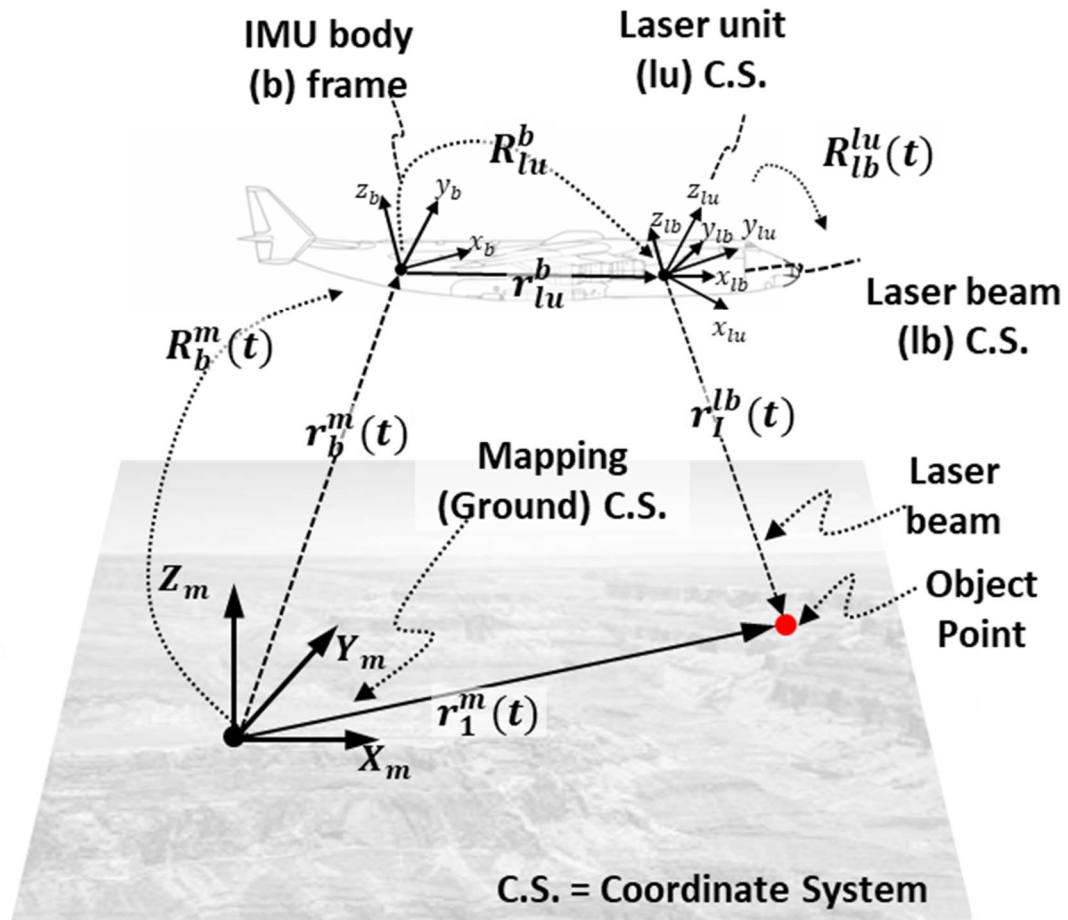


Figure 2.1: Coordinate Systems and Vectors in the LiDAR Point-Positioning Equation
(adapted from Habib et al., 2008)

As can be seen in Figure 2.1, the LiDAR point-positioning equation involves four coordinate systems and they include the laser beam coordinate system, the laser unit coordinate system, the Inertial Measurement Unit (IMU) body frame, and the mapping coordinate system.

a) Laser beam coordinate system (lb):

- The laser beam firing point is the origin of this coordinate system.
- The laser beam extends from the firing point to the laser beam footprint, and the z-axis of lb is aligned along the laser beam.

- If the z-axis positive direction is in the same direction of the laser beam, then the coordinates of object point I in this coordinate system are represented as eq. (2.1).
- If the z-axis positive direction is in the opposite direction of the laser beam, then the coordinates of object point I in this coordinate system are represented as eq. (2.2).
- The positive y-axis is nominally in the flight direction. If the positive z-axis is nominally in up direction, then the positive x-axis is nominally aligned with the across-flight direction such that the system is a right handed coordinate system. This configuration can be seen in Figure 2.2 (a).
- $r_I^{lb}(t)$ is time dependent. As the system scans, the range between the laser beam firing point and point I will change.

$$r_I^{lb}(t) = \begin{bmatrix} 0 \\ 0 \\ \rho(t) \end{bmatrix} \quad (2.1)$$

$$r_I^{lb}(t) = \begin{bmatrix} 0 \\ 0 \\ -\rho(t) \end{bmatrix} \quad (2.2)$$

b) Laser unit coordinate system (lu):

- The origin of this coordinate system is at the laser beam firing point, which is the same as the laser beam coordinate system, which is at the laser beam firing point.
- The positive y-axis is nominally aligned along the flying direction, and the positive z-axis points nominally in the up direction. Therefore, the x-axis is aligned nominally along the across-flight direction such that the system is a right handed coordinate system. This configuration can be seen in Figure 2.2 (a).

- The rotational matrix, $\mathbf{R}_{lb}^{lu}(t)$, characterizes the scanning direction at a single point in time.
- For system with a steering mirror, $\mathbf{R}_{lb}^{lu}(t)$ is defined by the values from the encoders on the the mirror steering mechanism. If it is an elliptical system, then it requires two rotation angles ($\alpha(t), \beta(t)$); $\mathbf{R}_{lb}^{lu}(t)$ for this scenario is defined in eq. (2.3). The angle of rotation around the x-axis of the laser unit coordinate system is $\alpha(t)$, and the angle of rotation around the once rotated y-axis of the laser unit coordinate system is $\beta(t)$. The relationship between the laser beam and laser unit coordinate systems with $\alpha(t)$ and $\beta(t)$ scan angles can be seen in Figure 2.2 (b) and (c), respectively. If it is a linear system, then just one rotation angle is required ($\beta(t)$) to define $\mathbf{R}_{lb}^{lu}(t)$ because there will be no rotation about the x-axis, the $\alpha(t)$ angle will be equal to zero.
- Eq. (2.4) defines the coordinates of point I relative to the laser unit coordinate system.
- $\mathbf{R}_{lb}^{lu}(t)$ is time dependent since the scanning direction is continuously changing.

$$\mathbf{R}_{lb}^{lu}(t) = \begin{bmatrix} 1 & 0 & 0 \\ 0 & \cos(\alpha(t)) & -\sin(\alpha(t)) \\ 0 & \sin(\alpha(t)) & \cos(\alpha(t)) \end{bmatrix} \begin{bmatrix} \cos(\beta(t)) & 0 & \sin(\beta(t)) \\ 0 & 1 & 0 \\ -\sin(\beta(t)) & 0 & \cos(\beta(t)) \end{bmatrix} \quad (2.3)$$

$$r_I^{lu}(t) = \mathbf{R}_{lb}^{lu}(t)r_I^{lb}(t) \quad (2.4)$$

c) Inertial Measurement Unit (IMU) body frame (b):

- The axes of this reference frame is aligned along the axes of the accelerometers and gyroscopes of the IMU.
- Eq. (2.5) defines the coordinates of point I relative to the IMU coordinate system.

- The lever arm \mathbf{r}_{lu}^b , and boresight matrix \mathbf{R}_{lu}^b , are the spatial and rotational offsets between the laser unit coordinate system and IMU body frame, respectively. These terms are time independent because the Laser unit and IMU are rigidly fixed relative to one another (negligible aircraft flexure is assumed).

$$\mathbf{r}_I^b(t) = \mathbf{r}_{lu}^b + \mathbf{R}_{lu}^b \mathbf{R}_{lb}^{lu}(t) \mathbf{r}_I^{lb}(t) \quad (2.5)$$

d) Mapping reference frame (\mathbf{m}):

- This reference frame is the datum for the reconstructed point cloud and it is defined by the GNSS reference frame or a user specified reference frame.
- The position $\mathbf{r}_b^m(\mathbf{t})$, and the orientation $\mathbf{R}_b^m(\mathbf{t})$, of the IMU body frame relative to the mapping reference frame are derived through a post-processing GNSS/INS integration step.
- Eq. (2.6) defines the coordinates of point \mathbf{I} relative to the mapping reference frame.
- $\mathbf{r}_b^m(\mathbf{t})$ and $\mathbf{R}_b^m(\mathbf{t})$ are time dependent because the platform is in motion.

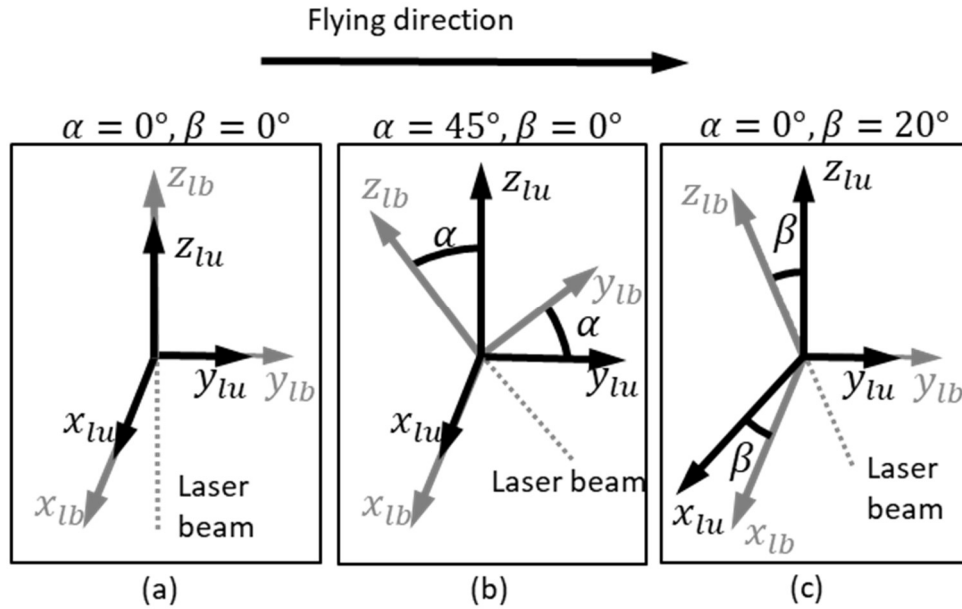


Figure 2.2: The Laser beam (*lb*) Coordinate System with Respect to the Laser unit (*lu*) Coordinate System at Various α and β Scan Angles

$$r_i^m(t) = r_b^m(t) + R_b^m(t)r_{lu}^b + R_b^m(t)R_{lu}^b R_{lb}^{lu}(t)r_i^{lb}(t) \quad (2.6)$$

Note that this LiDAR point-positioning equation does not have redundancy in deriving the ground coordinates. It is a summation of system parameters and direct measurements of the LiDAR system (Habib et al., 2009b). This characteristic plays a major role in the evaluation of the positional quality of LiDAR point clouds, which is discussed in the next section.

2.1 Quality Assurance (QA) and Quality Control (QC) of LiDAR Mapping

LiDAR mapping requires specific procedures to maintain quality throughout all preparation and collection steps. Before collection, there are typical QA procedures to complete in order to ensure that the point cloud is derived in such a way that optimizes quality. Likewise, QC measures that quantitatively evaluate the resulting point cloud after collection are also of utmost importance to verify the data quality and are usually defined beforehand. QA measures include the LiDAR scanner settings, planning collection routes,

a rigorous derivation of the system parameters via calibration, and a stability analysis of the calibration parameters (Habib et al., 2010a). The LiDAR scanner settings to be decided on include the scan angle, the scan rate, the laser beam divergence angles, and the laser pulse repetition rate. To specify collection routes, the flying height and lateral distance between flights should be planned. All of these QA procedures affect the presence or absence of occlusions, the inter-point spacing of the point cloud, and the positional accuracy. The QC is done after data collection by the end user. QC procedures include establishing measures that effectively verify the point cloud completeness and correctness. They include quantitative evaluation of the relative and absolute accuracy of the coordinates (Habib et al., 2010c), of the inter-point spacing (Lari and Habib, 2012), and also of the higher-level LiDAR data processing such as segmentation and classification (Lari and Habib, 2014; Habib and Lin, 2016).

These QA and QC procedures require attention to detail and knowledge of how each one affects the point cloud derivation process; there are also inherent and traditional obstacles in LiDAR QA and QC that require attention. The rigorous calibration of LiDAR systems remains to be a challenge for several reasons that are mostly related to the fact that the footprint of LiDAR is non-selective (Alharthy et al., 2004). Meaning, we are not guaranteed that the LiDAR footprint will fall on the center of a control target. Instead of directly using the coordinates of an observed control target, like in photogrammetry, highly reflective geometric shaped targets (e.g. spherical or square) can be placed over control points and the geometric center can be determined from the LiDAR point cloud (assuming the scanner settings are set such that there is an adequate amount of points on the geometric target) (Glennie, 2007). Moreover, the non-selective nature of LiDAR makes tie-point generation difficult because tie points cannot simply be selected from overlapping strips. Because the utilization of control and the tie-point generation are not straightforward for LiDAR data, the LiDAR calibration process requires more steps than photogrammetric calibration in order to generate and compare conjugate features in overlapping LiDAR surfaces (Kersting, 2011; Habib et al., 2008).

The QC procedures are also affected by the non-selective nature of LiDAR. For example, the process of evaluating inter-point spacing throughout the entire point cloud is difficult because it is always irregular (Habib and Lin, 2016). It is also important to note that evaluating inter-point spacing directly verifies some of the QA procedures. Evaluating positional accuracy is another QC procedure that is also greatly affected by the fact that the point-positioning equation is not based on redundant measurements, another consequence of the non-selective nature of LiDAR (Habib et al., 2009a; Habib et al., 2010a). Therefore, the traditional positional accuracy measures, i.e. variance-covariance matrices and a-posteriori variance factors, cannot be derived. QC can be divided into two categories, Internal Quality Control (IQC) and External Quality Control (EQC). EQC is an absolute measure that entails checkpoint analysis using control information. EQC is not only expensive but it does not provide the horizontal verification unless special targets are used (such as highly reflective geometric shaped targets previously mentioned) (Csanyi and Toth, 2007; Wotruba et al., 2005). IQC is a relative measure between overlapping strips, and actually every IQC can be employed as an EQC procedure by comparing point clouds with control surfaces instead of comparing point clouds with each other (Habib et al., 2010a). Strip adjustment is an IQC procedure that not only assesses the quality of overlapping strips, but it goes beyond all other QC procedures by also attempting to improve the alignment of overlapping strips by applying a rigid-body transformation (Habib et al., 2009a). Research has been done on different strip adjustment techniques that vary depending on the discrepancies detected, the matching procedure used, or the type of primitive used (points, lines, planes). Some developed strip adjustment procedures only detect vertical discrepancies (Crombaghs et al., 2000; Kager and Krauss, 2001). Since the biases have the greatest impact on the horizontal coordinates, this is not a complete strip adjustment solution. Others detect all discrepancies but have a simple transformation to model them (Maas, 2002; Filin and Vosselman, 2002). Since it is well known that the impacts of some biases are not linear, this is an approximate approach to strip adjustment. Because LiDAR points are irregular, some have alternatively used planes or lines as conjugate features instead of points (Hamza and Habib, 2013; Skaloud and Lichti, 2006; Kager, 2004; Pfeifer et al., 2005; Vosselman, 2002). However, these types of features only exist in urban areas (Bretar et al., 2004). In order not to be restricted to urban areas, some

use natural features that are locally approximated by planes (Filin and Vosselman, 2004). Primitives are the driving force for the success of any QA or QC procedure and they need to be carefully chosen. The decision on which primitive is appropriate for use when comparing overlapping LiDAR strips depends on how they can be automatically identified, how they can be represented, and how they can be robustly compared. A more in-depth discussion on primitives is provided in section 2.4.3.

These inherent obstacles and decisions within the QA and QC procedures occur due to the nature of LiDAR scanners, and a standardized approach for the community at large is yet to be adopted. Although both QA and QC are needed to ensure comprehensive quality of point clouds, the research objectives of this study focus on the QA procedures related to LiDAR system calibration and stability analysis.

2.2 LiDAR System Calibration and Stability Analysis Background

There are three different types of LiDAR system calibration methods which are implemented at different stages. The first is laboratory calibration, then platform calibration, and finally the in-situ calibration (Kersting et al., 2012).

- a) Laboratory calibration is done by the system manufacturer on all components within the system. This includes the range offset and mirror angle scale. If the manufacturer sells a LiDAR system (i.e. the scanning and ranging unit together with an integrated GNSS/INS), the lever arm and boresight are determined.
- b) Platform calibration is done by the data provider to determine the lever arm offset.
- c) In-situ calibration is done by data provider near the time of data collection. It is carried out to refine all parameters since the previous laboratory and platform calibrations might be unstable over time and possibly biased. For the in-situ calibration, the observed discrepancies between the LiDAR-derived and control surfaces are used to refine the mounting parameters and biases in the system measurements (mirror angles and ranges).

This work focuses on the in-situ calibration because current and past in-situ calibration approaches have many shortcomings. These shortcomings include empirical and/or non-transparent methodologies, lengthy and costly procedures, and usually a heavy reliance on control surfaces (Filin 2001). As mentioned before there are no commonly accepted LiDAR system calibration methodologies, each manufacturer provides their own calibration approach in their software, and the data providers might also have their own approach. Many times, the calibration approach significantly degrades the accuracy and when this is the case, it adversely affects any post-processing or conclusions drawn from the data. These shortcomings are often due to the fact that these are data-driven approaches which fit strips together without constraining the point cloud reconstruction to the physics of the sensor model. The integrity and usability of data can be greatly increased by the use of a standardized calibration that corrects the systematic errors with a system-driven approach which preserves the link to the sensor model.

A data-driven calibration process only uses the point cloud data, as opposed to the system-driven approaches which use system measurements and system parameters. The data-driven processes are developed because users do not always have access to raw measurements, due to manufacturer restrictions. When raw measurements are discussed here, it is referencing any of the measurements involved in the reconstruction of a LiDAR point at a certain time. These raw measurements include the position and orientation of the IMU body frame, and the scan angle and range. These data-driven approaches have major drawbacks because there is no reliance on the physical sensor model (i.e. the LiDAR point-positioning equation). Instead, they arbitrarily fit data strips together through a transformation model that may not scale appropriately to the entire data set. The link to the sensor model is very important and should always be present in a formal LiDAR system calibration. Establishing a link to the point-positioning equation using only the point cloud data was successfully accomplished in Habib et al., 2009 and Habib et al., 2010a, with the development of the *Simplified (S)* calibration. This approach was accomplished through a mathematical analysis of the LiDAR point-positioning equation that indirectly relates it to the detected discrepancies, and it will be derived in full below because it is one of the calibration approaches used as a comparison in the experimental results. This development

of the \mathcal{S} calibration established the first system-driven calibration to only use the point cloud. The \mathcal{S} calibration is separated into two distinct steps, the first is a registration algorithm that determines the discrepancies between overlapping strips and the second is a linear Least Squares estimation of the system parameters. The new calibration approach derived in this research is a data-driven calibration like the \mathcal{S} , but it is a 1-step approach where the matching and system parameter estimations are iteratively optimized together.

When raw measurements are available, then the mathematical relationship of the point-positioning equation is directly incorporated, making it a *system-driven calibration*. Such calibration can be further classified as a *rigorous* calibration or *pseudo-rigorous* calibration, depending on whether the raw measurements are fully or partially available, respectively. There have been various types of system-driven calibration approaches developed that differ based on a need for control surfaces (as opposed to using overlapping strips), dependence on urban settings, manual operations, and/or preprocessing of data. If control surfaces are readily available and economical, approaches that constrain the LiDAR point to those control surfaces would be suitable (Filin 2001), but this is not always the case and calibration solutions that take this approach are not suitable for all users. The majority of calibration methodology development has been done on the premise of comparing overlapping strips (to avoid dependency on control surfaces) for both *rigorous* approaches (Kersting, 2011; Kersting et al., 2012; Skaloud and Lichti, 2006; Friess, 2006) and *pseudo-rigorous* approaches (Habib et al., 2010b; Bang, 2010; Kersting 2012; Burman, 2000; Toth, 2002; Morin, 2002). The approaches that rely on the presence of planar features are restricted to urban areas where there are several slopes and aspects of planes available. In addition to that restriction, they also either have a dependence on manual selection (Skaloud and Lichti, 2006), or there is a preprocessing step that the point clouds go through for plane segmentation (Friess, 2006). As mentioned before, preserving the native link to the system's point-positioning equation is of utmost importance. But, that link is often sacrificed due to the irregularity of LiDAR data. One of the existing calibration approaches preserves the link to the sensor model (and does so within an architecture that is able to handle the irregularity of LiDAR points), but it approximates the ground truth by averaging the coordinates of tie points in overlapping strips (Morin, 2002). This is not an assumption

that should be applied generally to all overlapping flight strip comparisons, due to the nature of some biases when the system is flown in different directions. Lastly, some of the existing approaches have chosen to only focus on the angular biases found in the boresight rotation matrix that defines the orientation of the laser unit with respect to the IMU body frame. These are important developments because these biases tend to have the largest impact on the resulting point cloud, but it is not a complete solution to the other biases that might be present in the LiDAR system. The *Quasi-Rigorous (QR)* calibration approach proposed by Bang (2010) and Habib et al. (2010b), and the *rigorous* calibration approach proposed by Kersting (2011) and Kersting et al. (2012), use point primitives to preserve the link to the sensor model. They have an automated procedure that accounts for the irregularity of LiDAR point clouds, they rely on overlapping strips instead of expensive control surfaces, and they determine both linear and angular mounting parameters and internal characteristics. Since these calibration approaches are two of the three used as a comparison in the experiment results, they will be derived in the section below giving more insight into the conjugate feature matching procedure and the metrics and models employed. The Universal LiDAR Error Model (ULEM) developed by Rodarmel et al. (2015) is another approach that accomplishes system driven calibration. ULEM provides a comprehensive and efficient sensor modelling approach for error propagation and data adjustment (to include calibration), which specifically focuses on being accessible to the user community with standardized parameters, existing file formats, and efficient storage and calculations. The ULEM model is different from calibration specific models in that it is geared towards overall data adjustment (which includes determination of calibration parameters), and essentially parallels the photogrammetric approach to bundle adjustment. More specifically, ULEM provides the architecture to handle multi-ray points as well as simultaneous refinement of system calibration parameters and system measurements within the adjustment process. The ULEM allows for specification of values of not only the full adjustable parameter (system calibration and system measurement) error covariance matrix, but also parameters that model their temporal de-correlation.

Calibration is performed throughout the lifespan of a LiDAR system and one should also consider performing a stability analysis over time to quantify how the calibration

parameters change over time. Stability analysis is a timely subject because LiDAR systems are becoming more compact, economical, and readily available, and they are being used more often and for more types of engineering projects. Thus, this mapping tool is fading away from being a commodity. When a mapping tool that requires rigorous calibration is relied upon on such a regular basis, knowing the stability or reliability of that calibration also becomes more important. To the best of the author's knowledge, procedures for stability analysis of LiDAR system calibration have never been discussed in literature. There is research on the stability of photogrammetric systems and the research done here will consider insights taken from those studies (Habib et al., 2005; Lichti et al., 2009; Habib et al., 2014).

2.3 Strategy of LiDAR System Calibration

The system parameters to be established through LiDAR system calibration should be decoupled and estimated simultaneously in a Least Squares Adjustment. In order for the simultaneous estimation to be effective and accurate, there are several choices to be made about the strategy of the calibration process. This includes deciding upon an optimal, and minimal data collection strategy that magnifies the visibility of biases. Another prominent choice is the type of primitives to use when comparing overlapping strips and control information, whether they are the data points, or higher-level features within the point cloud (i.e. linear or planar features). The primitive choice conclusively influences the model to be chosen because the model should be able to incorporate the chosen features. The reasoning for certain architectural choices, in regard to the collection configuration, primitives, and the calibration mathematical model, will be outlined in the following sections after the theoretical basis of LiDAR calibration is discussed.

2.3.1 Theoretical Basis of LiDAR Calibration

The purpose of system calibration is to effectively reconstruct a point cloud as close as possible to the actual surface that was scanned. As noted before, the mathematical reconstruction of a point cloud is a function of measurements and system parameters. The calibration process provides the values of the system parameters by eliminating biases, and

the process of eliminating biases aids in reconstructing the point cloud as close as possible to the true representation. There are two different sets of system parameters to be estimated within the system calibration. The first set of parameters are referred to as the *mounting parameters*. The mounting parameters describe the spatial and rotational relationship between the IMU body frame and the laser unit coordinate system, and they are referred to as the lever arm (\mathbf{r}_{lu}^b) and boresight (\mathbf{R}_{lu}^b) components, respectively. The other set of parameters are within the laser unit. The calibration of these parameters is referred to as a *sensor calibration* and the parameters are referred to as *internal characteristics*. They include the range offset ($\Delta\rho$) and the scan angle scale factors ($\mathbf{S}_\alpha, \mathbf{S}_\beta$). In addition to the scale factor characteristic, the scan angles of a laser unit do contain biases that one might consider to model as an internal characteristic, but they are directly correlated with the boresight angles and cannot be uncorrelated no matter what the flight configuration. Because of this correlation, the scan angle biases cannot be simultaneously estimated with the boresight angles. The more significant scan angle error is the scale factors ($\mathbf{S}_\alpha, \mathbf{S}_\beta$) (Morin, 2002; Csanyi, 2008). The range offset error is a factor of several sources and has been determined to be a constant bias in the research of Filin (2001); Csanyi (2008); and Skaloud and Litchi (2006).

The notation of the two sets of parameters is listed here:

a) Mounting Parameters:

- Lever arm (\mathbf{r}_{lu}^b) components: $(\Delta X, \Delta Y, \Delta Z)^T$
- Boresight (\mathbf{R}_{lu}^b) components: $(\Delta\omega, \Delta\varphi, \Delta\kappa)^T$

b) Internal Characteristics:

- Range (ρ) offset: $\Delta\rho$
- Scale factors of the scan angles (α, β): $\mathbf{S}_\alpha, \mathbf{S}_\beta$

First, the system parameters outlined above are determined either from a laboratory or manufacturer calibration, or an initial estimate. Then, through an in-situ LiDAR system calibration, those values are refined in order to determine their true values. The calibration uses the initial values then strategically determines their refined value by comparing

overlapping strips and control information. The comparison process is carried out by detecting and minimizing discrepancies that inhibit the compatibility. This comparison is depicted in Figure 2.3. In order to have a reliable calibration that uses minimal, or no, control, the discrepancy minimization should be done using corresponding features within the point clouds. In order to do so successfully, the following tasks from Habib et al. (2017) should be completed; a) Determine which, if any, parameters would not produce a discrepancy, and then determine the minimal control necessary to estimate such a parameter (covered in section 2.3.2). b) Maximize the visibility of discrepancies between overlapping point clouds with a strategic data collection (covered in section 2.3.2). c) Identify which primitive would be appropriate for comparing LiDAR point clouds and account for the irregularity of LiDAR data (covered in section 2.3.3). d) Establish an automated strategy to match these primitives. Then, incorporate these matches and the sensor model into a procedure which evaluates system parameters (covered in section 2.4.3). e) Develop procedures which can handle the absence of system measurements (covered in section 2.4.2).

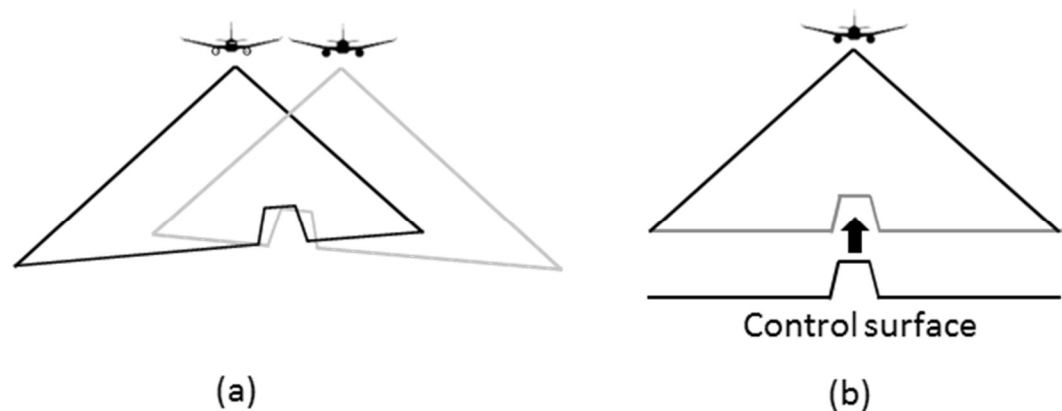


Figure 2.3: LiDAR System Calibration Strategy to Minimize Discrepancies between Overlapping Point Clouds (a) and Control Surfaces (b) (adapted from Bang, 2010)

2.3.2 LiDAR Data Collection Strategy

In order to reduce the control requirement and rely on features within the point cloud, the optimal data collection is the one that maximizes the impact of the systematic errors. This ensures that discrepancies between conjugate features are detected. First, the point-positioning equation will be inspected to make assumptions that are associated with the nature of airborne LiDAR collection and a general use case involving a linear scanner flying in a straight line. Then, the impact that the mounting parameter and internal characteristic biases have on the reconstructed point cloud will be determined. Some of the terms (e.g. $\mathbf{R}_b^m(\mathbf{t})$) of the equation are different for *forward* and *backward* flights, and they are denoted by a subscript of \mathbf{f} and \mathbf{b} , respectively (not to be confused with the b that is used to denote the IMU body frame). Moreover, some equations have multiple signs on each term, which indicates that the equation is representative of both *forward* and *backward* flights. The top sign represents the *forward* flight, and the bottom sign represents the *backward* flight.

The list of assumptions below essentially simplifies the point-positioning equation (2.7) into a different version where we can easily depict and discuss the impact that biases have on a reconstructed point cloud.

$$r_I^m(t) = r_b^m(t) + R_b^m(t)r_{lu}^b + R_b^m(t)R_{lu}^b R_{lb}^{lu}(t)r_I^{lb}(t) \quad (2.7)$$

1. The IMU body frame is aligned with its \mathbf{x}_b , \mathbf{y}_b , and \mathbf{z}_b axes pointing in starboard, flight, and up directions, respectively.
2. The airborne platform is flying with a constant heading along the South-to-North (denoted as *forward*) and North-to-South (denoted as *backward*) directions. Therefore, the $\mathbf{R}_b^m(\mathbf{t})$ rotation matrices for these flight lines are defined as per eq. (2.8) and eq.(2.9), respectively.

$$R_b^m(t)\{forward\} = \begin{bmatrix} 1 & 0 & 0 \\ 0 & 1 & 0 \\ 0 & 0 & 1 \end{bmatrix} \quad (2.8)$$

$$R_b^m(t)\{backward\} = \begin{bmatrix} -1 & 0 & 0 \\ 0 & -1 & 0 \\ 0 & 0 & 1 \end{bmatrix} \quad (2.9)$$

3. The IMU body frame and the laser unit coordinate system are almost parallel to each other with small boresight angles ($\Delta\omega, \Delta\varphi, \Delta\kappa$) describing their rotational relationship. Thus, the R_{lu}^b rotation matrix can be represented by eq. (2.10).

$$R_{lu}^b \approx \begin{bmatrix} 1 & -\Delta\kappa & \Delta\varphi \\ \Delta\kappa & 1 & -\Delta\omega \\ -\Delta\varphi & \Delta\omega & 1 \end{bmatrix} \quad (2.10)$$

4. The IMU body frame and the laser unit coordinate system are relatively close to each other. Therefore, the lever arm can be represented by the incremental vector in eq. (2.11).

$$r_{lu}^b = \begin{bmatrix} \Delta x \\ \Delta y \\ \Delta z \end{bmatrix} \quad (2.11)$$

5. We are dealing with a linear vertical scanner that maps a relatively flat terrain (with respect to the flying height) across the flight direction. Therefore, there is only one scan angle β and its corresponding scan angle scale factor is denoted as S . The coordinates of a given point I relative to the laser unit coordinate system, $r_I^{lu}(t)$, would be represented by eq. (2.12), where $\mathbf{x}(t)$ and \mathbf{z} are the x -laser unit coordinate and the z -laser unit coordinate of the LiDAR point with respect to the laser unit frame, respectively (as seen in Figure 2.4). The z -laser unit coordinate is considered constant due to the assumption that we are dealing with a relatively flat terrain.

These two coordinates are dependent on the mirror angle measurement β , range measurement ρ , and the internal characteristics $\Delta\rho$ and S , as seen in eq. (2.13) and eq. (2.14).

$$r_I^{lu}(t) = \begin{bmatrix} x(t) \\ 0 \\ z \end{bmatrix} \quad (2.12)$$

$$x(t) = -(\rho(t) + \Delta\rho) \sin(S\beta(t)) \quad (2.13)$$

$$z = -(\rho(t) + \Delta\rho) \cos(S\beta(t)) \quad (2.14)$$

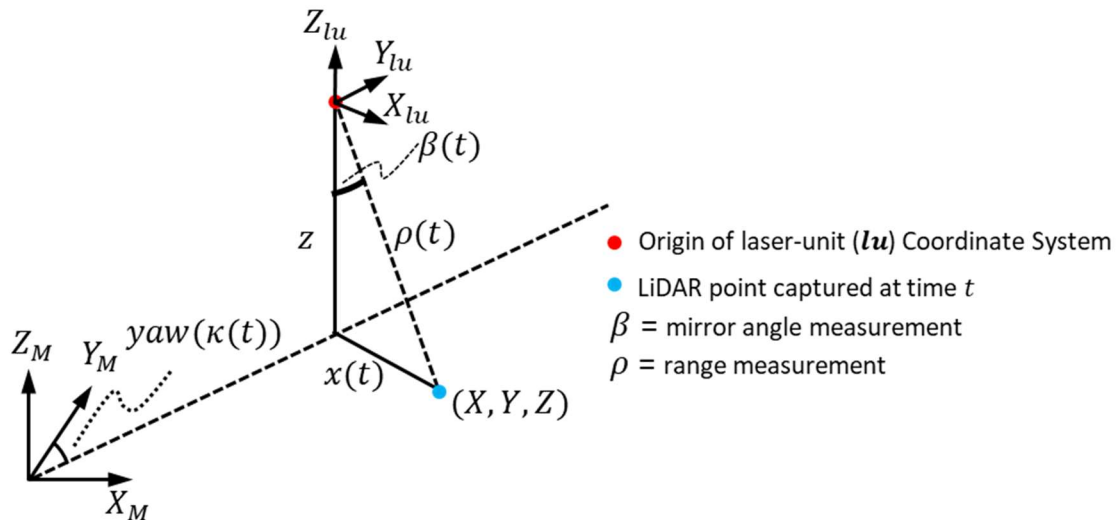


Figure 2.4: Laser unit Coordinates and their Relation to the Range and Mirror Angle Measurements

These assumptions result in the new form of the point-positioning equation seen in eq. (2.15).

$$r_I^m(t) = r_b^m(t) + \begin{bmatrix} \pm\Delta x \\ \pm\Delta y \\ \Delta z \end{bmatrix} + \begin{bmatrix} \pm 1 & \mp\Delta\kappa & \pm\Delta\varphi \\ \pm\Delta\kappa & \pm 1 & \mp\Delta\omega \\ -\Delta\varphi & \Delta\omega & 1 \end{bmatrix} \begin{bmatrix} x(t) \\ 0 \\ z \end{bmatrix} \quad (2.15)$$

Now the second step in the development of the acquisition scenario, defining the impact of the biases, can be completed. By investigating when and where the system parameter biases impact the reconstructed point cloud, we can determine what types of flights are needed to maximize the visibility of discrepancies between overlapping strips. More specifically, this will determine which system parameter biases are dependent on flying direction, flying height, and/or the scan angle. The impact is represented as δr_I^m , and is accomplished via taking the derivative of eq. (2.15) with respect to each bias, and then multiplying each resulting derivative by its respective bias. The results are shown in Table 2-1. In this table, a bias is represented by the symbol δ , which precedes the system parameter it is referring to, and the impact it has on the X_m , Y_m , or Z_m coordinate is separated into the columns of δX_m , δY_m , and δZ_m , respectively. Eq.(2.16) is the result of summing the columns of Table 2-1 to form the vector representation of the impact that the biases have on the coordinates. Eq.(2.17) is essentially the same as eq. (2.16) but it is reorganized by the different types of system parameters (the first term pertains to the lever arm, the second term pertains to the boresight angles, and the third and fourth terms pertain to the range offset and the scan angle scale factor, respectively).

Table 2-1: Impact of System Parameter Biases on Each Component of the Reconstructed Coordinate (Habib et al., 2009a)

	Impact		
	δX_m	δY_m	δZ_m
$\delta\Delta x$	$\pm\delta\Delta x$	0	0
$\delta\Delta y$	0	$\pm\delta\Delta y$	0
$\delta\Delta z$	0	0	$\delta\Delta z$
$\delta\Delta\omega$	0	$\mp z \delta\Delta\omega$	0
$\delta\Delta\varphi$	$\pm z \delta\Delta\varphi$	0	$-x(t)\delta\Delta\varphi$
$\delta\Delta\kappa$	0	$\pm x(t) \delta\Delta\kappa$	0
$\delta\Delta\rho$	$\mp \sin(S\beta(t)) \delta\Delta\rho$	0	$-\cos(S\beta(t)) \delta\Delta\rho$
δS	$\pm z\beta(t)\delta S$	0	$-x(t)\beta(t)\delta S$

$$\delta r_I^m = \begin{bmatrix} \pm\delta\Delta x \pm z\delta\Delta\varphi \mp \sin(S\beta(t)) \delta\Delta\rho \pm z\beta(t)\delta S \\ \pm\delta\Delta y \pm x(t)\delta\Delta\kappa \mp z\delta\Delta\omega \\ \delta\Delta z - x(t)\delta\Delta\varphi - \cos(S\beta(t)) \delta\Delta\rho - x(t)\beta(t)\delta S \end{bmatrix} \quad (2.16)$$

$$\delta r_I^m = \begin{bmatrix} \pm\delta\Delta x \\ \pm\delta\Delta y \\ \delta\Delta z \end{bmatrix} + \begin{bmatrix} 0 & \mp\delta\Delta\kappa & \pm\delta\Delta\varphi \\ \pm\delta\Delta\kappa & 0 & \mp\delta\Delta\omega \\ -\delta\Delta\varphi & \delta\Delta\omega & 0 \end{bmatrix} \begin{bmatrix} x(t) \\ 0 \\ z \end{bmatrix} + \begin{bmatrix} \mp \sin(S\beta(t)) \delta\Delta\rho \\ 0 \\ -\cos(S\beta(t)) \delta\Delta\rho \end{bmatrix} + \begin{bmatrix} \pm z\beta(t)\delta S \\ 0 \\ -x(t)\beta(t)\delta S \end{bmatrix} \quad (2.17)$$

After deriving the impact of each bias for both the *forward* and *backward* flights in Table 2-1, we can see many patterns and affects that are useful for developing the optimal and minimal configuration. One can understand which biases impact each coordinate, and then even more importantly whether or not a bias impact is dependent on flying direction, flying height, and/or scan angle. Understanding these relationships will guide the process of developing the optimal and minimal configuration because it will reveal which biases will be visible when comparing overlapping point clouds and control information. Table 2-2,

Table 2-3, and Table 2-4 depict which biases impact the X , Y , and Z coordinates, respectively. As depicted in Figure 2.5, if an expression in the bias impact columns of these tables includes $x(t)$, $\beta(t)$, or $\sin(\beta(t))$, then it is scan angle dependent, and if an expression includes $z(t)$, then it is flying height dependent. If an expression contains the double signage \pm or \mp , then it is flying direction dependent. The only time such observation is not true is when an expression includes \pm or \mp in addition to the x-laser unit coordinate $x(t)$, the scan angle $\beta(t)$, or the sine of the scan angle $\sin(\beta(t))$. This is because the sign of $x(t)$, $\beta(t)$, and $\sin(\beta(t))$ also changes depending on the flight direction, as seen in Figure 2.5. As an example, the term $\pm x(t)$ is not flying direction dependent because the sign of $x(t)$ also changes for *forward* and *backward* flights, thus negating the flying direction dependence from the double signage. In a similar manner, if an expression has only $x(t)$, $\beta(t)$, or $\sin(\beta(t))$, then it is flying direction dependent. Finally, when an expression has two of the three flying direction dependent terms ($x(t)$, $\beta(t)$, and $\sin(\beta(t))$), and no double signage, there will be no dependence on flying direction.

Table 2-2: Biases that Impact the X Coordinate and their Dependencies

Bias	Bias Impact	Dependencies		
		Flying Direction Dependent	Flying Height Dependent	Scan Angle Dependent
$\delta\Delta x$	$\pm\delta\Delta x$	Yes	No	No
$\delta\Delta\varphi$	$\pm z \delta\Delta\varphi$	Yes	Yes	No
$\delta\Delta\rho$	$\mp \sin(S\beta(t)) \delta\Delta\rho$	No	No	Yes
δS	$\pm z\beta(t)\delta S$	No	Yes	Yes

Table 2-3: Biases that Impact the Y Coordinate and their Dependencies

Bias	Bias Impact	Dependencies		
		Flying Direction Dependent	Flying Height Dependent	Scan Angle Dependent
$\delta\Delta y$	$\pm\delta\Delta y$	Yes	No	No
$\delta\Delta\kappa$	$\pm x(t) \delta\Delta\kappa$	No	No	Yes

Table 2-4: Biases that Impact the Z Coordinate and their Dependencies

Bias	Bias Impact	Dependencies		
		Flying Direction Dependent	Flying Height Dependent	Scan Angle Dependent
$\delta\Delta z$	$\delta\Delta z$	No	No	No
$\delta\Delta\varphi$	$-x(t) \delta\Delta\varphi$	Yes	No	Yes
$\delta\Delta\rho$	$-\cos(S\beta(t)) \delta\Delta\rho$	No	No	Yes
δS	$-x\beta(t)\delta S$	No	No	Yes

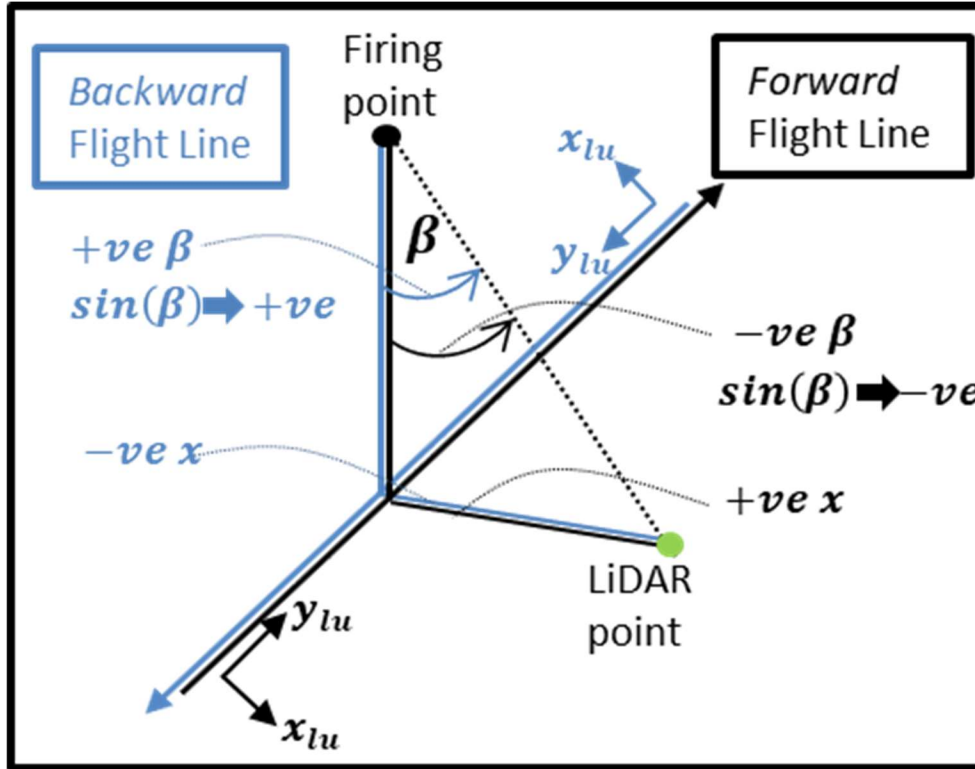


Figure 2.5: Illustration of the Flying Direction Dependent Terms, $(\beta(t), \sin(\beta(t)),$ and $x(t))$, other than the Double Signage Term

The term strip-pair, is used to denote two overlapping flight strips that we have chosen to compare. As seen in Table 2-2, Table 2-3, and Table 2-4, the four *mounting parameter* biases $\delta\Delta X$, $\delta\Delta Y$, $\delta\Delta\omega$, and $\delta\Delta\phi$, are dependent on the flying direction; therefore, a strip-pair with opposite flying directions can be used to estimate them. The biases $\delta\Delta X$ and $\delta\Delta\phi$ both impact the X coordinate, but they can be decoupled using opposite flying directions since $\delta\Delta\phi$ also impacts the Z coordinate. The biases $\delta\Delta Y$ and $\delta\Delta\omega$ both only impact the Y coordinate and they cannot be decoupled with just opposite flying directions. Therefore, we use an additional strip pair with different flying directions at a different flying height from the first one since $\delta\Delta\omega$ is flying height dependent (Table 2-3). The scan angle dependent biases seen in Table 2-2, Table 2-3, and Table 2-4 are the *mounting parameter* bias $\delta\Delta\kappa$ and the *internal characteristic* biases $\delta\Delta\rho$ and δS . To detect these biases, a strip pair with less than 100 percent overlap should be used so that when compared, the discrepancy is visible since the overlapping points have differing scan angles. Furthermore,

that overlap should be minimized to maximize the difference in scan angle (which maximizes the observed discrepancy). As seen in Table 2-4 the impact of $\delta\Delta Z$ will not be seen no matter what the flight configuration is, and therefore control information in the Z direction is necessary to estimate this bias (Habib et al., 2009b). The resulting optimal configuration can be seen in Figure 2.6 and it is composed of five flight lines as well as vertical control. The first two strip-pairs are comprised of *forward* and *backward* flights with almost 100% overlap, and the two strip-pairs are at different flying heights. The third strip-pair is two parallel flight lines with a large lateral distance between them (about 50% overlap). Furthermore, the terrain between the overlap case with a large lateral distance should have adequate elevation variation, since planimetric discrepancies across the flight direction are needed for the $\delta\Delta\rho$ estimation. This is because the impact is relatively small and can therefore be insignificant compared to the noise level of the data (making it undetectable) if the elevation variation is low. If this area does not exhibit enough elevation variation, then $\delta\Delta\rho$ also needs vertical control in order to be estimated. When this is the case, the $\delta\Delta z$ and $\delta\Delta\rho$ biases cannot be simultaneously estimated because their impact on the Z_I^m coordinate is highly correlated when the scan angle is relatively small. With the established optimal and minimal configuration, the calibration process can be carried out by detecting discrepancies between overlapping strips and then minimizing such discrepancies by estimating the system parameters using the point-positioning equation.

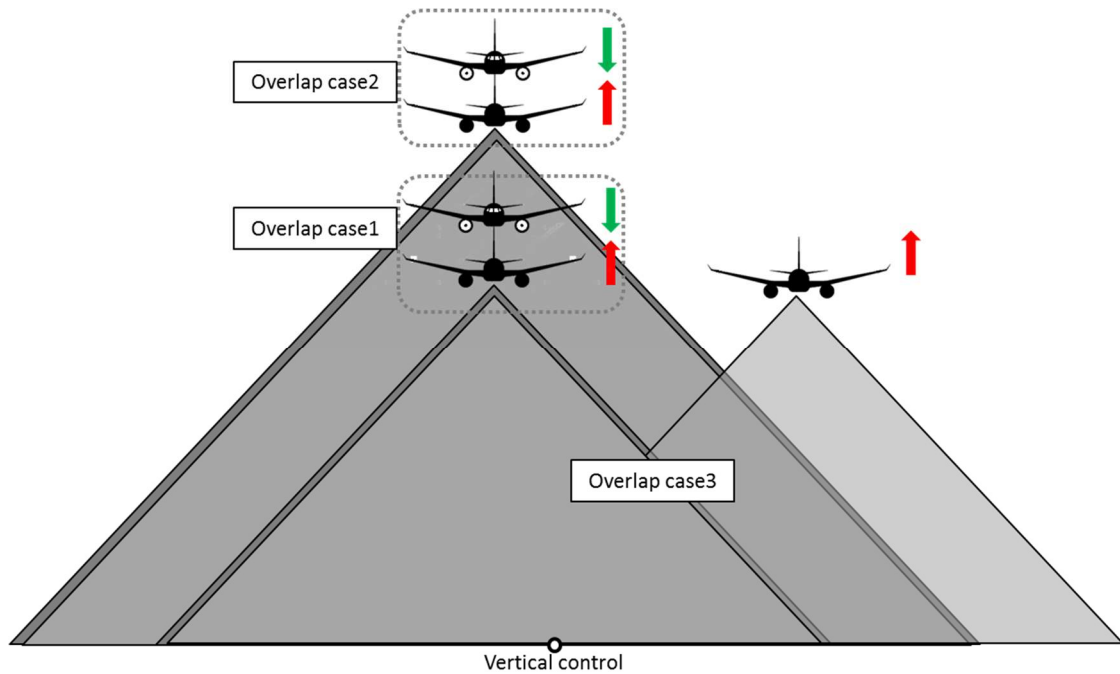


Figure 2.6: Optimal/Minimal Flight Configuration for Airborne LiDAR System Calibration (adapted from Bang, 2010)

2.3.3 Calibration Primitives

Employing point based matches for the calibration strategy ensures the mathematical relationship between the point cloud and the sensor model (sensor model contains the system parameters to be estimated) is preserved, but these matches do not actually exist because LiDAR data is irregular. With irregular data, conjugate points in overlapping data are not as straightforward as they are with other geospatial data (such as photogrammetry), where distinct control and tie points can be identified. Higher level features, such as lines and planes, can be reliably derived and used as conjugate features (Hamza and Habib, 2013; Vosselman, 2002; Pfeifer et al., 2005), but we are not always guaranteed to have these features available in the covered areas. In addition to the problem of the availability of higher level features, using them as conjugate features requires preprocessing of the data in order to extract them. The most prominent drawback of using higher level features is that the link between the features and the sensor model is lost unless the parameters are extended to include the parameters of that feature. Since using points as conjugate features

is the only way to preserve this crucial relationship to the sensor model, an approach that properly accounts for the irregularity of LiDAR points needs to be used. Bretan (2004) uses interpolated regions to bypass the issue of distinct points but does not have an optimal matching procedure. Throughout the many tests on primitives and conjugate features, the most recommended correspondence for LiDAR point cloud analysis is between discrete points in one scan, and a triangulated irregular networks (TIN) of the other scan (Habib et al., 2010d; Maas, 2002). The concept of point-patch pairs is illustrated in Figure 2.7. The point and the patch are considered to be pseudo-conjugate points, they are not distinct conjugates, but they belong to conjugate features.

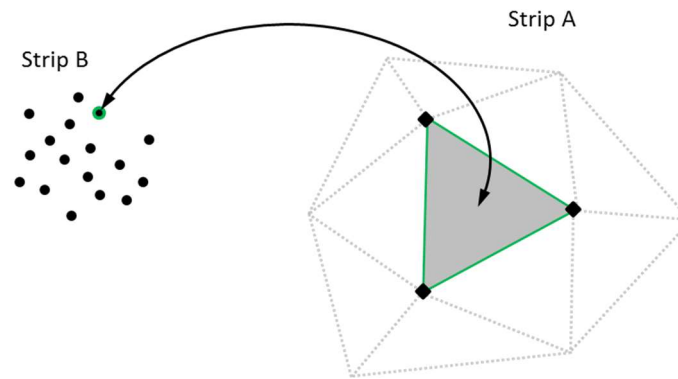


Figure 2.7: Point-patch Pair

The matching approach used in these calibration methods is the *Iterative Closest Patch* (ICPatch) (Habib et al., 2009b; Bang, 2010), and it properly accounts for the irregularity of LiDAR data by using the point-to-patch matches in conjunction with a weight modification. The process of pairing points with their corresponding patches involves matching a point from strip **B** to the closest patch in strip **A**. In order to be confirmed as a point-patch pair, there are three criteria that need to be met (Habib et. al., 2010d).

1. Of all the patches, the patch is the closest to the projected point,
2. The normal distance observed between the point and that patch is less than the determined threshold (which is determined based on the point cloud noise level),
and

3. The projection of the point onto the patch falls inside the patch.

The result of ICPatch is a set of point-patch pairs, and when these matches are employed in the calibration, any vertex of the patch is used as the pseudo-conjugate to the point from **B**. During calibration, instead of minimizing the **XYZ** discrepancies, the normal distance between the point and the conjugate patch should be minimized through a weight modification process. The weight modification steps are defined here:

- a) Calculate the variance-covariance matrix using error propagation and the calibration math model, and then calculate its corresponding weight matrix \mathbf{P}_{XYZ} .
- b) Define a new \mathbf{uvw} coordinate system where \mathbf{w} coincides with the normal to the patch, and the $\mathbf{u-v}$ plane coincides with the patch as seen in Figure 2.8.
- c) Derive the rotation matrix from the **XYZ** mapping frame to the \mathbf{uvw} frame, \mathbf{R}_{XYZ}^{uvw} . Using error propagation, calculate the weight matrix corresponding to the \mathbf{uvw} system according to eq. (2.18).

$$P_{uvw} = \begin{bmatrix} p_{uu} & p_{uv} & p_{uw} \\ p_{vu} & p_{vv} & p_{vw} \\ p_{wu} & p_{wv} & p_{ww} \end{bmatrix} = R_{XYZ}^{uvw} P_{XYZ} R_{uvw}^{XYZ} \quad (2.18)$$

- d) Because we wish to only consider the weight along the patch normal direction, the weight matrix is modified to eq. (2.19).

$$P'_{uvw} = \begin{bmatrix} 0 & 0 & 0 \\ 0 & 0 & 0 \\ 0 & 0 & p_{ww} \end{bmatrix} \quad (2.19)$$

- e) Use error propagation again to define the new weight matrix with respect to the **XYZ** frame. This operation can be seen in eq. (2.20), which is the final weight matrix that will be used in the calibration.

$$P'_{XYZ} = R_{uvw}^{XYZ} P'_{uvw} R_{XYZ}^{uvw} \quad (2.20)$$

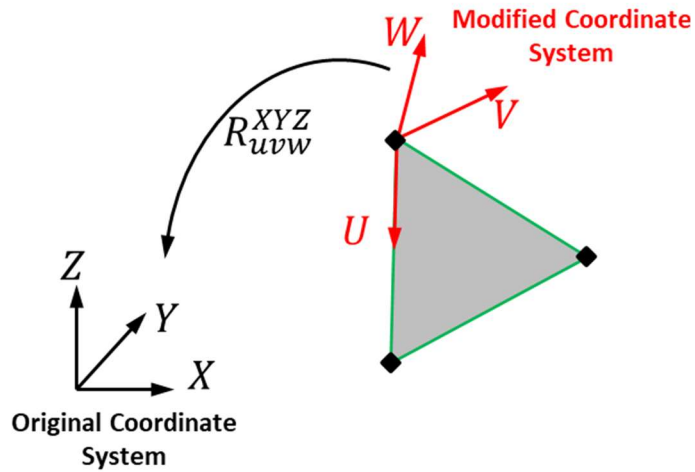


Figure 2.8: Formation of the uvw Modified Coordinate System for ICPatch Weight Modification (adapted from Bang, 2010)

The weight modification is necessary to account for the fact that a point based procedure is being used with pseudo-conjugate points. The initial discrepancy equation is formed with the point in strip A and a vertex of the matching patch from strip B , the weight modification allows the conjugate point in strip B to move around in the plane of the patch to ensure the minimization of the normal distance from the patch to the point (Habib et. al., 2010d).

When comparing control points with LiDAR points, the TIN is generated from the LiDAR point cloud, because control points are usually minimized for cost and therefore not dense enough to characterize the ground surface (if a control surface is provided as opposed to control points, then the TIN may also be generated from the control surface). Other research has used higher-level features, such as planes or lines, as conjugate primitives (Vosselman, 2002); but with such approaches the crucial link to the sensor model is lost (Habib et al., 2008; Skaloud and Lichti, 2006). ICPatch is preferred here because it is based on the original, irregular points as input, and the matching procedure accounts for the irregularity of LiDAR data. In addition to the generation of the point-patch pairs, ICPatch also estimates a rigid body transformation between strip A and strip B .

2.4 System Calibration Procedures

The following sections derive the calibration procedures for both *rigorous* and *pseudo-rigorous* approaches. From this point on, the *rigorous* approach proposed by Kersting (2011) is referred to as the *Rigorous (R)* approach, and the *S* (Bang, 2010) and *QR* (Bang, 2010) approaches are collectively referred to as the *Pseudo-rigorous* approaches (*Pseudo-rigorous* approaches will also entail the new *QRQS* approach once it has been developed in Chapter 3).

2.4.1 Rigorous (R) LiDAR System Calibration

The *R* calibration procedure is used when all raw measurements are available. The development of the calibration math model follows upon the previously established theoretical basis in 2.3.1 of comparing overlapping point clouds and control information through the use of the point-positioning equation (2.6). The symbolic form of eq. (2.6) is eq. (2.21). In eq. (2.21), the approximate values of the system parameters are represented as \mathbf{x}_o , the unknown corrections to the approximate values of the system parameters are represented as $\delta\mathbf{x}$, and the system measurements are represented as \mathbf{y} . The true system parameter values are represented as \mathbf{x} , and the expanded form of \mathbf{x} is shown in eq. (2.22). The expanded form of vector \mathbf{y} is shown in eq. (2.23). Also in eq. (2.21), the noise in the system measurements is \mathbf{e} , whereas Σ represents the variance-covariance matrix of that noise vector and is expanded in eq. (2.24).

$$r_I^m(t) = f(\mathbf{x}_o + \delta\mathbf{x}, \mathbf{y} - \mathbf{e}) \ \& \ \mathbf{e} \sim (0, \Sigma) \quad (2.21)$$

$$x = \begin{bmatrix} \Delta X \\ \Delta Y \\ \Delta Z \\ \Delta \omega \\ \Delta \varphi \\ \Delta \kappa \\ \Delta \rho \\ S_\alpha \\ S \end{bmatrix} \quad (2.22)$$

$$y = \begin{bmatrix} X \\ Y \\ Z \\ \omega \\ \varphi \\ \kappa \\ \rho \\ \alpha \\ \beta \end{bmatrix} \quad (2.23)$$

$$\Sigma = \begin{bmatrix} \sigma_X^2 & 0 & 0 & 0 & 0 & 0 & 0 & 0 & 0 \\ 0 & \sigma_Y^2 & 0 & 0 & 0 & 0 & 0 & 0 & 0 \\ 0 & 0 & \sigma_Z^2 & 0 & 0 & 0 & 0 & 0 & 0 \\ 0 & 0 & 0 & \sigma^2 & 0 & 0 & 0 & 0 & 0 \\ 0 & 0 & 0 & 0 & \sigma_\varphi^2 & 0 & 0 & 0 & 0 \\ 0 & 0 & 0 & 0 & 0 & \sigma_\kappa^2 & 0 & 0 & 0 \\ 0 & 0 & 0 & 0 & 0 & 0 & \sigma_\rho^2 & 0 & 0 \\ 0 & 0 & 0 & 0 & 0 & 0 & 0 & \sigma_\alpha^2 & 0 \\ 0 & 0 & 0 & 0 & 0 & 0 & 0 & 0 & \sigma^2 \end{bmatrix} \quad (2.24)$$

The two flight lines within a strip-pair are denoted by subscripts **A** and **B**, and their respective time stamps associated with a specific point of interest are denoted as \mathbf{t}_A and \mathbf{t}_B , respectively. Eq. (2.25) represents the mathematical relationship between pseudo-conjugate points, and it shows that when the true system parameter values \mathbf{x} ($\mathbf{x} = \mathbf{x}_o + \delta\mathbf{x}$) are used and the noise impact (\mathbf{e}_A and \mathbf{e}_B) removed, the conjugate points should have

identical coordinates. In order to be used in a Least Squares Adjustment, eq. (2.25) must be linearized, which is shown on the right side of eq. (2.26). In eq. (2.26), the terms \mathbf{f}_A and \mathbf{f}_B , are the predicted point cloud coordinates reconstructed using the approximate values for the system parameters \mathbf{x}_o , and the noise-contaminated measurements \mathbf{y}_A and \mathbf{y}_B , for flight lines \mathbf{A} and \mathbf{B} , respectively. The Jacobian matrices in eq. (2.26) J_{x_A} and J_{x_B} are relative to the system parameters, and the matrices J_{y_A} and J_{y_B} are relative to the system measurements. The Jacobian matrices are evaluated using the approximate system parameter values \mathbf{x}_o , and the measurements \mathbf{y} . Next, we rearrange eq. (2.26) so that the predicted coordinates \mathbf{f}_A and \mathbf{f}_B are on the left side leaving the system parameters to be estimated on the right side. This leads to the final representation of the \mathbf{R} calibration math model, eq. (2.27). It is stated in eq. (2.27) that the combined error term from this discrepancy equation is $(J_{y_A}e_A - J_{y_B}e_B)$, and it is distributed with a mean of zero and variance-covariance matrix of $(J_{y_A}\Sigma_A J_{y_A}^T + J_{y_B}\Sigma_B J_{y_B}^T)$. During implementation, the Σ matrix is filled using the reported hardware uncertainties and assumes no correlation between measurements acquired at different time stamps.

$$\begin{aligned} r_{I_A}^m(t_A) - r_{I_B}^m(t_B) &= f(x_o + \delta x, y_A - e_A) - f(x_o + \delta x, y_B - e_B) \\ &= 0 \end{aligned} \quad (2.25)$$

$$\begin{aligned} r_{I_A}^m(t_A) - r_{I_B}^m(t_B) &\approx (f_A + J_{x_A}\delta x - J_{y_A}e_A) - (f_B + J_{x_B}\delta x - \\ &J_{y_B}e_B) = 0, \text{ where } f_A = f(x_o, y_A), f_B = f(x_o, y_B) \end{aligned} \quad (2.26)$$

$$\begin{aligned} f_A(t_A) - f_B(t_B) &= -(J_{x_A}\delta x - J_{y_A}e_A) + (J_{x_B}\delta x - J_{y_B}e_B) \\ &\&(J_{y_A}e_A - J_{y_B}e_B) \sim (0, J_{y_A}\Sigma_A J_{y_A}^T + J_{y_B}\Sigma_B J_{y_B}^T) \end{aligned} \quad (2.27)$$

A discrepancy equation should also be developed for comparing flight strips with control. The development of this discrepancy equation is shown in eq. (2.28) through eq. (2.30), and it follows the same sequence of eq. (2.25) through eq. (2.27) (except the conjugate

point from flight line \mathbf{B} is now a control point). The noise-free control point is represented as \mathbf{r}_{IC}^m , and the noise-contaminated control point is represented as $\mathbf{r}_{IC_o}^m$. The noise contaminating the control point is represented as \mathbf{e}_C , and its variance-covariance matrix is represented as Σ_C . Eq. (2.30) shows that the uncertainty of the combined error term in the discrepancy equation is $(\mathbf{J}_{y_A}\mathbf{e}_A - \mathbf{e}_C)$, and it is distributed with a mean of zero and a variance-covariance matrix of $(\mathbf{J}_{y_A}\Sigma_A\mathbf{J}_{y_A}^T + \Sigma_C)$. To carry out the calibration, eq. (2.27) and eq. (2.30) are simultaneously used in a Least Squares Adjustment solving for the unknown system parameters (Mikhail and Ackerman, 1976). Upon estimation of the system parameters, the calibration is then completed by reconstructing the coordinates through the LiDAR point-positioning equation with the updated set of system parameters.

$$\begin{aligned} r_{I_A}^m(t_A) - r_{I_C}^m &= f(x_o + \delta x, y_A - e_A) - (r_{I_{C_o}}^m - e_C) \\ &= 0 \quad \& \quad e_A \sim (0, \Sigma_A), e_C \sim (0, \Sigma_C) \end{aligned} \quad (2.28)$$

$$r_{I_A}^m(t_A) - r_{I_C}^m \approx (f_A + J_{x_A}\delta x - J_{y_A}e_A) - (r_{I_{C_o}}^m - e_C) = 0 \quad (2.29)$$

$$\begin{aligned} f_A(t_A) - r_{I_{C_o}}^m &= -J_{x_A}\delta x + J_{y_A}e_A - e_C \quad \& \quad (J_{y_A}e_A - \\ &e_C) \sim (0, J_{y_A}\Sigma_A\mathbf{J}_{y_A}^T + \Sigma_C) \end{aligned} \quad (2.30)$$

2.4.2 Pseudo-rigorous LiDAR System Calibration

Since the manufacturer may not always provide the raw measurements, system-driven calibration approaches in the full or partial absence of raw measurements need to be developed and discussed. The raw measurements, being referred to here, consist of the position and orientation of the IMU body frame interpolated at the time of the individual laser pulses, $\mathbf{r}_b^m(\mathbf{t})$ and $\mathbf{R}_b^m(\mathbf{t})$, respectively, as well as the range and mirror angles needed to define $\mathbf{r}_I^{lu}(\mathbf{t})$. When these measurements are available, the \mathbf{R} calibration procedure is the most suitable. The two calibration approaches detailed below show how a calibration

can be approached in the absence of system raw measurements. Note that these calibration approaches are all restricted to linear scanners, but there is a possibility of expanding the theory in future research to incorporate elliptical scanners. The **QR** calibration is employed whenever the time-tagged point cloud and the time-tagged trajectory are available. The **S** calibration is the approach that can be employed when just the point cloud information is available.

2.4.2.1 Quasi-Rigorous (**QR**) Calibration Procedures

The **QR** calibration is developed assuming we have the time-tagged point cloud and time-tagged position information of the trajectory. The point cloud coordinates are derived using biased system parameters, denoted henceforth as biased point cloud coordinates. The **QR** calibration math model and procedure will be developed in a similar manner as the **R**, but instead of determining the system parameters, the system parameter biases are determined and the missing raw measurements are synthesized using the given data. The missing raw measurements are $\mathbf{R}_b^m(\mathbf{t})$ and $\mathbf{r}_I^{lu}(\mathbf{t})$, and to effectively synthesize the measurements, the data should follow a certain assumption that will allow the point-positioning equation to be simplified. The assumption is that we are dealing with a linear vertical scanner which maps the terrain across the flight direction. Therefore, there is only one scan angle $\beta(\mathbf{t})$, and the coordinates of a given point I relative to the laser unit coordinate system \mathbf{r}_I^{lu} , can be represented by the lateral and vertical distances between the flight trajectory and the point in question, respectively, as seen in eq. (2.31). Here, $\mathbf{z}(\mathbf{t})$ is a function of time because it is not assumed to be constant (as was the case in section 2.3.2). Also, the rotation matrix from the body frame to the mapping frame $\mathbf{R}_b^m(\mathbf{t})$, is now only a function of heading $\kappa(\mathbf{t})$, because the platform maintains a constant height with no roll and pitch. In addition to this assumption, the **QR** calibration also has expectations about the location and orientation of the IMU body frame and laser unit coordinate systems. It is important to note that these expectations can always be met by introducing virtual coordinate systems, and therefore they are not required in order to carry out the calibration. First, it is expected that the IMU body frame is aligned with its \mathbf{x}_b , \mathbf{y}_b , and \mathbf{z}_b axes pointing in the starboard, flight, and up directions, respectively. Also, the IMU body frame and the laser unit coordinate systems are expected to be almost parallel and close to each other with small boresight

angles $(\Delta\omega, \Delta\varphi, \Delta\kappa)$ and a small lever arm offset $(\Delta X, \Delta Y, \Delta Z)$ describing their rotational and translational relationship, respectively. The linear vertical scanner assumption and the expectations about the coordinate system configurations collectively simplify the LiDAR point-positioning equation into eq. (2.32) below.

$$r_i^{lu}(t) = \begin{bmatrix} x(t) \\ 0 \\ z(t) \end{bmatrix} \quad (2.31)$$

$$\begin{aligned} r_i^m(t) &= r_b^m(t) + \begin{bmatrix} \cos(\kappa(t)) & -\sin(\kappa(t)) & 0 \\ \sin(\kappa(t)) & \cos(\kappa(t)) & 0 \\ 0 & 0 & 1 \end{bmatrix} \begin{bmatrix} \Delta x \\ \Delta y \\ \Delta z \end{bmatrix} \\ &+ \begin{bmatrix} \cos(\kappa(t)) & -\sin(\kappa(t)) & 0 \\ \sin(\kappa(t)) & \cos(\kappa(t)) & 0 \\ 0 & 0 & 1 \end{bmatrix} \begin{bmatrix} 1 & -\Delta\kappa & \Delta\varphi \\ \Delta\kappa & 1 & -\Delta\omega \\ -\Delta\varphi & \Delta\omega & 1 \end{bmatrix} \begin{bmatrix} x(t) \\ 0 \\ z(t) \end{bmatrix} \end{aligned} \quad (2.32)$$

The symbolic representation of a biased coordinate is seen in eq. (2.33). The term $r_i^m(\mathbf{t}, \mathbf{biased})$, represents the biased point cloud coordinates derived using the inaccurate system parameters. In eq. (2.33), the true system parameters are represented as \mathbf{x} and the term $\delta\mathbf{x}_b$, represents the biases contaminating the system parameters (the subscript b distinguishes it from the term $\delta\mathbf{x}$ which was introduced in the \mathbf{R} procedure as the corrections to the approximate values of system parameters). The measurements are represented as \mathbf{y} , the noise free system measurements as \mathbf{y}_{nf} , the error associated with those measurements as \mathbf{e} , and the time tag of the point in question as \mathbf{t} . Using Taylor series expansion, eq. (2.33) could be expanded to the form in eq. (2.34). The term $\mathbf{f}(\mathbf{x}, \mathbf{y}_{nf}, \mathbf{t})$, represents the true coordinates of the point in question $r_i^m(\mathbf{t})$. Eq.(2.34) is reformulated into eq. (2.35) by writing the true coordinates in terms of the biased coordinates. Now the discrepancy equations can be formed under the presumption that true conjugate points should have identical coordinates. This relationship is seen in eq. (2.36), and it is then reformulated into eq. (2.37) so that the biased coordinates are on the left and the values to be estimated are on the right. When control is incorporated, the discrepancy equation to

use is eq. (2.38). Instead of comparing a biased point coordinate from A to a biased point coordinate from B , eq. (2.38) compares a biased point coordinate from A to the control point $r_{I_{C_0}}^m$.

$$r_I^m(t, \text{biased}) = f(x + \delta x_b, y_{nf} + e, t) \quad (2.33)$$

$$\begin{aligned} r_I^m(t, \text{biased}) &\approx f(x, y_{nf}, t) + J_x \delta x_b + J_y e \\ &\approx r_I^m(t) + J_x \delta x_b + J_y e \end{aligned} \quad (2.34)$$

$$r_I^m(t) = r_I^m(t)(\text{biased}) - J_x \delta x_b - J_y e \quad (2.35)$$

$$\begin{aligned} r_{I_A}^m(t_A) - r_{I_B}^m(t_B) &\approx (r_{I_A}^m(t_A, \text{biased}) - J_{x_A} \delta x_b - J_{y_A} e_A) - \\ &(r_{I_B}^m(t_B, \text{biased}) - J_{x_B} \delta x_b - J_{y_B} e_B) = 0 \end{aligned} \quad (2.36)$$

$$\begin{aligned} r_{I_A}^m(t_A, \text{biased}) - r_{I_B}^m(t_B, \text{biased}) \\ = (J_{x_A} \delta x_b + J_{y_A} e_A) - (J_{x_B} \delta x_b + J_{y_B} e_B) \end{aligned} \quad (2.37)$$

$$r_{I_A}^m(t_A, \text{biased}) - r_{I_{C_0}}^m = (J_{x_A} \delta x_b + J_{y_A} e_A) - e_C \quad (2.38)$$

The discrepancy equations can then be evaluated using the biased point cloud coordinates and the Jacobian matrices. The term $J_x \delta x_b$, is shown in eq. (2.39) and is evaluated using synthesized raw measurements from the time-tagged point clouds and system trajectory. Figure 2.9 depicts what spatial relationships are used to synthesize the raw measurements. Using this figure, the raw measurements can be synthesized according to the following steps:

- The trajectory heading can be estimated for a given LiDAR point captured at time t by analyzing the trajectory points within the time range $[t - \Delta t, t + \Delta t]$ and

fitting a line through these selected points. The trajectory heading is estimated from this orientation of this line that is approximating the local trajectory. The heading is then used to determine $\mathbf{R}_b^m(\mathbf{t})$.

- The firing point of the laser pulse can be determined by projecting the LiDAR point in question onto the trajectory.
- The firing point of the laser beam is used to evaluate $\mathbf{r}_l^{lu}(\mathbf{t}) = [\mathbf{x}(\mathbf{t}) \quad \mathbf{0} \quad \mathbf{z}(\mathbf{t})]^T$; where $\mathbf{x}(\mathbf{t})$ and $\mathbf{z}(\mathbf{t})$ are the x -laser unit coordinate and the z -laser unit coordinate of the LiDAR point with respect to the laser unit frame. The elements of $\mathbf{r}_l^{lu}(\mathbf{t})$ can be used to determine the mirror scan angle β according to Figure 2.9 through basic trigonometry.

$$\begin{aligned}
& J_x \delta x_b \\
&= \begin{bmatrix} \cos(\kappa(t)) \delta \Delta X - \sin(\kappa(t)) \delta \Delta Y \\ \sin(\kappa(t)) \delta \Delta X + \cos(\kappa(t)) \delta \Delta Y \\ \delta \Delta Z \end{bmatrix} \\
&+ \begin{bmatrix} \sin(\kappa(t)) z(t) \delta \Delta \omega + \cos(\kappa(t)) z(t) \delta \Delta \varphi - \sin(\kappa(t)) x(t) \delta \Delta \kappa \\ -\cos(\kappa(t)) z(t) \delta \Delta \omega + \sin(\kappa(t)) z(t) \delta \Delta \varphi + \cos(\kappa(t)) x(t) \delta \Delta \kappa \\ -x(t) \delta \Delta \varphi \end{bmatrix} \quad (2.39) \\
&+ \begin{bmatrix} -\cos(\kappa(t)) \sin(S\beta(t)) \delta \Delta \rho + \cos(\kappa(t)) z(t) \beta(t) \delta S \\ -\sin(\kappa(t)) \sin(S\beta(t)) \delta \Delta \rho + \sin(\kappa(t)) z(t) \beta(t) \delta S \\ -\cos(S\beta(t)) \delta \Delta \rho - x(t) \beta(t) \delta S \end{bmatrix}
\end{aligned}$$

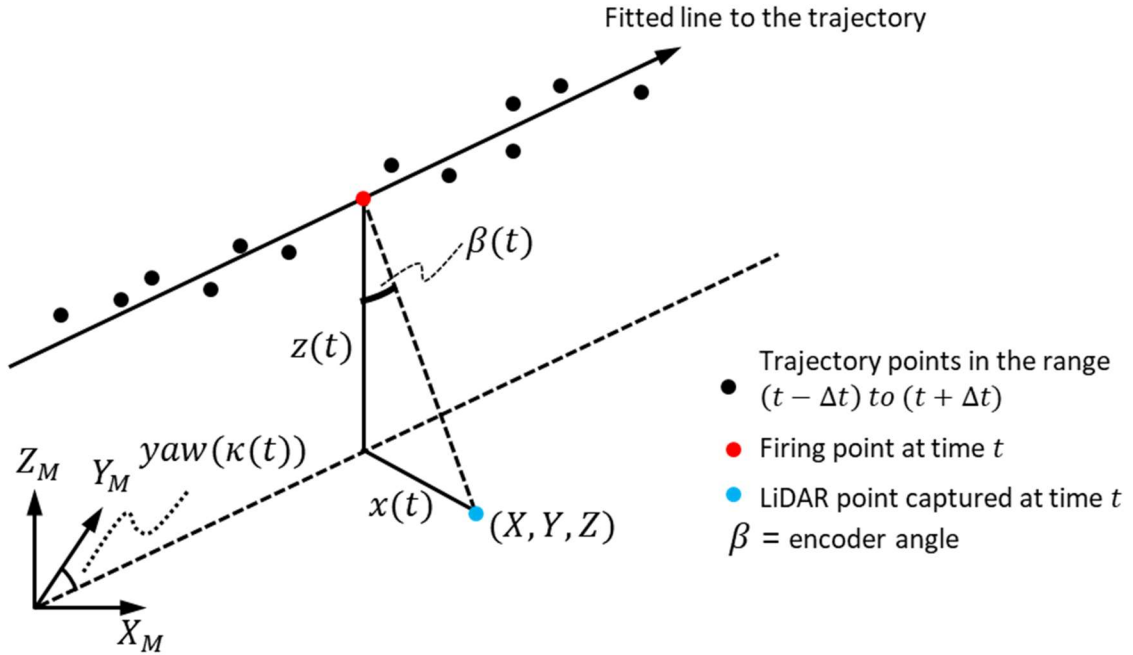


Figure 2.9: Synthesizing the System Raw Measurements for the **QR** Calibration Procedure (adapted from Bang, 2010)

Once the trajectory line fitting, firing point estimation, x -laser unit coordinate and the z -laser unit coordinate calculations are complete, the calibration can be carried out to estimate the system parameter biases. Upon estimation of the system parameter biases, the adjusted coordinates are found by removing their impact $J_x \delta x_b$. The process of removing the impact completes the calibration and it is shown in eq. (2.40), which is evaluated using the biased coordinates, synthesized measurements, and estimated system parameter biases.

$$r_I^m (Adjusted) = r_I^m (Biased) - J_x \delta x_b \quad (2.40)$$

2.4.2.2 Simplified (**S**) Calibration Procedures

The **S** calibration can be used when the system raw measurements are fully unavailable. The **S** calibration is markedly different from the **R** and **QR** approaches because it requires two steps instead of one. The first step compares overlapping strips to determine the

transformation parameters between them, and the second step uses that transformation to perform an estimation of the system parameter biases via a linear relationship. The linear relationship developed is between the system parameters and the discrepancies which are observed when overlapping strips are compared. In other words, the magnitudes and the directions of the observed discrepancies are directly related to the inherent biases in the system parameters. However, such a mathematical relationship is only derived through the use of assumptions, which are listed below:

- Terrain elevation variation should be much smaller when compared with the flying height. Given this assumption, the z -laser unit coordinate of the LiDAR point with respect to the laser unit frame, $\mathbf{z}(\mathbf{t})$, can be assumed to be constant and denoted as \mathbf{z} , which is equivalent to $-\mathbf{H}$.
- We are dealing with a linear vertical scanner that maps the terrain across the flight direction (i.e. the pitch and roll are approximately 0°). Therefore, the coordinates of a given point \mathbf{I} relative to the laser unit coordinate system $\mathbf{r}_I^{lu}(\mathbf{t})$ would be represented by eq. (2.41), where $\mathbf{x}(\mathbf{t})$ and \mathbf{z} are the x -laser unit coordinate, and the z -laser unit coordinate of the LiDAR point with respect to the laser unit frame.

$$\mathbf{r}_I^{lu}(\mathbf{t}) = \begin{bmatrix} \mathbf{x}(\mathbf{t}) \\ 0 \\ \mathbf{z} \end{bmatrix} \quad (2.41)$$

- The xy -axes of the mapping reference frame will be defined at the average terrain elevation.
- The xy -axes of the mapping reference will be defined such that the y -axis is half-way between the flight lines in question and aligned along the flight direction, ensuring that the strips are flown in the South-to-North and North-to-South directions.

In addition to these assumptions, the \mathcal{S} calibration also has expectations about the location and orientation of the IMU body frame and laser unit coordinate systems. It is important to note that these expectations can always be met by introducing virtual coordinate systems,

and therefore they are not required in order to carry out the calibration. First, it is expected that the IMU body frame is aligned with its \mathbf{x}_b , \mathbf{y}_b , and \mathbf{z}_b axes pointing along starboard, flight, and up directions, respectively. Also, the IMU body frame and the laser unit coordinate systems are expected to be almost parallel and close to each other with small boresight angles $(\Delta\omega, \Delta\varphi, \Delta\kappa)$ and a small lever arm offset $(\Delta X, \Delta Y, \Delta Z)$ describing their rotational and translational relationship, respectively. With these coordinate system expectations and the listed assumptions, the LiDAR point-positioning equation simplifies to the form in eq. (2.42). Some of the terms in eq. (2.42) have double signage, the upper sign is used if the strip has a South-to-North flight direction (denoted as *forward*), and the bottom sign is used if the strip has a North-to-South flight direction (denoted as *backward*).

$$\mathbf{r}_l^m(t) = \mathbf{r}_b^m(t) + \begin{bmatrix} \pm\Delta x \\ \pm\Delta y \\ \Delta z \end{bmatrix} + \begin{bmatrix} \pm 1 & \mp\Delta\kappa & \pm\Delta\varphi \\ \pm\Delta\kappa & \pm 1 & \mp\Delta\omega \\ -\Delta\varphi & \Delta\omega & 1 \end{bmatrix} \begin{bmatrix} \mathbf{x}(t) \\ 0 \\ -H \end{bmatrix} \quad (2.42)$$

The \mathcal{S} method uses biased point cloud coordinates, and therefore the biased representation of eq. (2.42) should be formed. This is done in the same manner as in the \mathcal{QR} procedure and is shown in eq. (2.43). Eq. (2.43) accounts for the biases in the system parameters $\delta\mathbf{x}_b$ and the noise in the system measurements \mathbf{e} . The noise free system measurements are represented as \mathbf{y}_{nf} , the true value of the system parameters is represented as \mathbf{x} , and the time tag of the point in question as \mathbf{t} . To be used in the calibration, this equation is linearized, resulting in eq. (2.44). Eq. (2.45) is formed from eq. (2.44) and uses the relationship $\mathbf{r}_l^m(\mathbf{t}) = \mathbf{f}(\mathbf{x}, \mathbf{y}_{nf})$ to define the relationship between the true coordinates, $\mathbf{r}_l^m(\mathbf{t})$, and the biased coordinates, $\mathbf{r}_l^m(\mathbf{t}, \mathbf{biased})$. The Jacobian matrix in eq. (2.44) and eq. (2.45) is found by taking the derivative of eq. (2.42) with respect to the system parameters. With that Jacobian matrix, the impact of the system parameter biases on the derived coordinates $\mathbf{J}_x\delta\mathbf{x}_b$ can be formed and is shown in eq. (2.46). Eq. (2.45) and eq. (2.46) are then used to develop the discrepancy equations representing the mathematical relationship between conjugate points in overlapping strips. In developing the discrepancy equations, the \mathbf{A} and \mathbf{B} subscripts denote the two different overlapping strips; there is also an \mathbf{f} and \mathbf{b} notation to denote whether each strip is flying in the *forward* or *backward*

direction, respectively. Eq. (2.47) is the discrepancy equation representing the strip-pair with opposite flying directions, and eq. (2.48) is the discrepancy equation for a strip-pair with flights in the same direction. The current implementation of the \mathcal{S} calibration does not incorporate control and therefore does not have a discrepancy equation for that scenario, as the other calibration approaches do.

$$r_I^m(t, \text{biased}) = f(x + \delta x_b, y_{nf} + e, t) \quad (2.43)$$

$$r_I^m(t, \text{biased}) \approx f(x, y_{nf}) + J_x \delta x_b + J_y e \quad (2.44)$$

$$r_I^m(t, \text{biased}) = r_I^m(t) + J_x \delta x_b + J_y e \quad (2.45)$$

$$J_x \delta x_b = \begin{bmatrix} \pm \delta \Delta X \mp H \delta \Delta \varphi \mp \sin(S\beta) \delta \Delta \rho \mp H \beta \delta S \\ \pm \delta \Delta Y \mp H \delta \Delta \omega \pm \delta \Delta \kappa \\ \delta \Delta Z - x \delta \Delta \varphi - \cos(S\beta) \delta \Delta \rho - x \beta \delta S \end{bmatrix} \quad (2.46)$$

$$r_{I_A}^m(t_A, f, \text{biased}) - r_{I_B}^m(t_B, b, \text{biased}) =$$

$$\begin{bmatrix} a \\ 2\delta \Delta y + 2H\delta \Delta \omega + (x_A(t_A) + x_B(t_B))\delta \Delta \kappa \\ b \end{bmatrix}, \text{ where}$$

$$a = 2\delta \Delta x - 2H \delta \Delta \varphi - (\sin(S\beta_A(t_A)) + \sin(S\beta_B(t_B))) \delta \Delta \rho - H(\beta_A(t_A) + \beta_B(t_B))\delta S \quad (2.47)$$

$$b = -(x_A(t_A) - x_B(t))\delta \Delta \varphi - (\cos(S\beta_A(t_A)) - \cos(S\beta_B(t)))\delta \Delta \rho - (x_A(t_A)\beta_A(t_A) - x_B(t_B)\beta_B(t_B))\delta S$$

$$r_{I_A}^m(t_A, f, \text{biased}) - r_{I_B}^m(t_B, f, \text{biased}) = \begin{bmatrix} \left(-\sin(S\beta_A(t_A)) + \sin(S\beta_B(t_B)) \right) \delta\Delta\rho - H(\beta_A(t_A) - \beta_B(t_B))\delta S \\ (x_A(t_A) - x_B(t_B))\delta\Delta\kappa \\ -(x_A(t_A) - x_B(t_B))\delta\Delta\varphi - (x_A(t_A)\beta_A(t_A) - x_B(t_B)\beta_B(t_B))\delta S \end{bmatrix} \quad (2.48)$$

In order to remove the need for the raw measurements, the following steps are used to reformulate the discrepancy equations. In these steps, the compact representations of a biased point $\mathbf{r}_{I_A}^m(t_A, \mathbf{f}, \text{biased})$ and $\mathbf{r}_{I_B}^m(t_B, \mathbf{b}, \text{biased})$ are switched to their full vector form, as seen in eq. (2.49), for the remainder of this section.

$$r_{I_A}^m(t_A, f, \text{biased}) - r_{I_B}^m(t_B, b, \text{biased}) = \begin{bmatrix} X_{I_A}^m(t_A, f, \text{biased}) \\ Y_{I_A}^m(t_A, f, \text{biased}) \\ Z_{I_A}^m(t_A, f, \text{biased}) \end{bmatrix} - \begin{bmatrix} X_{I_B}^m(t_B, b, \text{biased}) \\ Y_{I_B}^m(t_B, b, \text{biased}) \\ Z_{I_B}^m(t_B, b, \text{biased}) \end{bmatrix} \quad (2.49)$$

Reformulation of discrepancy equation (2.47) (overlapping strips flying in opposite directions) starts with the expression $(\sin(S\beta_A(t_A)) + \sin(S\beta_B(t_B)))\delta\Delta\rho$. It is assumed that within the nominal scan angle of a LiDAR system (range of 0°- 30°), the differences between the sine and the tangent of an angle are small enough to be ignored, and therefore can be used interchangeably in this expression. With this assumption, the tangent of the scan angles are rewritten as the ratios in eq. (2.50) and eq. (2.51), and they are used to rewrite the expression as shown in eq. (2.52).

$$\tan(S\beta_A(t_A)) = -\frac{x_A(t_A)}{H} \quad (2.50)$$

$$\tan(S\beta_B(t_B)) = -\frac{x_B(t_B)}{H} \quad (2.51)$$

$$\begin{aligned}
& \left(\sin(S\beta_A(t_A)) + \sin(S\beta_B(t_B)) \right) \delta\Delta\rho \\
& \approx \left(\tan(S\beta_A(t_A)) + \tan(S\beta_B(t_B)) \right) \delta\Delta\rho \\
& = \left(-\frac{x_A(t_A)}{H} - \frac{x_B(t_B)}{H} \right) \delta\Delta\rho \tag{2.52} \\
& = -\left(\frac{x_A(t_A) + x_B(t_B)}{H} \right) \delta\Delta\rho
\end{aligned}$$

Figure 2.10 shows the two scenarios that use this discrepancy equation (2.47). The term, \mathbf{D} , is the lateral distance between the two flight lines, and the *forward* and *backward* flight lines are denoted by \mathbf{A} and \mathbf{B} , respectively. In the first scenario, \mathbf{B} is to the right of \mathbf{A} and denoted as \mathbf{B}_R . In the second scenario, \mathbf{B} is to the left of \mathbf{A} and denoted as \mathbf{B}_L . To represent both scenarios in the following equations, the top and bottom signs are used for the \mathbf{B}_R and \mathbf{B}_L scenarios, respectively. It can be seen in Figure 2.10 that in the \mathbf{B}_R scenario the expression $(x_A(t_A) + x_B(t_B))$ is equivalent to \mathbf{D} and in the \mathbf{B}_L scenario it is equivalent to $-\mathbf{D}$ (as is shown in eq. (2.53)). Applying this equivalency to eq. (2.52) reduces it to eq. (2.54), and further simplification is seen in eq. (2.55) by assuming $\beta_A(t_A) = -\frac{x_A(t_A)}{H}$ and $\beta_B(t_B) = -\frac{x_B(t_B)}{H}$.

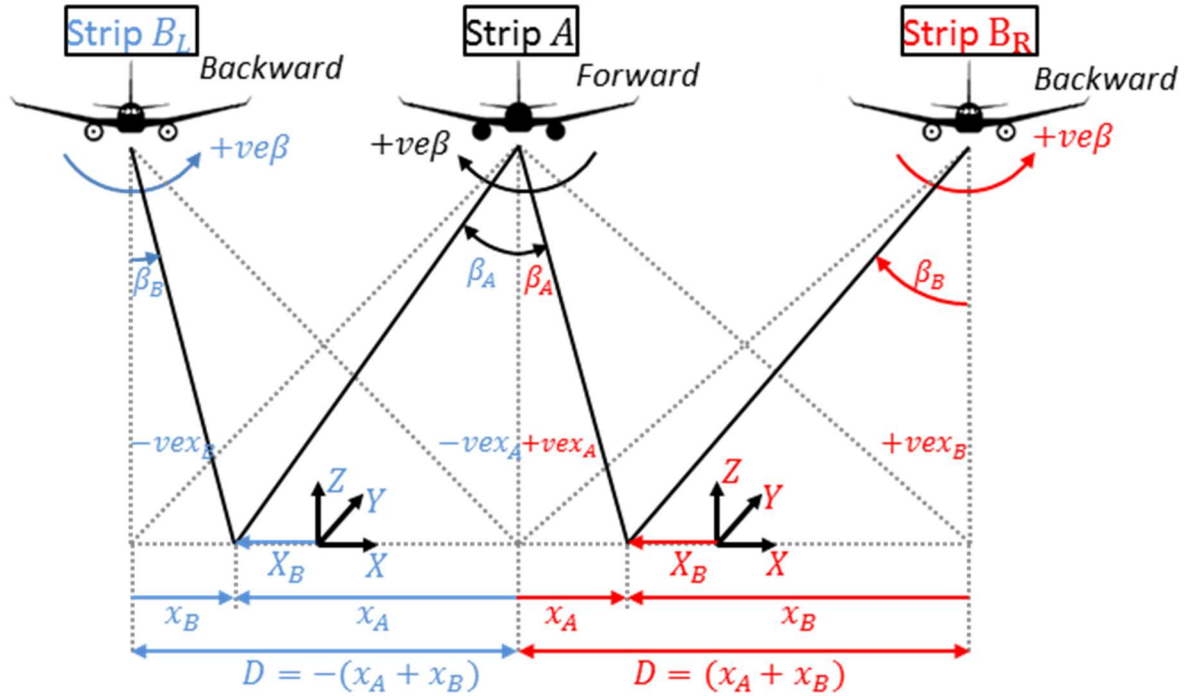


Figure 2.10: An Object Point and its Measurements Observed from the Two Different Scenarios of Overlapping Strips flown in Opposite Directions (A & B_L , A & B_R) (adapted from Bang, 2010)

$$(x_A(t_A) + x_B(t_B)) = \pm D \quad (2.53)$$

$$\left(\sin(S\beta_A(t_A)) + \sin(S\beta_B(t_B)) \right) \delta\Delta\rho = \left(\mp \frac{D}{H} \right) \delta\Delta\rho \quad (2.54)$$

$$(\beta_A(t_A) + \beta_B(t_B)) = \mp \frac{D}{H} \quad (2.55)$$

The expression $\cos(S\beta(t)) \delta\Delta\rho$, in eq. (2.47) does not significantly change within the nominal scan angle range of 0° - 30° ; therefore, $(\cos(S\beta_A(t_A)) - \cos(S\beta_B(t_B)))\delta\Delta\rho$ can be reduced to zero. With that expression cancelling out, the discrepancy equation for overlapping strips flying in opposite directions can be represented as eq. (2.56).

$$\begin{aligned}
& \begin{bmatrix} X_{I_A}^m(t_A, f, \text{biased}) \\ Y_{I_A}^m(t_A, f, \text{biased}) \\ Z_{I_A}^m(t_A, f, \text{biased}) \end{bmatrix} - \begin{bmatrix} X_{I_B}^m(t_B, b, \text{biased}) \\ Y_{I_B}^m(t_B, b, \text{biased}) \\ Z_{I_B}^m(t_B, b, \text{biased}) \end{bmatrix} \\
& = \begin{bmatrix} 2\delta\Delta x - 2H \delta\Delta\varphi \pm \frac{D}{H} \delta\Delta\rho \pm D\delta S \\ 2\delta\Delta y + 2H\delta\Delta\omega \pm D\delta\Delta\kappa \\ -(x_A(t_A) - x_B(t_B))\delta\Delta\varphi - (x_A(t_A)\beta_A(t_A) - x_B(t_B)\beta_B(t_B))\delta S \end{bmatrix} \quad (2.56)
\end{aligned}$$

From Figure 2.10, the equivalency in eq. (2.57) can be observed, and the term $\mathbf{X}_B(t_B)$ represents $\mathbf{X}_{I_B}^m$. Considering eq. (2.57), as well as the equivalencies in eq. (2.53) and $\beta_A(t_A) = -\frac{x_A(t_A)}{H}$ and $\beta_B(t_B) = -\frac{x_B(t_B)}{H}$, the expression $(x_A(t_A)\beta_A(t_A) - x_B(t_B)\beta_B(t_B))$ from eq. (2.56), simplifies to eq. (2.58). Given eq. (2.57) and eq. (2.58), the discrepancy equation (2.56) simplifies into eq. (2.59).

$$(x_A(t_A) - x_B(t_B)) = 2X_B(t_B) \quad (2.57)$$

$$(x_A(t_A)\beta_A(t_A) - x_B(t_B)\beta_B(t_B)) = \mp 2X_B(t_B) \frac{D}{H} \quad (2.58)$$

$$\begin{aligned}
& \begin{bmatrix} X_{I_A}^m(t_A, f, \text{biased}) \\ Y_{I_A}^m(t_A, f, \text{biased}) \\ Z_{I_A}^m(t_A, f, \text{biased}) \end{bmatrix} - \begin{bmatrix} X_{I_B}^m(t_B, b, \text{biased}) \\ Y_{I_B}^m(t_B, b, \text{biased}) \\ Z_{I_B}^m(t_B, b, \text{biased}) \end{bmatrix} \\
& = \begin{bmatrix} 2\delta\Delta x - 2H \delta\Delta\varphi \pm \frac{D}{H} \delta\Delta\rho \pm D\delta S \\ 2\delta\Delta y + 2H\delta\Delta\omega \pm D\delta\Delta\kappa \\ -2X_B(t_B)\delta\Delta\varphi \pm 2X_B(t_B) \frac{D}{H} \delta S \end{bmatrix} \quad (2.59)
\end{aligned}$$

To further simplify eq. (2.59), it is observed that the third row of this equation represents the impact that the biases have on the vertical discrepancy between conjugate points. This

vertical impact can be reformulated as a rotation around the flying direction through the following steps. First, the discrepancy equation can be written as a sum of two vectors, as seen in eq. (2.60). Next, the biased coordinates in the *forward* flight can be expressed in terms of the conjugate point in the *backward* flight line. This relationship is expressed in eq. (2.61) (this assumes that $\mathbf{X}_{I_B}^m(\mathbf{b}, \mathbf{biased})$ is equivalent to \mathbf{X}_I^m , this replaces the exact equality with an approximate equality).

$$\begin{aligned}
& \begin{bmatrix} X_{I_A}^m(t_A, f, \mathbf{biased}) \\ Y_{I_A}^m(t_A, f, \mathbf{biased}) \\ Z_{I_A}^m(t_A, f, \mathbf{biased}) \end{bmatrix} - \begin{bmatrix} X_{I_B}^m(t_B, b, \mathbf{biased}) \\ Y_{I_B}^m(t_B, b, \mathbf{biased}) \\ Z_{I_B}^m(t_B, b, \mathbf{biased}) \end{bmatrix} \\
&= \begin{bmatrix} 2\delta\Delta x - 2H \delta\Delta\varphi \pm \frac{D}{H} \delta\Delta\rho \pm D\delta S \\ 2\delta\Delta y + 2H\delta\Delta\omega \pm D\delta\Delta\kappa \\ 0 \end{bmatrix} \\
&+ \begin{bmatrix} 0 \\ 0 \\ -2X_B(t_B)\delta\Delta\varphi \pm 2X_B(t_B)\frac{D}{H}\delta S \end{bmatrix}
\end{aligned} \tag{2.60}$$

$$\begin{aligned}
& \begin{bmatrix} X_{I_A}^m(t_A, f, \mathbf{biased}) \\ Y_{I_A}^m(t_A, f, \mathbf{biased}) \\ Z_{I_A}^m(t_A, f, \mathbf{biased}) \end{bmatrix} \\
&\approx \begin{bmatrix} 2\delta\Delta x - 2H \delta\Delta\varphi \pm \frac{D}{H} \delta\Delta\rho \pm D\delta S \\ 2\delta\Delta y + 2H\delta\Delta\omega \pm D\delta\Delta\kappa \\ 0 \end{bmatrix} \\
&+ \begin{bmatrix} 0 \\ 0 \\ -2X_B(t_B)\delta\Delta\varphi \pm 2X_B(t_B)\frac{D}{H}\delta S \end{bmatrix} \\
&+ \begin{bmatrix} X_{I_B}^m(t_B, b, \mathbf{biased}) \\ Y_{I_B}^m(t_B, b, \mathbf{biased}) \\ Z_{I_B}^m(t_B, b, \mathbf{biased}) \end{bmatrix}
\end{aligned} \tag{2.61}$$

The addition of the last two vectors in eq. (2.61) can be rewritten as a matrix multiplication. This equivalency is shown in eq. (2.62), and substituting this into the discrepancy equation results in eq. (2.63).

$$\begin{aligned} & \begin{bmatrix} 0 \\ 0 \\ -2X_B(t_B)\delta\Delta\varphi \pm 2X_B(t_B)\frac{D}{H}\delta S \end{bmatrix} + \begin{bmatrix} X_{I_B}^m(t_B, b, biased) \\ Y_{I_B}^m(t_B, b, biased) \\ Z_{I_B}^m(t_B, b, biased) \end{bmatrix} \\ &= \begin{bmatrix} 1 & 0 & 2\delta\Delta\varphi \mp 2\frac{D}{H}\delta S \\ 0 & 1 & 0 \\ -2\delta\Delta\varphi \pm 2\frac{D}{H}\delta S & 0 & 1 \end{bmatrix} \begin{bmatrix} X_{I_B}^m(t_B, b, biased) \\ Y_{I_B}^m(t_B, b, biased) \\ Z_{I_B}^m(t_B, b, biased) \end{bmatrix} \end{aligned} \quad (2.62)$$

$$\begin{aligned} & \begin{bmatrix} X_{I_A}^m(t_A, f, biased) \\ Y_{I_A}^m(t_A, f, biased) \\ Z_{I_A}^m(t_A, f, biased) \end{bmatrix} \\ & \approx \begin{bmatrix} 2\delta\Delta x - 2H\delta\Delta\varphi \pm \frac{D}{H}\delta\Delta\rho \pm D\delta S \\ 2\delta\Delta y + 2H\delta\Delta\omega \pm D\delta\Delta\kappa \\ 0 \end{bmatrix} \\ & + \begin{bmatrix} 1 & 0 & 2\delta\Delta\varphi \mp 2\frac{D}{H}\delta S \\ 0 & 1 & 0 \\ -2\delta\Delta\varphi \pm 2\frac{D}{H}\delta S & 0 & 1 \end{bmatrix} \begin{bmatrix} X_{I_B}^m(t_B, b, biased) \\ Y_{I_B}^m(t_B, b, biased) \\ Z_{I_B}^m(t_B, b, biased) \end{bmatrix} \end{aligned} \quad (2.63)$$

Now, the middle matrix on the right side of eq. (2.63) will be converted to the rotation matrix about the flying direction seen in eq. (2.64). The $\mathbf{sin}(-2\delta\Delta\varphi)$ and $\mathbf{sin}(\pm 2\frac{D}{H}\delta S)$, approximate to $-2\delta\Delta\varphi$ and $\pm 2\frac{D}{H}\delta S$, respectively, and the values for $\mathbf{cos}(-2\delta\Delta\varphi)$ and $\mathbf{cos}(\pm 2\frac{D}{H}\delta S)$ are close to 1.0 since the angular values are small. The multiplication of $2\delta\Delta\varphi \mp 2\frac{D}{H}\delta S$ and $Z_{I_B}^m(t_B, b, biased)$ can be assumed to be very small and almost equivalent to zero due to the assumption of relatively flat terrain and the user defined coordinate system. From these conclusions, the rotation matrix about the flying direction

by an angle of $2\delta\Delta\phi \mp 2\frac{D}{H}\delta S$ is formed, $\mathbf{R}_{(0, 2\delta\Delta\phi \mp 2\frac{D}{H}\delta S, 0)}$. The final form of the discrepancy equation for two overlapping strips flown in opposite directions is eq. (2.64), when there is 100% overlap the equation simplifies to eq. (2.65) (because \mathbf{D} will be equal to zero).

$$\begin{aligned}
& \begin{bmatrix} X_{I_A}^m(t_A, f, biased) \\ Y_{I_A}^m(t_A, f, biased) \\ Z_{I_A}^m(t_A, f, biased) \end{bmatrix} \\
& \approx \begin{bmatrix} 2\delta\Delta x - 2H \delta\Delta\phi \pm \frac{D}{H} \delta\Delta\rho \pm D\delta S \\ 2\delta\Delta y + 2H\delta\Delta\omega \pm D\delta\Delta\kappa \\ 0 \end{bmatrix} \\
& + \begin{bmatrix} 1 & 0 & +2\delta\Delta\phi \mp 2\frac{D}{H}\delta S \\ 0 & 1 & 0 \\ -2\delta\Delta\phi \pm 2\frac{D}{H}\delta S & 0 & 1 \end{bmatrix} \begin{bmatrix} X_{I_B}^m(t_B, b, biased) \\ Y_{I_B}^m(t_B, b, biased) \\ Z_{I_B}^m(t_B, b, biased) \end{bmatrix} \quad (2.64) \\
& = \begin{bmatrix} 2\delta\Delta x - 2H \delta\Delta\phi \pm \frac{D}{H} \delta\Delta\rho \pm D\delta S \\ 2\delta\Delta y + 2H\delta\Delta\omega \pm D\delta\Delta\kappa \\ 0 \end{bmatrix} \\
& + R_{y(2 \Delta\phi \mp 2\frac{D}{H} S)} \begin{bmatrix} X_{I_B}^m(t_B, b, biased) \\ Y_{I_B}^m(t_B, b, biased) \\ Z_{I_B}^m(t_B, b, biased) \end{bmatrix}
\end{aligned}$$

$$\begin{aligned}
& \begin{bmatrix} X_{I_A}^m(t_A, f, biased) \\ Y_{I_A}^m(t_A, f, biased) \\ Z_{I_A}^m(t_A, f, biased) \end{bmatrix} \approx \begin{bmatrix} 2\delta\Delta x - 2H \delta\Delta\phi \\ 2\delta\Delta y + 2H\delta\Delta\omega \\ 0 \end{bmatrix} + \\
& R_{y(2 \Delta\phi)} \begin{bmatrix} X_{I_B}^m(t_B, b, biased) \\ Y_{I_B}^m(t_B, b, biased) \\ Z_{I_B}^m(t_B, b, biased) \end{bmatrix} \quad (2.65)
\end{aligned}$$

Now, reformulation of the discrepancy equation for overlapping strips flying in the same direction (2.48), is completed with similar steps using Figure 2.11 (now strip A and strip

B are both *forward* flights). The equivalencies in eq. (2.66) and eq. (2.67) can be observed from Figure 2.11.

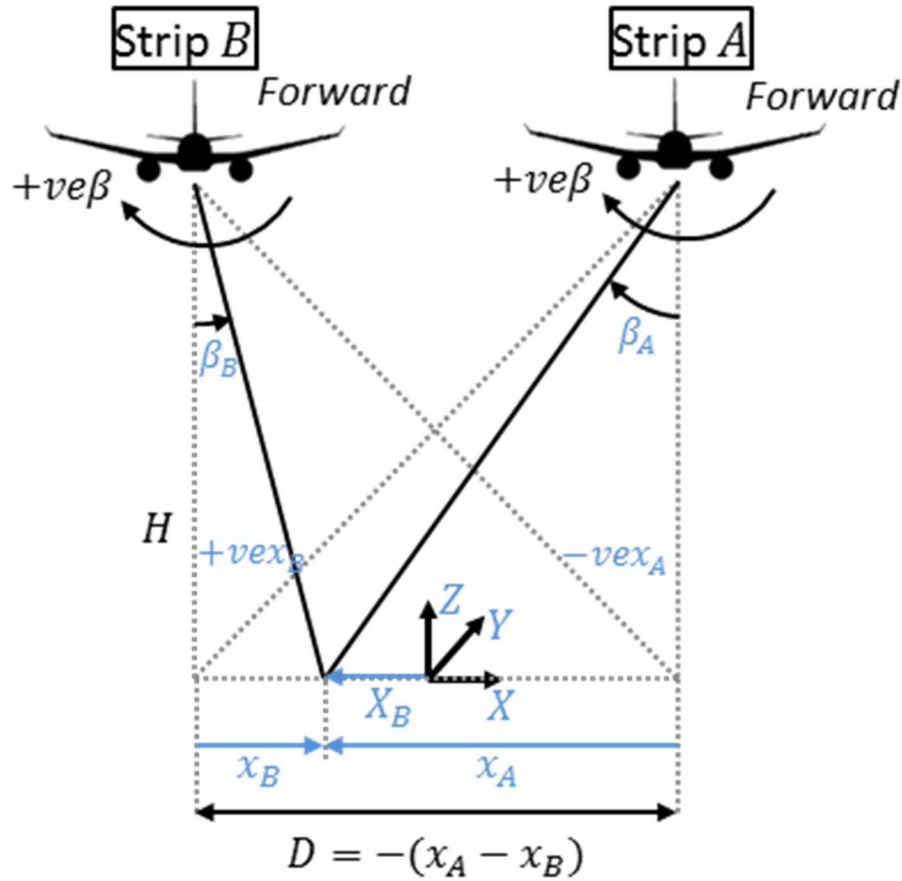


Figure 2.11: An Object Point and its Measurements Observed from Overlapping Strips Flown in the Same Direction (adapted from Bang, 2010)

$$(x_A(t_A) - x_B(t_B)) = -D \quad (2.66)$$

$$(x_A(t_A) + x_B(t_B)) = 2X_B(t_B) \quad (2.67)$$

Starting with the expression $(-\sin(S\beta_A(t_A)) + \sin(S\beta_B(t_B)))\delta\Delta\rho$ from eq. (2.48), it is assumed that within the nominal scan angle range of 0° - 30° , the differences between the sine and the tangent of an angle are small enough to be ignored, and therefore can be used

interchangeably. With this assumption, the tangent of the scan angles are rewritten as the ratios in eq. (2.50) and eq. (2.51), and they are used to rewrite the expression as shown in eq. (2.68). Which is further simplified to eq. (2.69) and then (2.70) using eq. (2.66) and the assumptions $\beta_A(t_A) = -\frac{x_A(t_A)}{H}$ and $\beta_B(t_B) = -\frac{x_B(t_B)}{H}$, respectively.

$$\begin{aligned} & \left(-\sin(S\beta_A(t_A)) + \sin(S\beta_B(t_B)) \right) \delta\Delta\rho \\ & \approx \left(-\tan(S\beta_A(t_A)) + \tan(S\beta_B(t_B)) \right) \delta\Delta\rho \quad (2.68) \\ & = \left(\frac{x_A(t_A)}{H} - \frac{x_B(t_B)}{H} \right) \delta\Delta\rho \end{aligned}$$

$$\left(-\sin(S\beta_A(t_A)) + \sin(S\beta_B(t_B)) \right) \delta\Delta\rho \approx -\frac{D}{H} \delta\Delta\rho \quad (2.69)$$

$$\left(\beta_A(t_A) - \beta_B(t_B) \right) = \frac{D}{H} \quad (2.70)$$

Next, the expression $(x_A(t_A)\beta_A(t_A) - x_B(t_B)\beta_B(t_B))$ from eq. (2.48) is simplified to eq. (2.71) using the equivalencies in eq. (2.66) and eq. (2.67), and the assumptions $\beta_A(t_A) = -\frac{x_A(t_A)}{H}$ and $\beta_B(t_B) = -\frac{x_B(t_B)}{H}$. With eq. (2.70) and eq. (2.71), the discrepancy equation is now of the form in eq. (2.72).

$$\left(x_A(t_A)\beta_A(t_A) - x_B(t_B)\beta_B(t_B) \right) = \frac{D}{H} 2x_B(t_B) \quad (2.71)$$

$$\begin{aligned}
& \begin{bmatrix} X_{I_A}^m(t_A, f, biased) \\ Y_{I_A}^m(t_A, f, biased) \\ Z_{I_A}^m(t_A, f, biased) \end{bmatrix} - \begin{bmatrix} X_{I_B}^m(t_B, f, biased) \\ Y_{I_B}^m(t_B, f, biased) \\ Z_{I_B}^m(t_B, f, biased) \end{bmatrix} \\
& = \begin{bmatrix} -\frac{D}{H} \delta \Delta \rho - D \delta S \\ -D \delta \Delta \kappa \\ D \delta \Delta \varphi - \frac{D}{H} 2X_B(t_B) \delta S \end{bmatrix} \quad (2.72)
\end{aligned}$$

To further simplify eq. (2.72), it is observed that the third row of this equation represents the impact that the biases have on the vertical discrepancy between conjugate points, and this impact can be reformulated as rotation around the flying direction of the mapping frame through using the same logic as was used with the previous discrepancy equation. The right side of the discrepancy equation can be written as a sum of two vectors and the biased coordinates in the *forward* flight can be expressed in terms of the conjugate point in the *backward* flight line. These steps are reflected in eq. (2.73). Next, the addition of the last two vectors in eq. (2.73) can be rewritten as a matrix multiplication. This equivalency is shown in eq. (2.74), and substituting this into the discrepancy equation results in eq. (2.75).

$$\begin{aligned}
& \begin{bmatrix} X_{I_A}^m(t_A, f, biased) \\ Y_{I_A}^m(t_A, f, biased) \\ Z_{I_A}^m(t_A, f, biased) \end{bmatrix} \\
& \approx \begin{bmatrix} -\frac{D}{H} \delta \Delta \rho - D \delta S \\ -D \delta \Delta \kappa \\ D \delta \Delta \varphi \end{bmatrix} + \begin{bmatrix} 0 \\ 0 \\ -\frac{D}{H} 2X_B(t_B) \delta S \end{bmatrix} \quad (2.73) \\
& + \begin{bmatrix} X_{I_A}^m(t_B, f, biased) \\ Y_{I_A}^m(t_B, f, biased) \\ Z_{I_A}^m(t_B, f, biased) \end{bmatrix}
\end{aligned}$$

$$\begin{aligned}
& \begin{bmatrix} 0 \\ 0 \\ -\frac{D}{H}2X_B(t_B)\delta S \end{bmatrix} + \begin{bmatrix} X_{I_A}^m(t_B, f, \text{biased}) \\ Y_{I_A}^m(t_B, f, \text{biased}) \\ Z_{I_A}^m(t_B, f, \text{biased}) \end{bmatrix} \\
& = \begin{bmatrix} 1 & 0 & 0 \\ 0 & 1 & 0 \\ -2\frac{D}{H}\delta S & 0 & 1 \end{bmatrix} \begin{bmatrix} X_{I_A}^m(t_B, f, \text{biased}) \\ Y_{I_A}^m(t_B, f, \text{biased}) \\ Z_{I_A}^m(t_B, f, \text{biased}) \end{bmatrix}
\end{aligned} \tag{2.74}$$

$$\begin{aligned}
& \begin{bmatrix} X_{I_A}^m(t_A, f, \text{biased}) \\ Y_{I_A}^m(t_A, f, \text{biased}) \\ Z_{I_A}^m(t_A, f, \text{biased}) \end{bmatrix} \\
& \approx \begin{bmatrix} -\frac{D}{H}\delta\Delta\rho - D\delta S \\ -D\delta\Delta\kappa \\ D\delta\Delta\varphi \end{bmatrix} \\
& + \begin{bmatrix} 1 & 0 & 0 \\ 0 & 1 & 0 \\ -2\frac{D}{H}\delta S & 0 & 1 \end{bmatrix} \begin{bmatrix} X_{I_A}^m(t_B, f, \text{biased}) \\ Y_{I_A}^m(t_B, f, \text{biased}) \\ Z_{I_A}^m(t_B, f, \text{biased}) \end{bmatrix}
\end{aligned} \tag{2.75}$$

Now, the middle matrix on the right side of eq. (2.75) will be converted to the rotation matrix about the flying direction seen in eq. (2.63). The $\sin(-2\delta\Delta\varphi)$ and $\sin(\pm 2\frac{D}{H}\delta S)$, approximate to $-2\delta\Delta\varphi$ and $\pm 2\frac{D}{H}\delta S$, respectively, and the values for $\cos(-2\delta\Delta\varphi)$ and $\cos(\pm 2\frac{D}{H}\delta S)$ are close to 1.0 since the angular values are small. The multiplication of $2\frac{D}{H}\delta S$ and $Z_{I_B}^m(t_B, f, \text{biased})$ can be assumed to very small and almost equivalent to zero due to the assumption of relatively flat terrain and the use of a user defined coordinate system. From these conclusions, the rotation matrix about the flying direction by an angle of $2\frac{D}{H}\delta S$ is formed, $R_{(0, 2\frac{D}{H}\delta S, 0)}$. The final form of the discrepancy equation for two overlapping strips flown in the same directions is eq. (2.76).

$$\begin{aligned}
& \begin{bmatrix} X_{I_A}^m(t_A, f, \text{biased}) \\ Y_{I_A}^m(t_A, f, \text{biased}) \\ Z_{I_A}^m(t_A, f, \text{biased}) \end{bmatrix} \\
& \approx \begin{bmatrix} -\frac{D}{H} \delta \Delta \rho - D \delta S \\ -D \delta \Delta \kappa \\ D \delta \Delta \varphi \end{bmatrix} \\
& + \begin{bmatrix} 1 & 0 & 2\frac{D}{H} \delta S \\ 0 & 1 & 0 \\ -2\frac{D}{H} \delta S & 0 & 1 \end{bmatrix} \begin{bmatrix} X_{I_A}^m(t_B, f, \text{biased}) \\ Y_{I_A}^m(t_B, f, \text{biased}) \\ Z_{I_A}^m(t_B, f, \text{biased}) \end{bmatrix} \quad (2.76) \\
& = \begin{bmatrix} -\frac{D}{H} \delta \Delta \rho - D \delta S \\ -D \delta \Delta \kappa \\ D \delta \Delta \varphi \end{bmatrix} + R_{y(2\frac{D}{H} S)} \begin{bmatrix} X_{I_A}^m(t_B, f, \text{biased}) \\ Y_{I_A}^m(t_B, f, \text{biased}) \\ Z_{I_A}^m(t_B, f, \text{biased}) \end{bmatrix}
\end{aligned}$$

By observing eq. (2.64) it can be seen that overlapping strips flown in opposite directions introduce a constant shift along the **X** and **Y** directions, as well as a rotation around the flying direction. These shifts and the rotation are related to the biases according to eq. (2.77). This model is general in the sense that it does not assume $\mathbf{D} = \mathbf{0}$. When $\mathbf{D} = \mathbf{0}$, some of the terms cancel out.

$$\begin{bmatrix} X_T \\ Y_T \\ \varphi \end{bmatrix} = \begin{bmatrix} 2\delta \Delta x - 2H \delta \Delta \varphi \pm \frac{D}{H} \delta \Delta \rho \pm D \delta S \\ 2\delta \Delta y + 2H \delta \Delta \omega \pm D \delta \Delta \kappa \\ 2\delta \Delta \varphi \pm 2\frac{D}{H} \delta S \end{bmatrix} \quad (2.77)$$

By observing eq. (2.76) it can be seen that flight lines of the same direction result in a constant shift along the **X**, **Y**, and **Z** directions, and a rotation around the flying direction. These shifts and the rotation are related to the biases according to eq. (2.78).

$$\begin{bmatrix} X_T \\ Y_T \\ Z_T \\ \varphi \end{bmatrix} = \begin{bmatrix} -\frac{D}{H}\delta\Delta\rho - D\delta S \\ -D\delta\Delta\kappa \\ D\delta\Delta\varphi \\ 2\frac{D}{H}\delta S \end{bmatrix} \quad (2.78)$$

In conclusion, the \mathcal{S} calibration procedure relates the detected discrepancies between overlapping strips to the biases in the system parameters, and those discrepancies can be modeled by three shifts and a rotation around the flight direction (Kersting et al, 2012; Bang, 2010). The first step of the \mathcal{S} calibration method determines these transformation parameters (three shifts and a rotation), and the second step determines the system parameter biases through a Least Squares estimation using eq. (2.77) and eq. (2.78). After estimating the system parameter biases, the adjusted coordinates are found by removing the impact of the estimated system parameter biases $\mathbf{J}_x\delta\mathbf{x}_b$. The process of removing the impact is shown in eq. (2.79), which can be derived from the relationship between the true and biased coordinates (eq. (2.45)).

$$\begin{aligned} & r_I^m \text{ Adjusted} \\ & = r_I^m \text{ Biased} - R_{(0,0,\kappa)}^T \\ & * \begin{bmatrix} \delta\Delta X - (H - Z(t))\delta\Delta\varphi - \sin(\beta(t))\delta\Delta\rho - (H - Z(t))\beta(t)\delta S \\ \delta\Delta Y + (H - Z(t))\delta\Delta\omega + x(t)\delta\Delta\kappa \\ \delta\Delta Z - x(t)\delta\Delta\varphi - \cos(\beta(t))\delta\Delta\rho - x(t)\beta(t)\delta S \end{bmatrix} \end{aligned} \quad (2.79)$$

In eq. (2.79), the term \mathbf{H} is the flying height above average terrain elevation, κ is the heading of the flight line in question, and $\mathbf{Z}(t)$, $\mathbf{x}(t)$, and $\beta(t)$ are the elevation, lateral coordinate, and scan angle, respectively, of the point in question. It is necessary to rotate the correction term by the heading of the flight line in question because the term is based on the assumption that the flight direction is parallel to the y-axis of the mapping coordinate system. The trigonometric and spatial relationships needed to synthesize the raw measurements according to the following steps are shown in Figure 2.10 and Figure 2.11.

- The x -laser unit coordinate of the LiDAR point with respect to the laser unit frame $\mathbf{x}(t)$ is determined through the use of the approximate center of scan line. It is the

equivalent to the $\mathbf{X}(t)$ coordinate of the LiDAR point in question, minus/plus half the lateral distance between the two point clouds, \mathbf{D} (appropriate sign depends on the configuration).

- The encoder angle $\beta(t)$ is determined using the flying height, H , the $\mathbf{Z}(t)$ coordinate of the LiDAR point in question, I , and the lateral laser unit coordinate x (i.e. $\beta(t) = -\text{atan}(x(t)/(H - Z(t)))$).

Using these synthesized raw measurements, along with the biased coordinates and estimated system parameter biases, eq. (2.79) can be evaluated, resulting in the adjusted coordinates and thus completing the calibration.

2.4.3 Rigorous and Pseudo-rigorous Calibration Strategies

The implementation of the introduced calibration approaches is shown in Figure 2.12. This figure shows how to use the ICPatch matching process in an *iterative procedure*, and how that *iterative procedure* is slightly different for each approach. The *iterative procedure* refines the matches based on the current estimates of the following values:

- a) System parameters (for the \mathbf{R} approach)
- b) System parameter biases (for the \mathbf{QR} approach)
- c) Transformation parameters (for the \mathbf{S} approach)

In Figure 2.12, the \mathbf{R} and \mathbf{QR} calibration procedures simultaneously solve the matching and system parameters/system parameter biases within the *iterative procedure*, while the \mathbf{S} procedure requires an additional estimation step in order to evaluate the system parameter biases. After finding the point-patch matches through the ICPatch process and determining the estimations listed above, the \mathbf{R} approach updates the coordinates by reconstructing both strips, the \mathbf{QR} updates the coordinates of both strips by removing the impact of the biases, and the \mathbf{S} approach updates the coordinates in strip \mathbf{B} by transforming them (with the resulting rigid-body transformation, 3 shifts and a rotation). After updating the coordinates for all approaches, the primitive matching and parameters estimation are repeated until the change in estimation is smaller than a predefined threshold. After this iterative procedure, the 2nd step of the \mathbf{S} approach is then completed by estimating the system parameter biases. Finally, the initial point cloud coordinates are reconstructed/adjusted for each calibration

approach using the final estimates of the system parameters/system parameter biases. It is important to note that within the *iterative procedure*, the new point-patch matches are used for the estimation step, but the initial coordinate values are used as opposed to the updated coordinate values.

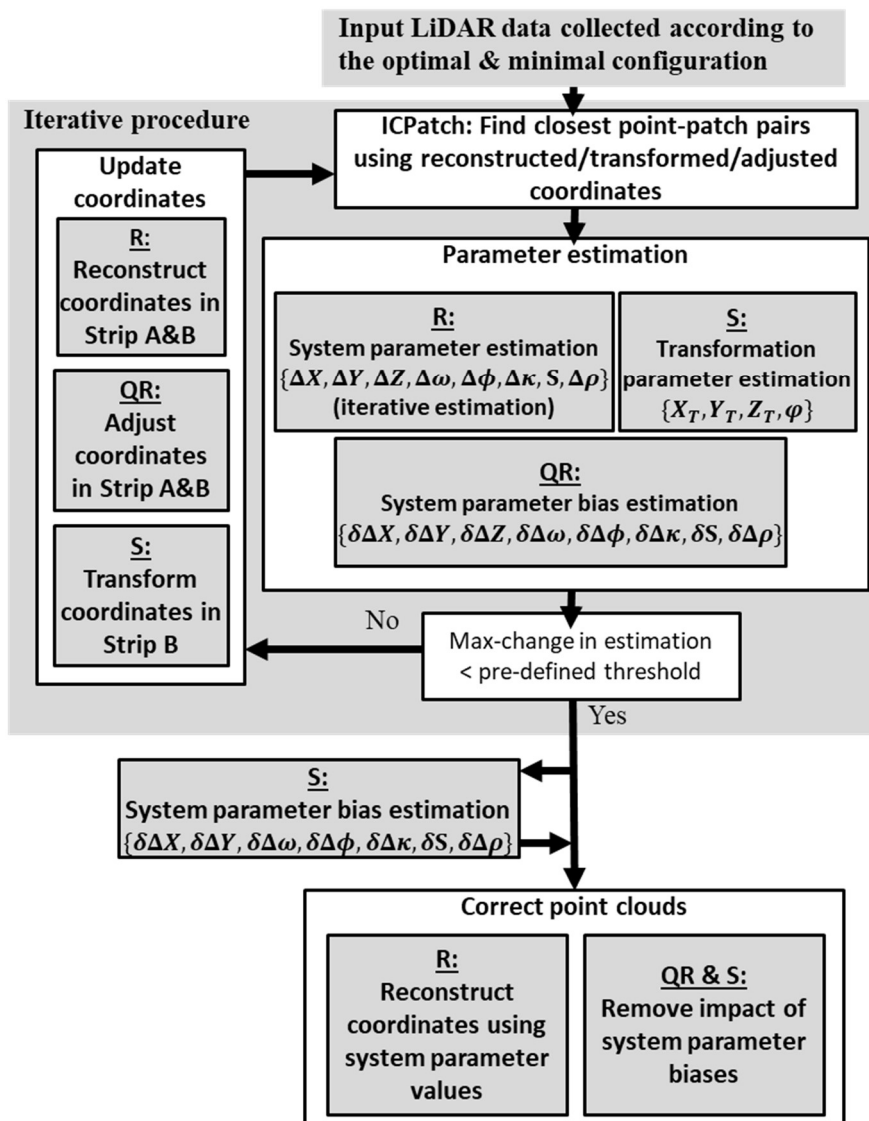


Figure 2.12: Implementation of the R , QR , and S Calibration Procedures

3. METHODOLOGY FOR ADDRESSING RESEARCH OBJECTIVES

3.1 Overview

The research objectives include the development of a new calibration approach, a performance analysis on the *Pseudo-rigorous* approaches, and the development of a strategy for performing a stability analysis. The new calibration approach to be developed has the same data requirements as the \mathcal{S} procedure, but it provides a more robust calibration by combining the two steps of the \mathcal{S} procedure into one comprehensive step. When compared to the \mathcal{S} calibration, the new calibration approach is different because it has the ability to incorporate control, and it has more flexibility in data collection and application by removing certain data assumptions. Development of a LiDAR calibration stability analysis strategy is yet to be addressed in the community, and it is very important now that systems are becoming more compact and readily available. The stability analysis will compare LiDAR system calibration results from two separate times and analyze their impact on the reconstructed point cloud. This portion of the research will give a quantitative approach for understanding the variation in system parameters over time and the optimal calibration frequency.

3.2 Quasi-Rigorous/Quasi-Simplified (*QRQS*) Calibration

This research focuses on developing a one-step calibration algorithm that operates without access to raw measurements, incorporates the sensor model, and can be used for any type of terrain cover. Current approaches do not address these issues simultaneously in one calibration solution (they only address one or two issues). Existing approaches will be used as a reference in discussing the *QRQS* development; namely, the \mathcal{S} , \mathcal{QR} , and \mathcal{R} , which have been developed in previous research by Bang (2010), Habib et al. (2010b), Kersting (2011), and Kersting et al. (2012). The \mathcal{S} calibration is a two-step procedure while the others are one-step. For the new calibration approach developed here, the level of detail needed from the flight collection is the same as the \mathcal{S} calibration (point clouds), but its capabilities are

more similar to that of the *QR*. The strategy associated with the *QRQS* math model has two less assumptions than the *S* approach; the flight lines do not have to be parallel and the terrain variation does not have to be low. In addition to having less assumptions than the *S* approach, this *QRQS* calibration can handle any type of terrain, it is a one-step strategy, and it can incorporate control into the procedure. Incorporating control enables the detection of a bias that significantly affects the vertical component of a point cloud.

3.2.1 Assumptions and Math Model

The *QRQS* calibration can be used when the system raw measurements are fully unavailable. The missing raw measurements for this approach are $\mathbf{r}_b^m(\mathbf{t})$, $\mathbf{R}_b^m(\mathbf{t})$, and $\mathbf{r}_I^{lu}(\mathbf{t})$, and in order to effectively synthesize them, the following assumptions are made:

- a) We are dealing with a linear vertical scanner that maps the terrain across the flight direction (i.e. the pitch and roll are approximately 0°). Therefore, the coordinates of a given point I relative to the laser unit coordinate system, $\mathbf{r}_I^{lu}(\mathbf{t})$, would be represented by eq. (3.1), where $\mathbf{x}(\mathbf{t})$ and $\mathbf{z}(\mathbf{t})$ are the x-laser unit coordinate and the z-laser unit coordinate of the LiDAR point with respect to the laser unit frame, respectively.

$$\mathbf{r}_I^{lu}(\mathbf{t}) = \begin{bmatrix} \mathbf{x}(\mathbf{t}) \\ 0 \\ \mathbf{z}(\mathbf{t}) \end{bmatrix} \quad (3.1)$$

- b) The strips of the individual strip-pairs must be flown in a straight trajectory.

In addition to these assumptions, the *QRQS* calibration also has expectations about the location and orientation of the IMU body frame and laser unit coordinate systems. It is important to note that these expectations can always be met by introducing virtual coordinate systems, and therefore they are not required in order to carry out the calibration. First, it is expected that the IMU body frame is aligned with its \mathbf{x}_b , \mathbf{y}_b , and \mathbf{z}_b axes pointing along starboard, flight, and up directions, respectively. Also, the IMU body frame and the laser unit coordinate systems are expected to be almost parallel and close to each other,

with small boresight angles $(\Delta\omega, \Delta\varphi, \Delta\kappa)$ and small lever arm offset values $(\Delta X, \Delta Y, \Delta Z)$ describing their rotational and translational relationship, respectively. With these coordinate system expectations and the listed assumptions, the LiDAR point-positioning equation simplifies to the form in eq. (3.2). The term $\kappa(t)$ is the heading of the flight line in question.

$$\begin{aligned}
r_i^m(t) &= r_b^m(t) + \begin{bmatrix} \cos(\kappa(t)) & -\sin(\kappa(t)) & 0 \\ \sin(\kappa(t)) & \cos(\kappa(t)) & 0 \\ 0 & 0 & 1 \end{bmatrix} \begin{bmatrix} \Delta x \\ \Delta y \\ \Delta z \end{bmatrix} \\
&+ \begin{bmatrix} \cos(\kappa(t)) & -\sin(\kappa(t)) & 0 \\ \sin(\kappa(t)) & \cos(\kappa(t)) & 0 \\ 0 & 0 & 1 \end{bmatrix} \begin{bmatrix} 1 & -\Delta\kappa & \Delta\varphi \\ \Delta\kappa & 1 & -\Delta\omega \\ -\Delta\varphi & \Delta\omega & 1 \end{bmatrix} \begin{bmatrix} x(t) \\ 0 \\ z(t) \end{bmatrix}
\end{aligned} \tag{3.2}$$

The symbolic representation of eq. (3.2) is eq. (3.3), where the true system parameters are represented as \mathbf{x} , the noise-free measurements are represented as \mathbf{y}_{nf} , and the time tag of the point in question as \mathbf{t} . The biased point cloud coordinates $\mathbf{r}_i^m(\mathbf{t}, \mathbf{biased})$ are shown in eq. (3.4), where the random error associated with the measurements is \mathbf{e} and the term $\delta\mathbf{x}_b$ represents the biases contaminating the system parameters. To start the process of forming the calibration math model, eq. (3.4) could be expanded to the form in eq. (3.5) using Taylor series expansion. In eq. (3.5), the term $\mathbf{f}(\mathbf{x}, \mathbf{y}_{nf}, \mathbf{t})$, represents the true coordinates of the point in question $\mathbf{r}_i^m(\mathbf{t})$, and the terms \mathbf{J}_x and \mathbf{J}_y represent the Jacobian matrices with respect to the system parameters and measurements, respectively. Eq. (3.5) is reformulated into eq. (3.6) by expressing the true coordinates in terms of the biased coordinates. Now, the discrepancy equations can be formed under the presumption that conjugate points (one from point cloud \mathbf{A} and one from point cloud \mathbf{B}) should have identical coordinates. This relationship is seen in eq. (3.7), and it is then reformulated into eq. (3.8) so that the known and unknown values are on opposite sides of the equation. It is stated in eq. (3.8) that the combined error term from this discrepancy equation is $(\mathbf{J}_{y_A}\mathbf{e}_A - \mathbf{J}_{y_B}\mathbf{e}_B)$, and it is distributed with a mean of zero and variance-covariance matrix of $(\mathbf{J}_{y_A}\Sigma_A\mathbf{J}_{y_A}^T + \mathbf{J}_{y_B}\Sigma_B\mathbf{J}_{y_B}^T)$. When control is incorporated, the discrepancy equation to use is eq. (3.9). Instead of

comparing a biased point from point cloud \mathbf{A} to one in point cloud \mathbf{B} , eq. (3.9) compares a biased point from \mathbf{A} to the control point $\mathbf{r}_{I_{C_0}}^m$. The noise contaminating the control point is represented as \mathbf{e}_C , and its variance-covariance matrix is represented as Σ_C . In eq. (3.9), the uncertainty of the combined error term in the discrepancy equation is $(\mathbf{J}_{y_A}\mathbf{e}_A - \mathbf{e}_C)$, and it is distributed with a mean of zero and a variance-covariance matrix of $(\mathbf{J}_{y_A}\Sigma_A\mathbf{J}_{y_A}^T + \Sigma_C)$.

$$r_1^m(t) = f(x, y_{nf}, t) \quad (3.3)$$

$$r_i^m(t, \text{biased}) = f(x + \delta x_b, y_{nf} + e, t) \quad (3.4)$$

$$\begin{aligned} r_i^m(t, \text{biased}) &\approx f(x, y_{nf}, t) + J_x \delta x_b + J_y e \\ &\approx r_i^m(t) + J_x \delta x_b + J_y e \end{aligned} \quad (3.5)$$

$$r_i^m(t) = r_i^m(t, \text{biased}) - J_x \delta x_b - J_y e \quad (3.6)$$

$$\begin{aligned} r_{I_A}^m(t_A) - r_{I_B}^m(t_B) &= (r_{I_A}^m(t_A, \text{biased}) - J_{x_A} \delta x_b - J_{y_A} e_A) \\ &\quad - (r_{I_B}^m(t_B, \text{biased}) - J_{x_B} \delta x_b - J_{y_B} e_B) = 0 \end{aligned} \quad (3.7)$$

$$\begin{aligned} r_{I_A}^m(t_A, \text{biased}) - r_{I_B}^m(t_B, \text{biased}) &= (J_{x_A} \delta x_b + J_{y_A} e_A) - (J_{x_B} \delta x_b + J_{y_B} e_B) \\ &\quad \&(J_{y_A} e_A - J_{y_B} e_B) \sim (0, J_{y_A} \Sigma_A J_{y_A}^T + J_{y_B} \Sigma_B J_{y_B}^T) \end{aligned} \quad (3.8)$$

$$\begin{aligned} r_{I_A}^m(t_A, \text{biased}) - r_{I_{C_0}}^m &= (J_{x_A} \delta x_b + J_{y_A} e_A) - e_C \\ &\quad \&(J_{y_A} e_A - e_C) \sim (0, J_{y_A} \Sigma_A J_{y_A}^T + \Sigma_C) \end{aligned} \quad (3.9)$$

The discrepancy equations can then be evaluated using the biased point cloud coordinates and the Jacobian matrices J_{x_A} and J_{x_B} (J_{y_A} and J_{y_B} are used in the error propagation). The terms $J_x \delta \mathbf{x}_b$, J_y , and \mathbf{e} are shown in eq. (3.10), eq. (3.11), and eq. (3.12) respectively, and the Jacobian terms can be evaluated after synthesizing the missing raw measurements ($\mathbf{r}_b^m(t)$, $\mathbf{R}_b^m(t)$, and $\mathbf{r}_l^{lu}(t)$).

$$\begin{aligned}
& J_x \delta \mathbf{x}_b_{3 \times 7} \\
&= \begin{bmatrix} \cos(\kappa(t)) \delta \Delta X - \sin(\kappa(t)) \delta \Delta Y \\ \sin(\kappa(t)) \delta \Delta X + \cos(\kappa(t)) \delta \Delta Y \\ \delta \Delta Z \end{bmatrix} \\
&+ \begin{bmatrix} \sin(\kappa(t)) z(t) \delta \Delta \omega + \cos(\kappa(t)) z(t) \delta \Delta \varphi - \sin(\kappa(t)) x(t) \delta \Delta \kappa \\ -\cos(\kappa(t)) z(t) \delta \Delta \omega + \sin(\kappa(t)) z(t) \delta \Delta \varphi + \cos(\kappa(t)) x(t) \delta \Delta \kappa \\ -x(t) \delta \Delta \varphi \end{bmatrix} \quad (3.10) \\
&+ \begin{bmatrix} -\cos(\kappa(t)) \sin(S\beta(t)) \delta \Delta \rho + \cos(\kappa(t)) z(t) \beta(t) \delta S \\ -\sin(\kappa(t)) \sin(S\beta(t)) \delta \Delta \rho + \sin(\kappa(t)) z(t) \beta(t) \delta S \\ -\cos(S\beta(t)) \delta \Delta \rho - x(t) \beta(t) \delta S \end{bmatrix}
\end{aligned}$$

$$\begin{aligned}
& J_y_{3 \times 6} \\
&= \begin{bmatrix} 1 & 0 & 0 & a & -\cos(\kappa(t)) \sin(S\beta(t)) & \cos(\kappa(t)) z(t) S \\ 0 & 1 & 0 & b & -\sin(\kappa(t)) \sin(S\beta(t)) & \sin(\kappa(t)) z(t) S \\ 0 & 0 & 1 & 0 & -\cos(S\beta(t)) & -x(t) S \end{bmatrix}, \text{ where} \\
&a = \cos(\kappa(t)) z(t) \delta \Delta \omega - \sin(\kappa(t)) z(t) \delta \Delta \varphi - \delta \Delta Y \cos(\kappa(t)) \\
&\quad - \delta \Delta X \sin(\kappa(t)) - \sin(\kappa(t)) x(t) - \cos(\kappa(t)) x(t) \delta \Delta \kappa, \\
&b = \cos(\kappa(t)) z(t) \delta \Delta \varphi + \sin(\kappa(t)) z(t) \delta \Delta \omega + \delta \Delta X \cos(\kappa(t)) \\
&\quad - \delta \Delta Y \sin(\kappa(t)) + \cos(\kappa(t)) x(t) - \sin(\kappa(t)) x(t) \delta \Delta \kappa
\end{aligned} \quad (3.11)$$

$$e_{6 \times 1} = \begin{bmatrix} e_{X_L} \\ e_{Y_L} \\ e_{Z_L} \\ e_{\kappa} \\ e_{\rho} \\ e \end{bmatrix} \quad (3.12)$$

3.2.2 Synthesizing Raw Measurements

To synthesize the raw measurements, first, a global heading for the entire flight line in question is determined by inspecting the Minimum Bounding Rectangle (MBR). The MBR is the rectangle with minimum area that encloses all the points within a given flight (Freeman and Shapira, 1975; Kwak and Habib, 2013), and can be seen in Figure 3.1. The outputs from the MBR generation are coordinates of the resulting rectangle's four corners. Then, the trajectory heading and other raw measurements are synthesized according to the following steps: **1)** As illustrated in Figure 3.1, the scan pattern of a point cloud will be in a zigzag pattern with scan lines that are almost parallel with two sides of the MBR. The midpoints of those two sides are the starting and ending points of the vector representing the flight direction (from the sequence of points, one can infer which midpoint is the starting point). These points reveal the heading of the trajectory κ and with that, the term $R_b^m(\mathbf{t})$ can be evaluated according to eq. (3.13). **2)** The synthesized flight trajectory is found by raising the flight direction vector up to the flying height. **3)** The trajectory position for the point in question $\mathbf{r}_b^m(\mathbf{t})$ is the result of projecting the point onto the synthesized trajectory. **4)** As illustrated in Figure 3.2, the x -laser unit coordinate of a LiDAR point $\mathbf{x}(\mathbf{t})$ is essentially the lateral distance, with the appropriate sign, between the LiDAR point in question and the flight direction. The z -laser unit coordinate of the LiDAR point with respect to the laser unit frame $\mathbf{z}(\mathbf{t})$ can be determined by subtracting the flying height above the datum from the LiDAR point elevation (i.e. $\mathbf{z}(\mathbf{t}) = -(\mathbf{H} - \mathbf{Z}(\mathbf{t}))$). The laser unit coordinates make up the term $\mathbf{r}_l^{lu}(\mathbf{t}) = [\mathbf{x}(\mathbf{t}) \quad \mathbf{0} \quad \mathbf{z}(\mathbf{t})]$, which can be used to evaluate the mirror scan angle $\beta(\mathbf{t})$ through basic trigonometric relationships. Following these steps for each strip will result in the raw measurements needed to carry out the calibration and estimate the system parameter biases.

$$R_b^m(\mathbf{t}) = \begin{bmatrix} \cos(\kappa(\mathbf{t})) & -\sin(\kappa(\mathbf{t})) & 0 \\ \sin(\kappa(\mathbf{t})) & \cos(\kappa(\mathbf{t})) & 0 \\ 0 & 0 & 1 \end{bmatrix} \quad (3.13)$$

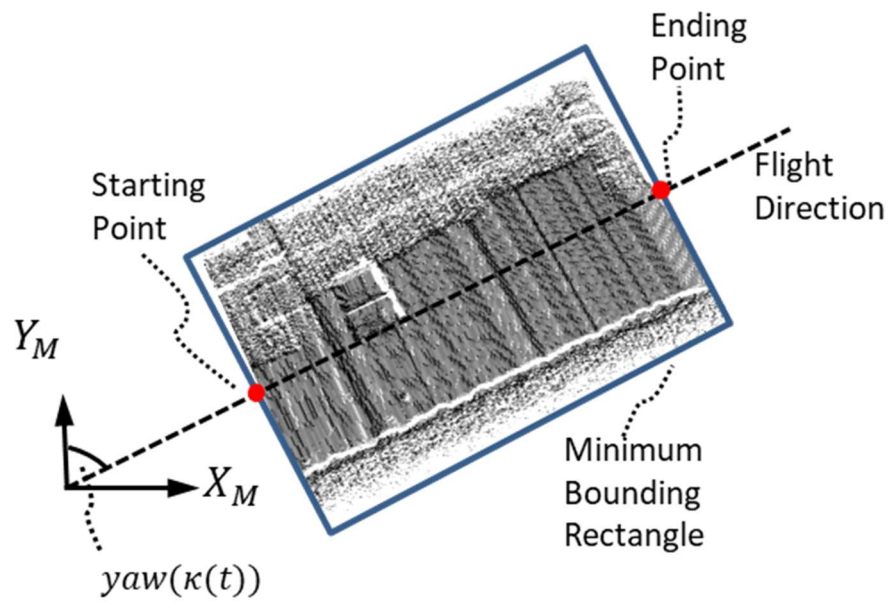


Figure 3.1: Minimum Bounding Rectangle Procedure for Determining Flight Direction

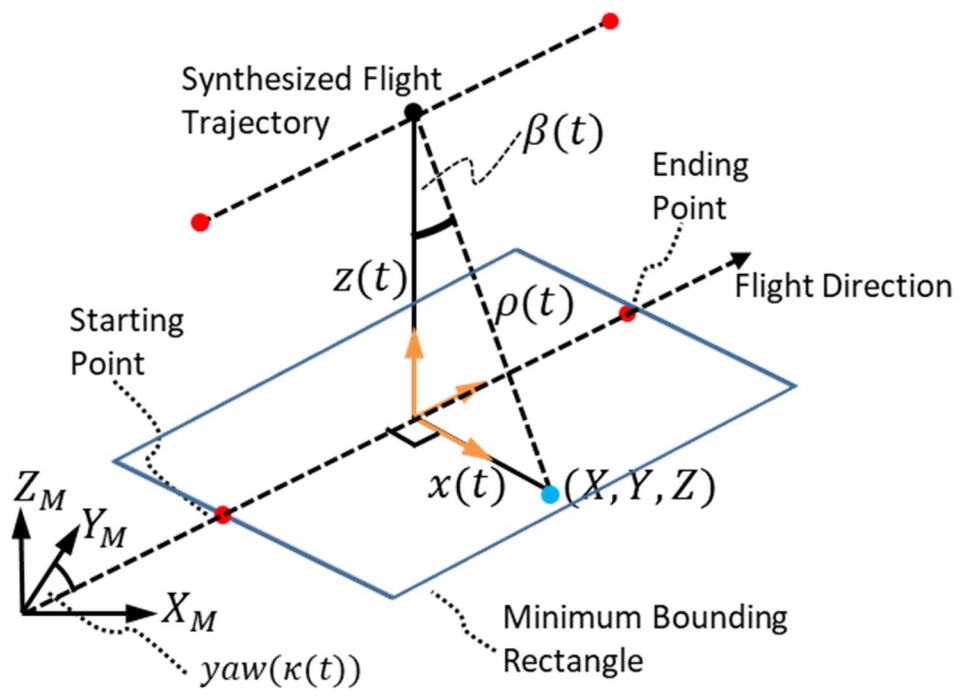


Figure 3.2: Synthesizing the System Raw Measurements for the **QRQS** Calibration Procedure

Upon synthesizing the raw measurements, the system parameter biases are estimated and the adjusted coordinates can be evaluated by removing the impact of the estimated system parameter biases $J_x \delta x_b$. Removing the impact completes the calibration process and this removal is shown in eq. (3.14), which is evaluated using the biased coordinates, the synthesized measurements, and the estimated system parameter biases.

$$r_i^m(t)_{(Adjusted)} = r_i^m(t)_{(Biased)} - J_x \delta x_b \quad (3.14)$$

3.2.3 Calibration Strategy

The calibration strategy involves an iterative process of matching (with ICPatch) and solving for the system parameter biases (depicted in Figure 3.3). The process starts with strip *A* and strip *B* as input data, and then a TIN is formed with strip *A*. Next, the measurements that are needed for the discrepancy equations are synthesized. Before estimating the system parameters using the discrepancy equations (3.8) and (3.9), the closest point-patch pairs are determined, either from initial approximations on the first iteration, or from the adjusted point clouds which resulted from the previous iteration. After the first iteration, the adjusted point clouds are used for the matching procedure in case the matches change after adjusting the point cloud. It is important to note that the matches, which are calculated after adjusting the coordinates, are used in the parameter estimation step, but the original biased coordinate values are always used (as opposed to using the updated coordinate values). When the iteration process converges, the final adjusted coordinates are determined by removing the impact of the biases using eq. (3.14), and the calibration is complete.

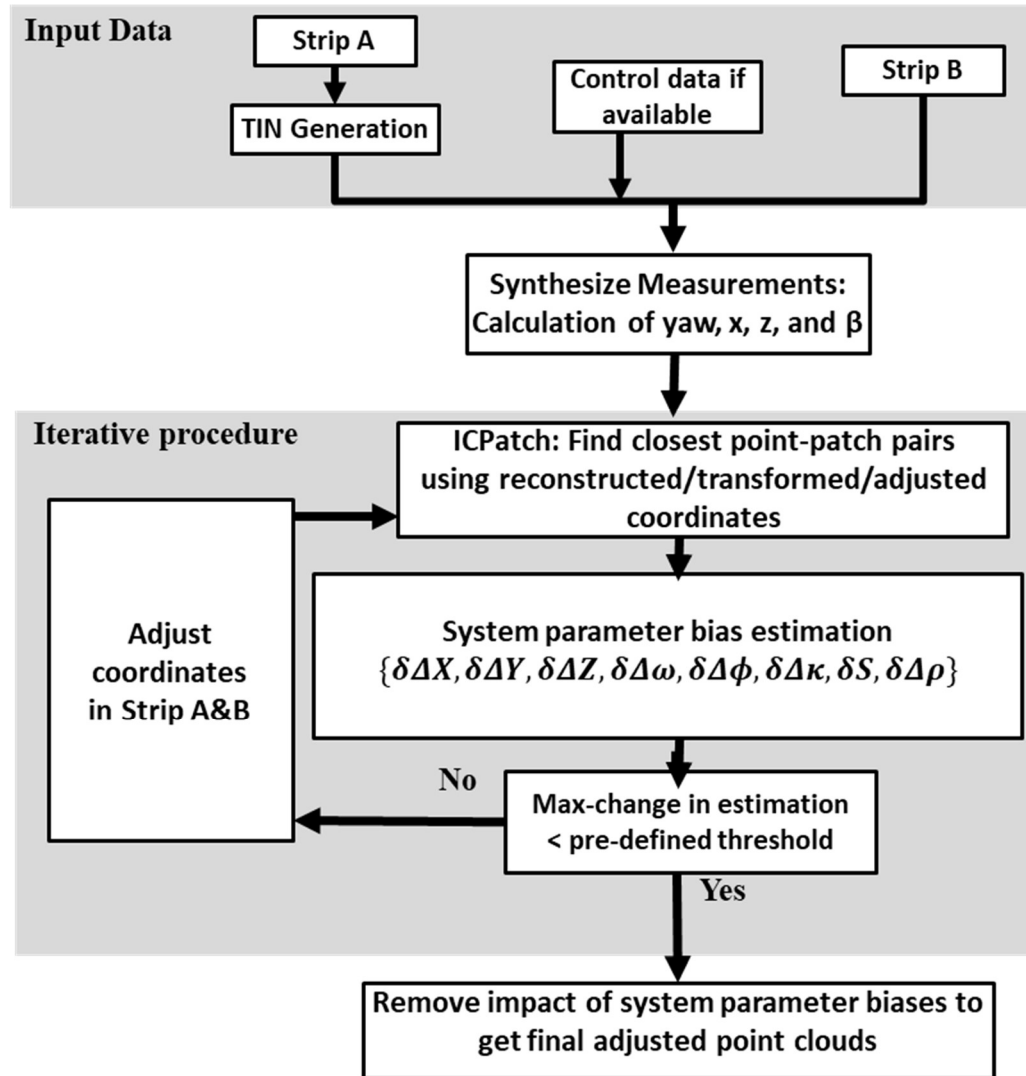


Figure 3.3: Workflow of the *QRQS* Calibration Procedure

3.3 LiDAR System Calibration Stability Analysis

Reliable and accurate recovery of LiDAR system parameters through calibration is what allows LiDAR technology to be as accurate as possible. LiDAR calibration is well understood, but the process of analyzing the stability of the system parameters over time has not been established. This research will give a quantitative strategy for stability analysis by comparing outcomes from calibration results derived at separate times. An overview of the stability analysis for LiDAR calibration is discussed; then the strategy for carrying out the stability analysis is reviewed.

3.3.1 Stability Analysis Overview

The **R** calibration reconstructs the point cloud after estimating the system parameters shown in eq. (3.15) (when dealing with a linear scanner S_α is not included), and the *Pseudo-rigorous* calibration methods (**S**, **QR**, and **QRQS**) adjust the point cloud after estimating the system parameter biases shown in eq. (3.16). The stability analysis process for both the **R** and *Pseudo-rigorous* approaches reconstructs/adjusts a LiDAR point cloud using temporally different calibration results, and it analyzes the observed spatial offsets between them. To quantify the stability, an RMSE measure is used to determine if there is a significant difference between the coordinates reconstructed/adjusted with the two different calibration results. The stability analysis measure for the **R** and *Pseudo-rigorous* approaches is the same, but the stability analysis strategy for *Pseudo-rigorous* approaches requires additional steps to synthesize the missing raw measurements.

$$\delta x = \begin{bmatrix} \Delta X \\ \Delta Y \\ \Delta Z \\ \Delta \omega \\ \Delta \phi \\ \Delta \kappa \\ \Delta \rho \\ S_\alpha \\ S \end{bmatrix} \quad (3.15)$$

$$\delta x_b = \begin{bmatrix} \delta \Delta X \\ \delta \Delta Y \\ \delta \Delta Z \\ \delta \Delta \omega \\ \delta \Delta \phi \\ \delta \Delta \kappa \\ \delta \Delta \rho \\ \delta S \end{bmatrix} \quad (3.16)$$

3.3.2 Stability Analysis Strategy

The strategy for the stability analyses for the *R* calibration approach and the *Pseudo-rigorous* calibration approach are illustrated in Figure 3.4 and Figure 3.5, respectively. For each of the stability analysis procedures, the quantitative measure is the degree of similarity between a point cloud which is reconstructed/adjusted from a set of calibration parameters derived at time T_1 , and the same point cloud reconstructed/adjusted from a set of calibration parameters derived at time T_2 . The point clouds are from the same exact collection flight, the only difference is the set of system parameters used to reconstruct/adjust them.

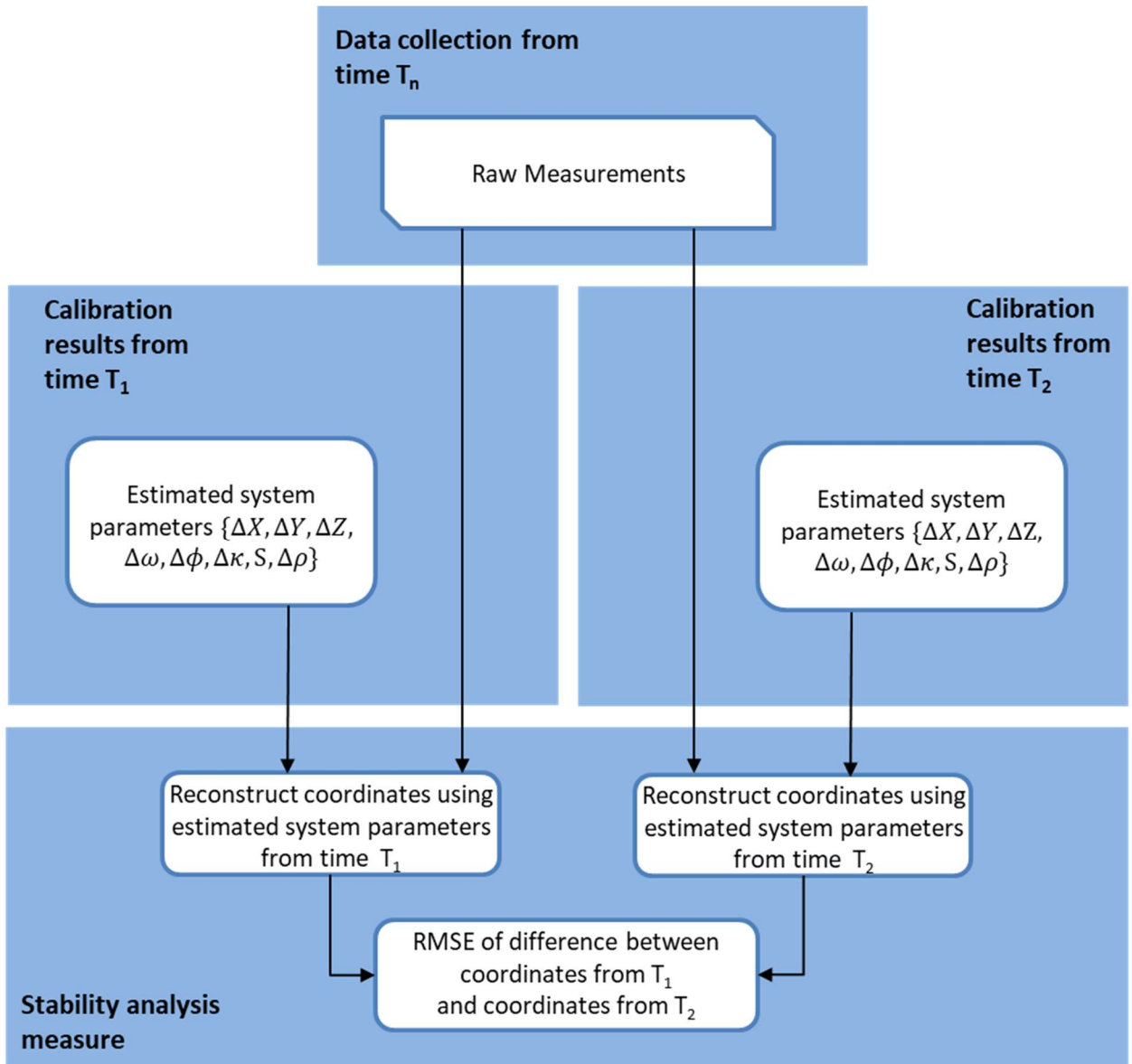


Figure 3.4: Workflow of the Stability Analysis Procedure for the R Calibration Approach

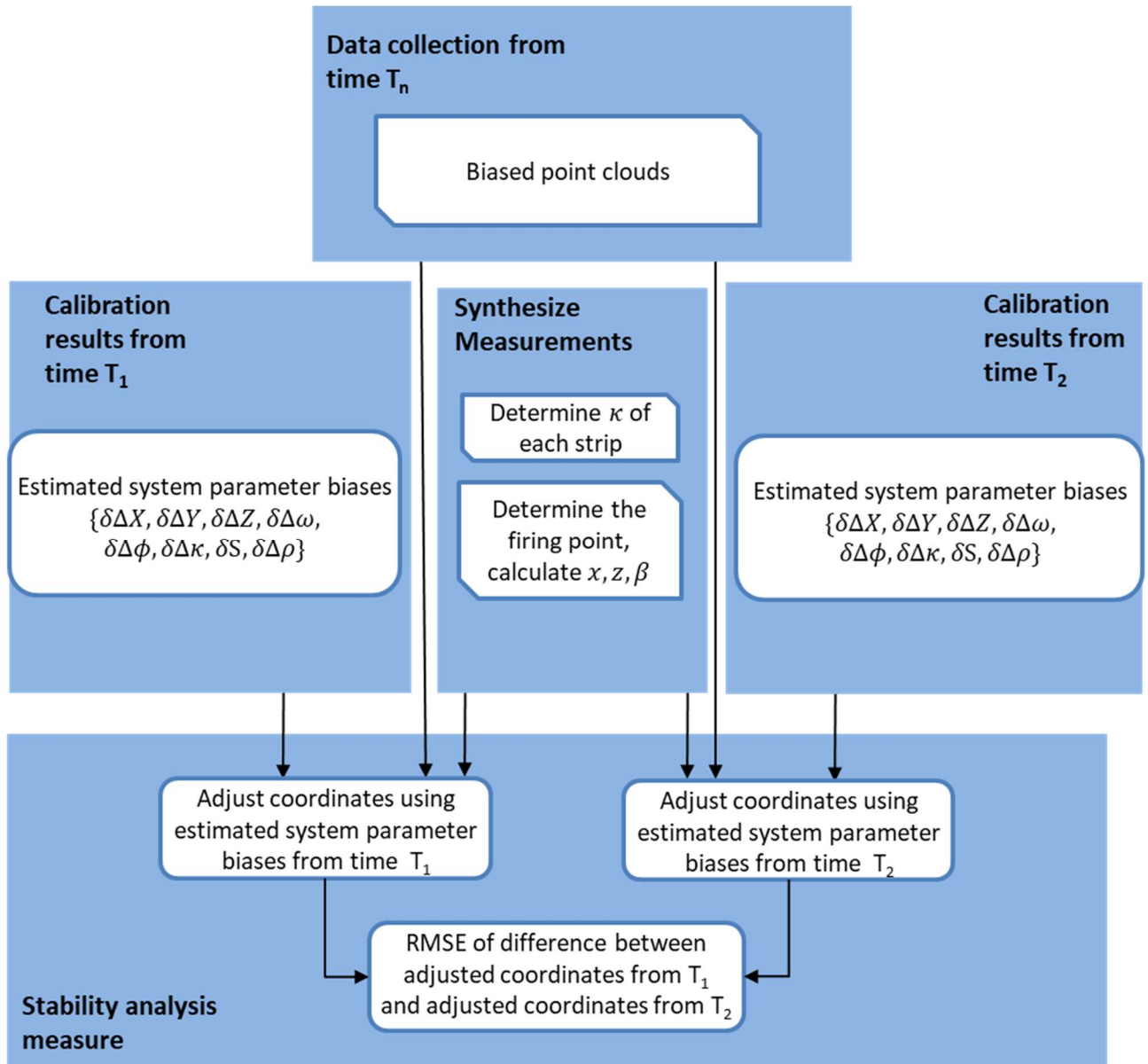


Figure 3.5: Workflow of the Stability Analysis Strategy for the *Pseudo-rigorous* Calibration Approaches

For the R stability analysis, the reconstruction is done using the LiDAR point-positioning equation (3.17). For the *Pseudo-rigorous* stability analysis, the adjusted coordinates are found by removing the impact of the biases as shown in eq. (3.18). The impact of the biases for the S approach is shown in eq. (3.19). The impact of the biases for the QR and the $QRQS$ approaches is shown in eq. (3.20).

$$r_I^m(t) = r_b^m(t) + R_b^m(t)r_{lu}^b + R_b^m(t)R_{lu}^b R_{lb}^{lu}(t)r_I^{lb}(t) \quad (3.17)$$

$$r_I^m(t)_{(Adjusted)} = r_I^m_{(Biased)} - J_x \delta x_b \quad (3.18)$$

$$J_x \delta x_b = \begin{bmatrix} \pm \delta \Delta X \mp H \delta \Delta \varphi \mp \sin(S\beta) \delta \Delta \rho \mp H \beta \delta S \\ \pm \delta \Delta Y \mp H \delta \Delta \omega \pm \delta \Delta \kappa \\ \delta \Delta Z - x \delta \Delta \varphi - \cos(S\beta) \delta \Delta \rho - x \beta \delta S \end{bmatrix} \quad (3.19)$$

$$\begin{aligned} & J_x \delta x_b_{QR,QRQS} \\ &= \begin{bmatrix} \cos(\kappa(t)) \delta \Delta X - \sin(\kappa(t)) \delta \Delta Y \\ \sin(\kappa(t)) \delta \Delta X + \cos(\kappa(t)) \delta \Delta Y \\ \delta \Delta Z \end{bmatrix} \\ &+ \begin{bmatrix} \sin(\kappa(t)) z(t) \delta \Delta \omega + \cos(\kappa(t)) z(t) \delta \Delta \varphi - \sin(\kappa(t)) x(t) \delta \Delta \kappa \\ -\cos(\kappa(t)) z(t) \delta \Delta \omega + \sin(\kappa(t)) z(t) \delta \Delta \varphi + \cos(\kappa(t)) x(t) \delta \Delta \kappa \\ -x(t) \delta \Delta \varphi \end{bmatrix} \quad (3.20) \\ &+ \begin{bmatrix} -\cos(\kappa(t)) \sin(S\beta(t)) \delta \Delta \rho + \cos(\kappa(t)) z(t) \beta(t) \delta S \\ -\sin(\kappa(t)) \sin(S\beta(t)) \delta \Delta \rho + \sin(\kappa(t)) z(t) \beta(t) \delta S \\ -\cos(S\beta(t)) \delta \Delta \rho - x(t) \beta(t) \delta S \end{bmatrix} \end{aligned}$$

In order to determine the degree of similarity between the point clouds that have been reconstructed/adjusted with calibration parameters derived at two separate times, an RMSE analysis will be used on the difference between the resulting reconstructed/adjusted coordinates. Using the reconstructed/adjusted coordinates from T_1 and T_2 , the RMSE of their difference is calculated using eq. (3.21) and compared to the expected noise. The expected noise is determined through a rigorous error propagation that accounts for all the uncertainty values associated with each individual raw measurement coming from the GNSS, INS, and laser unit. If the RMSE values are within the expected noise of the point cloud, then the point clouds are deemed similar. In this case, the change in system parameters over time are not considered to be significantly different and therefore stable

over the specified time period. If the RMSE values are not within the expected noise level of the data, then the system is considered to be unstable over the specific period of time.

$$RMSE(T_1, T_2) = \sqrt{\sum \frac{(r_i^m(T_1) - r_i^m(T_2))^2}{n}} \quad (3.21)$$

4. RESULTS OF THE QUASI-RIGOROUS/QUASI-SIMPLIFIED (QRQS) CALIBRATION AND STABILITY ANALYSIS

4.1 Overview

The results shown in this chapter focus on the implementation of the new *QRQS* calibration approach. First, section 4.2 shows the performance of the new method compared to existing methods, using data from a low altitude Unmanned Aerial Vehicle (UAV) platform. Then, section 4.3 uses simulated data at a higher altitude to test the new approach (and the existing *Pseudo-rigorous* approaches) in non-ideal scenarios to quantify their accuracy improvement ratios in conditions that do not meet their underlying assumptions. Section 4.4 uses the same data as section 4.3 to demonstrate the implementation of the stability analysis strategy.

4.2 Results of the Quasi-Rigorous/Quasi-Simplified (*QRQS*) Calibration using a UAV based LiDAR System

The *QRQS* calibration method has been developed to address the absence of raw measurements in LiDAR system calibration. This method carries out calibration with only the point cloud coordinates by using the previously discussed strategies to synthesize the missing raw measurements, and it does so while maintaining the rigor of calibration by preserving the sensor model. The following results show the implementation of the *QRQS* calibration method using data from a UAV platform specifically designed for cost effective low altitude metric mapping.

4.2.1 Platform and Sensors

The platform and sensors used to collect the data can be seen in Figure 4.1, which shows a VLP-16 PUCK Hi-Res LiDAR unit and an Applanix APX-15 UAV navigation board mounted on a DJI M600 UAV. The VLP-16 PUCK Hi-Res LiDAR unit has 16 laser beams oriented in fixed positions within the $x_{lw} - y_{lw}$ plane. Collectively, the beams were scanning at a rate of 300kHz (pulses/second) and spinning 360° at a rate of 10Hz

(cycles/second) during the data collection (although the LiDAR is spinning 360°, only points between -30° and 30° of nadir were reconstructed to focus on the ground). In Figure 4.1, the original laser unit (\mathbf{lu}) and IMU body frame (\mathbf{b}) coordinate systems are shown, and because they do not follow the expectations in the *Pseudo-rigorous* methods (i.e. the IMU body frame is not parallel to the laser unit coordinate system), virtual coordinate systems are implemented. The virtual IMU body frame (\mathbf{b}') and virtual laser unit (\mathbf{lu}') coordinate systems shown in Figure 4.1 were incorporated into the point-positioning equation according to eq. (4.1).

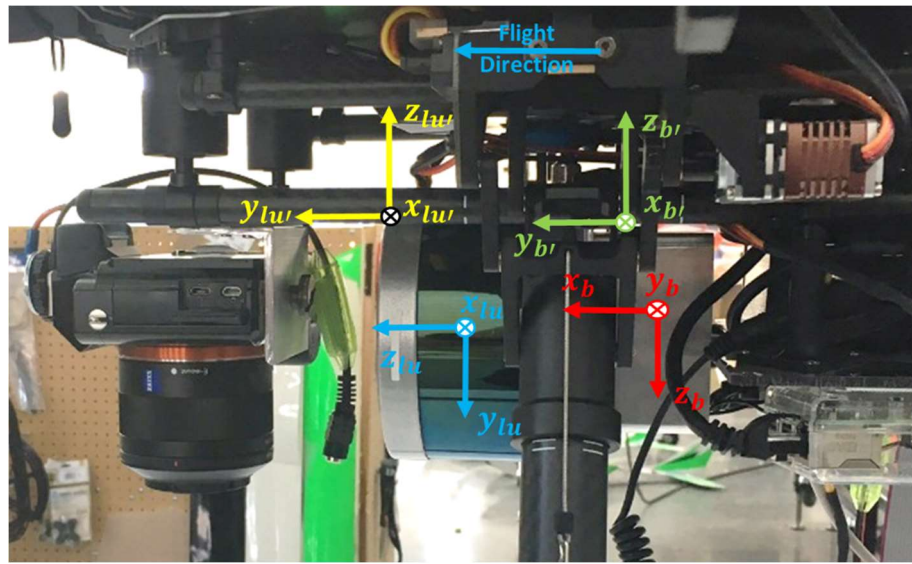


Figure 4.1: Alignment of Original and Virtual Coordinate Systems on the UAV LiDAR System used in this Analysis

$$\begin{aligned}
 r_I^m(t) = & r_b^m(t) + R_b^m(t)R_{b'}^b r_{lu'}^{b'} \\
 & + R_b^m(t)R_{b'}^b R_{lu'}^{b'} R_{lb}^{lu'} r_I^{lb}(t)
 \end{aligned} \tag{4.1}$$

The data used for this analysis is shown in Figure 4.2. There were six strip-pairs collected at 15m and 25m flying heights over a field with five geometric targets shaped like huts (as well as various checkerboards and reflective stop signs). Two of the huts were oriented so that the ridges were aligned along the North (N) and South (S) directions (along flight

directions), and the ridges of the other three huts were aligned in the East (E) and West (W) directions (across flight directions). These huts were used to provide the height variation needed in the otherwise flat terrain (elevation variation of terrain with huts: 1.0m, without huts: 0.2m). Three of the six strip-pairs were used for calibration to satisfy the optimal and minimal data requirement, the first and second strip-pairs contain two overlapping strips flying in opposite directions, at a flying height of 15m and 25m above ground, and with 100% overlap. The third strip-pair contained two flight strips flying in the same direction, at a flying height of 15m above ground, and 12m lateral distance between them. As is the case when flying UAVs, it is natural to have variation in the pitch and roll of the platform. For the *forward* flight lines, the pitch and roll variation ranges were $-2.2^\circ:0.5^\circ$ and $0.01^\circ:1.6^\circ$, respectively. For the *backward* flight lines, the pitch and roll variation ranges were $0.4^\circ:4.1^\circ$ and $-2.4^\circ:0.0^\circ$, respectively. The uncertainty of each involved measurement/derived measurement within the airborne LiDAR system is shown in Table 4-1. In this table, the GNSS/INS uncertainties are based on the Applanix APX-15 UAV board specifications sheet (Trimble Applanix, 2016) and the range uncertainty is based on the VLP-16 PUCK Hi-Res specification sheet (Velodyne LiDAR, 2016). The mirror angle encoder uncertainty is set to a quarter of the reported angular resolution on the VLP-16 PUCK Hi-Res LiDAR unit specifications sheet. The standard deviation for a reconstructed point was determined to be 6cm in the X and Y coordinates and 4cm in the Z coordinate by rigorously propagating the uncertainty values from Table 4-1 to the ground using the LiDAR Error Propagation Calculator developed by Habib et al. (2006). In the calibration programs, the Σ matrix (previously shown in eq. (2.24)) diagonal values come from the uncertainty of each measurement shown in Table 4-1. As for the a-priori variance-covariance matrix of the estimated system parameters/system parameter biases Σ_x , their diagonal values were set to be very low if the parameters/biases were known (e.g. 1×10^{-9}), or they were set to be high values (e.g. 1×10^9) to allow the program to estimate the parameter/bias. These low and high values are used to set the parameter/bias as fixed or free, respectively, but the user can input any value which is appropriate for their scenario. For the Σ and Σ_x matrices in the experimental results of this dissertation, only the diagonal elements are filled, the full variance-covariance matrix is not formed. The ULEM approach (Rodarmel et al., 2015) mentioned in the literature review does model the correlations

rigorously using what is called the Strictly Positive Definite Correlation Function (SPDCF) discussed by Dolloff (2013). Employing the full variance-covariance matrix is used to fully exploit the data, and although the effects of not using it may be negligible when flying heights are low, it may not be valid for higher altitude scenarios.

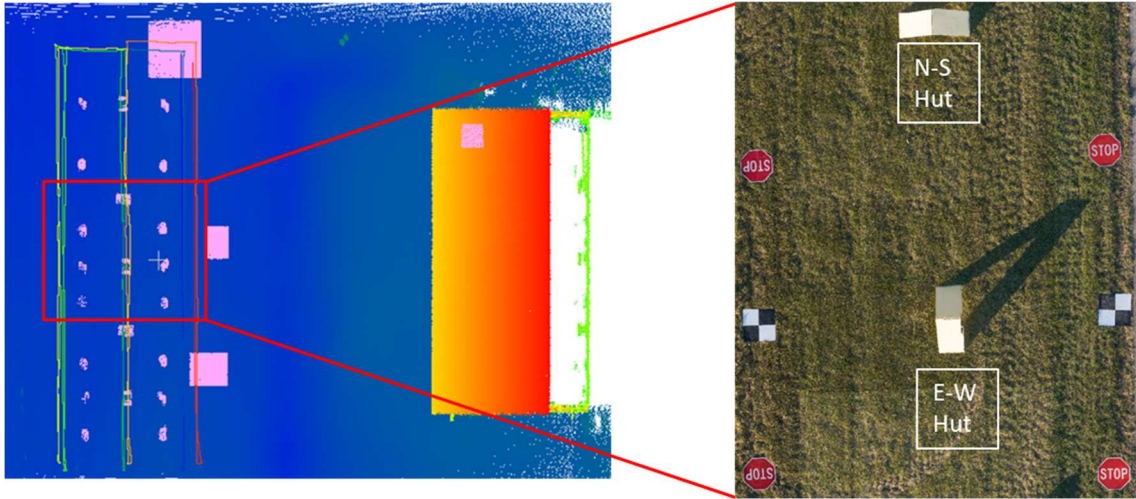


Figure 4.2: Flight Trajectories and Test Field Containing Geometric Targets (huts) as seen in 3D Point Clouds and Orthophoto

Table 4-1: Uncertainty of the LiDAR System Measurements

GNSS/INS position – X, Y, Z (m)	(0.03,0.03,0.03)
GNSS/INS orientation – ω, φ, κ (")	(72,72,360)
Mirror Angle Encoder (")	81
Range (m)	0.03

The *Pseudo-rigorous* calibration approaches were designed for single-beam linear laser scanners. This configuration allows the raw measurements to be synthesized through an inspection of the point cloud. When observing the resulting point cloud produced from a multi-beam and spinning laser scanner without any raw measurements (e.g. beam ID, recorded encoder angle, etc.), it is impossible to know which beam each point came from; therefore, it is impossible to synthesize the raw measurements. The orientation of the 16 laser beams within the VLP-16 PUCK Hi-Res are show in Figure 4.3. Using only the points

from one of the 16 beams (the one that is closest to vertical at $\sim 1^\circ$ from nadir, laser beam #2 or #15) produces a similar scanning pattern as a single-beam linear scanner, which allows the missing raw-measurements to be synthesized. It is important to note that the R approach is capable of calibrating a multi-beam spinning laser scanner system without isolating data from a single beam; however, it requires the system raw measurements.

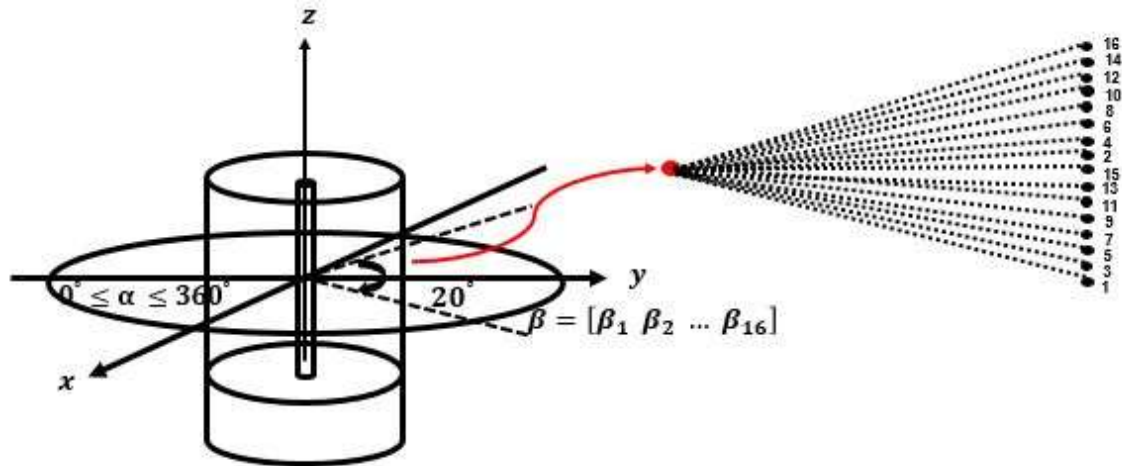


Figure 4.3: Orientation of VLP-16 PUCK Hi-Res Laser Beams

4.2.2 Calibration Results and their Quantitative and Qualitative Comparison with Existing Calibration Approaches

The R results discussed here include two different implementations, the *16-beam R* and the *1-beam R*. The *Pseudo-rigorous* approaches include the S , QR and $QRQS$. The *16-beam R* results were based on a feature based calibration which used all 16 beams (Ravi et al., 2018), and the *1-beam R*, S , QR , and $QRQS$ use the points from 1 laser beam over the entire terrain (no feature extraction). For the *16-beam R*, the checkerboard targets, building facades, hut-shaped targets, and the reflective stop signs were extracted from the point clouds shown in Figure 4.2. The *16-beam R* and *1-beam R* estimate the parameters and output the corrections ($\delta\Delta$) to the approximate values, while the S , QR , and $QRQS$ approaches estimate the biases ($\delta\Delta_b$). The biases can be distinguished from the corrections by the subscript b . The biases should be of the same magnitude as the corrections, but with the opposite sign. For this comparison, the results of all the approaches will be introduced and then the adjusted coordinates resulting from the *16-beam R* will be used as the

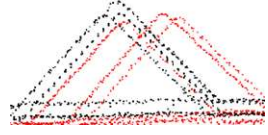
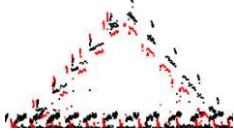





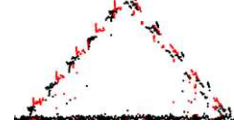
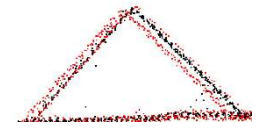

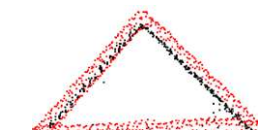

reference for evaluating the performance of the others (while focusing on the performance of the *QRQS Pseudo-rigorous* approach). The results of the calibration methods are shown in Table 4-2. The range bias is not estimated because there is not enough elevation variation in the across flight direction, and the scan angle scale factor bias is not estimated because the VLP-16 PUCK Hi-Res is a spinning LiDAR unit which does not have an oscillating mirror.

Table 4-2: Results for the *16-beam R*, *1-beam R*, *S*, *QR*, and *QRQS* Approaches using the VLP-16 PUCK Hi-Res LiDAR on a UAV Platform

	16-beam R	1-beam R		S	QR	QRQS
	Rigorous Estimated Corrections			Pseudo-rigorous Estimated Biases		
$\delta\Delta X$ (m):	0.02	0.01	$\delta\Delta X_b$ (m):	0.01	-0.03	-0.02
$\delta\Delta Y$ (m):	0.01	0.06	$\delta\Delta Y_b$ (m):	-0.02	-0.02	0.01
$\delta\Delta\omega$ (°):	0.04	-0.13	$\delta\Delta\omega_b$ (°):	-0.10	-0.08	-0.11
$\delta\Delta\phi$ (°):	-0.70	-0.86	$\delta\Delta\phi_b$ (°):	0.83	0.86	0.83
$\delta\Delta\kappa$ (°):	-0.33	-0.33	$\delta\Delta\kappa_b$ (°):	0.15	0.17	0.16
(biases should be of the same magnitude as the corrections, but with the opposite sign)						

For the qualitative comparison of the *QRQS* approach with the existing approaches, the alignment of overlapping strips before and after calibration can be seen in Table 4-3. This table shows a hut which was oriented so that the ridges were aligned along the North (N) and South (S) directions (along flight directions), and another hut that was oriented so that its ridges were aligned in East (E) and West (W) directions (across flight directions). The point clouds before calibration have an offset between the overlapping strips, while the overlapping point clouds after calibration show a significant improvement in alignment. Each of the approaches was successful in reducing the impact of systematic errors on the resulting point clouds, and the *16-beam R* and *1-beam R* approaches show the best alignment as expected. When comparing the alignment of *QRQS* with *S*, it is observed that the alignment in the vertical direction is better for the *QRQS*. When comparing the alignment of *QRQS* with *QR*, it is observed that they are very similar. This outcome is expected because the development of the *QRQS* math model is significantly different from that of the *S*, but very similar to that of the *QR*.

Table 4-3: Qualitative Analysis of Point Cloud Coordinates on the North-South (N-S) and East-West (E-W) Huts Before Calibration and After Calibration for the *16-beam R*, *1-beam R*, *S*, *QR*, and *QRQS* Approaches

	N-S Hut	E-W Hut
Before Cal.		
After Cal. (<i>16-beam R</i>)		
After Cal. (<i>1-beam R</i>)		
After Cal. (<i>QRQS</i>)		
After Cal. (<i>QR</i>)		
After Cal. (<i>S</i>)		
Red = forward flight, Black = backward flight		

The quantitative assessment of the *QRQS* approach and the existing approaches inspects the adjusted/reconstructed coordinates to see if there is a significant difference between

them and the reconstructed coordinates from the *16-beam R* approach. Table 4-4 shows the Root-Mean-Squared Error (RMSE) of the differences between the adjusted/reconstructed coordinates from the *16-beam R* approach and the *S*, *QR*, *QRQS*, and *1-beam R* approaches. The *Total Statistics* row shows the mean and standard deviation (st. dev) of the *X*, *Y*, and *Z* coordinate differences. In Table 4-4, the RMSE values range from 0cm to 6cm, and the highest values are observed in the *Z* and *Y* adjusted coordinates from the *S* and *QRQS* approaches, respectively. This 6cm RMSE in the *Z* adjusted coordinates of the *S* approach is higher than 4cm error propagation results for the *Z* coordinate. This 6cm RMSE in the *Y* adjusted coordinates of the *QRQS* approach is of the same magnitude as the 6cm error propagation results for the *Y* coordinate and is therefore not deemed significant. The mean and standard deviation values show the spread of the differences, and the low mean values signify that the presence of systematic errors is low. Although the huts in Table 4-4 show signs of remaining systematic errors, they are only detected in the RMSE analysis of the *Z* adjusted coordinates of the *S* approach. Therefore, the adjusted/reconstructed coordinates from the *QR*, *QRQS*, and *1-beam R* are not considered to be significantly different from the reconstructed coordinates of the *16-beam R* approach. Since the *QRQS* approach (like the *S* and *QR* existing *Pseudo-rigorous* approaches) makes several assumptions, it is not guaranteed to fully remove the presence of systematic errors, but it is successful in significantly reducing them. This analysis has shown that the *QRQS* approach is suitable for calibration in the full absence of raw measurements, while the *S* approach still has a significant amount of systematic error in the *Z* coordinate after calibration. The next analysis will demonstrate the limitations of the *S* approach and capabilities of the *QRQS* approach by analyzing their performance after deviating from their math model assumptions.

Table 4-4: RMSE of the Difference between Adjusted/Reconstructed Coordinates from each Calibration Approach and the Reconstructed Coordinates from the *16-beam R*

		S	QR	QRQS	1- beam R	
RMSE Per Coord.	X(m)	0.01	0.05	0.04	0.03	
	Y(m)	0.01	0.02	0.06	0.02	
	Z(m)	0.06	0.00	0.02	0.00	
Total Stats. Per Coord.	X(m)	mean	0.00	0.01	0.01	0.01
		st.dev	0.01	0.04	0.04	0.03
	Y(m)	mean	0.00	0.00	0.01	0.00
		st.dev	0.01	0.02	0.05	0.02
	Z(m)	mean	0.01	0.00	0.00	0.00
		st.dev	0.05	0.00	0.02	0.00

4.3 Performance of the Quasi-Rigorous/Quasi-Simplified (*QRQS*) Approach and Existing Calibration Approaches Before and After Deviating from their Assumptions

In order to highlight the differences between the *QRQS* approach and the other *Pseudo-rigorous* approaches, as well as quantify how robust they perform in non-ideal scenarios, this analysis will compare the results before and after calibration for scenarios that were both deviated from the respective assumptions and non-deviated. This analysis uses simulated data and characterizes how well the calibration approaches hold up in data collection scenarios that do not strictly adhere to the assumptions their math models are based on. In doing so, the results also reveal the limitations of the *S* calibration approach when compared to the new *QRQS* approach.

4.3.1 Rigorous Data Simulation

The point clouds used in this analysis were generated by simulating flights using ray tracing techniques over a predefined DEM from the USGS. The DEM used is of natural terrain that does not have any man-made objects such as buildings with gable roofs. The terrain elevation of the DEM was scaled down from a 400m elevation variation to a 100m variation in order to test the \mathcal{S} calibration assumption of low elevation variation with respect to the 2000m flying height. Simulating the data provided a very reliable way to investigate the impact of individual deviations. The simulation process actually mimics the rigorous mathematical model of the LiDAR system with ray tracing techniques, and it accounts for LiDAR unit specifications and all hardware uncertainties (i.e. GNSS/INS, range measurement, and scan angle). An example of two simulated flight lines and the resulting point clouds is shown in Figure 4.4 (the headings of the flight lines in this simulation differ by 30°).

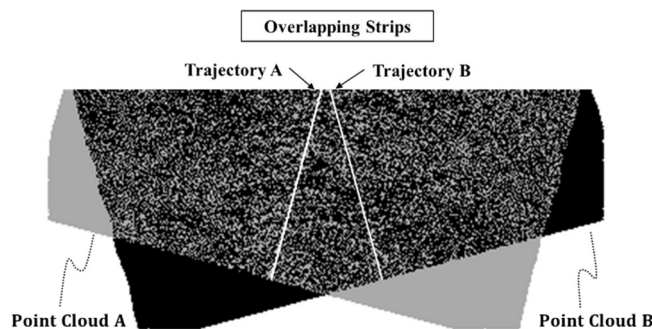


Figure 4.4: Simulated Point Clouds and Trajectories Deviated from Being Parallel by 30° (planimetric view)

For the simulation, the user defines the LiDAR unit specifications and the uncertainty of each measurement within the system. The pulse repetition rate was set at 33.3 kHz, the scan rate was set at 40 scans/sec, and the laser scan angle at 30° . The uncertainty values in Table 4-5 were used to generate random noise for each linear and angular measurement per pulse. These values reflect the uncertainty levels of high altitude industrial grade aerial LiDAR mapping systems. The configuration of the strip-pairs is show in Table 4-6.

Table 4-5: Uncertainty of the LiDAR System Components for Simulated Data

GNSS/INS Position - X, Y, Z (m)	0.05, 0.05, 0.10
GNSS/INS Orientation - ω, φ, κ (")	9, 9, 18
Mirror Angle Encoder (")	3
Range (m)	0.02

Table 4-6: Configuration of Strip-pairs for Simulated Data

Strip-pair	Flying Height (m)	Lateral Distance Between Trajectories (m)
1	1000	0
2	2000	0
3	2000	500

Throughout this analysis, there will be three sets of coordinates used; namely, true, biased, and adjusted coordinates. The true and biased coordinates were outputs from the simulator, and the adjusted coordinates were determined after calibration. The biased coordinates were contaminated with noise and system parameter biases, as is the case in a real-world scenario. The true coordinates have no noise and no system parameter biases. The adjusted coordinates were the result of adjusting the biased coordinates using the estimated system parameter biases.

Control was not used in the tests on assumption deviations in order to show how well the calibration approaches perform using non-urban terrain that has no control available. The last set of results demonstrate the ability of the R , QR , and $QRQS$ approaches to incorporate control. For the test on assumption deviations, the lever arm bias in the Z direction, $\delta\Delta z_b$, was not estimated because it requires vertical control. The range bias, $\delta\Delta\rho_b$, was not estimated in some of the results because, as mentioned before, in order to estimate the range bias without control a high amount of elevation variation is required in the across flight direction.

Only the assumptions required for successful calibration were included in this analysis. Thus, if an assumption is not included, this implies that the LiDAR data can always be mathematically manipulated in order to meet that assumption. For example, the *IMU* body frame and the laser unit coordinate system are assumed to be almost parallel and when they are not, virtual coordinate systems can be introduced. Since the virtual coordinate systems meet the assumptions, any measurements should be modified so they are with respect to the virtual coordinate systems. Then, the calibration can be carried out as it normally would be. There is a section for each assumption deviation with the resulting estimated biases and the RMSE of the difference between the adjusted coordinates and true coordinates. The RMSE is shown for before and after calibration, denoted as $RMSE_{before}$ and $RMSE_{after}$, respectively. The $RMSE_{after}$ is expected to be higher in the deviation scenario when comparing it to the non-deviation scenario. For the $RMSE_{before}$, there is no expectation for it to be worse or better in the deviation scenario because the assumptions being deviated from pertain to the LiDAR calibration. Table 4-7 shows the evaluated accuracy and expected accuracy of this data. The evaluated accuracy represents the RMSE of the differences between the true coordinates and the noise-contaminated true coordinates, and it is denoted as $RMSE_{true}$. The expected accuracy is from error propagation and is very similar to the evaluated accuracy. To evaluate the results, the estimated biases will be compared to the simulated biases, and the RMSE of the adjusted and true coordinates will be compared to the accuracy values in Table 4-7. In addition to this, there is a *Percent Improvement* measure which quantifies the improvement in accuracy after calibration and it will be used to understand the impact of deviating from the assumptions. The ratio used to calculate this measure is shown in eq. (4.2). Using this measure, it can be concluded that if $RMSE_{after}$ is equal to $RMSE_{before}$, then the *Percent Improvement* will be 0, and if $RMSE_{after}$ is equal to $RMSE_{true}$, then the *Percent Improvement* will be 100.

Table 4-7: Evaluated Accuracy (RMSE of Differences between True & Bias-Free Coordinates) and Expected Accuracy (via Error Propagation) at Various Scan Angles

	Evaluated Accuracy ($RMSE_{true}$)	Expected Accuracy (Error Propagation)		
		0° scan angle	15° scan angle	30° scan angle
X (m) (across flight dir.)	0.096	0.112	0.110	0.101
Y (m) (along flight dir.)	0.100	0.108	0.116	0.136
Z (m)	0.105	0.102	0.105	0.113

$$Percent\ Improvement = \frac{(RMSE_{before} - RMSE_{after})}{(RMSE_{before} - RMSE_{true})} * 100 \quad (4.2)$$

4.3.2 Deviating from the Parallel Flight Lines Assumption

The \mathcal{S} calibration requires that the flight lines be parallel to each other for the calibration math model to be valid. Four different calibration tests were done using varying levels of deviation from being parallel (0°, 10°, 20°, and 30°) and resulting estimated biases are shown in Table 4-8. The angular deviation value represents the collective deviation of flight lines in a strip-pair, i.e. if there is a 10° deviation from being parallel it means that each flight line is individually deviated by 5°. In Table 4-8, it is observed that the results from the 0° deviation are similar to the simulated biases, and the estimations for the $\delta\Delta\mathbf{x}_b$, $\delta\Delta\mathbf{\kappa}_b$, and $\delta\mathcal{S}_b$ show a gradual increase in difference from the simulated values as the flight lines deviate further from being parallel.

Table 4-8: The Estimated \mathcal{S} Calibration Parameters with Parallel and Non-Parallel Flight Lines

Non-deviation		Deviation			
		0° Deviation	10° Deviation	20° Deviation	30° Deviation
Simulated Biases		Estimated Biases			
$\delta\Delta X_b$ (m):	0.200	0.205	0.237	0.259	0.282
$\delta\Delta Y_b$ (m):	0.200	0.189	0.188	0.186	0.197
$\delta\Delta\omega_b$ (°):	36.000	37.013	36.364	36.692	35.688
$\delta\Delta\phi_b$ (°):	36.000	35.993	34.704	33.053	31.300
$\delta\Delta\kappa_b$ (°):	36.000	34.653	37.735	45.743	51.379
$\delta\mathcal{S}_b$:	0.00100	0.00096	0.00080	0.00073	0.00055

The RMSE analysis of these four tests is shown in Table 4-9. The adjusted coordinates in the non-deviated and deviated scenarios are individually compared to the true coordinates, and the RMSE of each of those differences indicates the overall accuracy. For the test where there is 0° deviation from being parallel, the RMSE values after calibration meet the evaluated/expected accuracy of 10cm in Table 4-7. When compared to the before calibration, the after calibration RMSE values also show a *Percent Improvement* at or close to 100% for the test with 0° deviation. We can see that as the flight lines were deviated further from being parallel, the X coordinate accuracy consistently gets worse, the Y coordinate accuracy does not degrade, and the Z coordinate accuracy degrades but not as much as X . This pattern is expected and can be attributed to the degraded bias estimation in the lever arm in the across flight direction, $\delta\Delta x_b$, and the degraded estimation of the scan angle scale factor bias, $\delta\mathcal{S}_b$. The scan angle scale factor bias additionally affects the Z coordinate. Even in this non-ideal scenario of non-parallel flight lines, there is still a significant *Percent Improvement*. The 10° and 20° deviations show a 90-100 and 82-99 *Percent Improvement*, respectively, and even in the extreme case of 30° deviation there is a 61-95 *Percent Improvement*, showing that the *Simplified* calibration performs well in this non-ideal condition.

Table 4-9: RMSE Analysis of \mathcal{S} Calibration Results with Parallel and Non-Parallel Flight Lines

		Non-deviation		Deviation	
		0° Deviation	10° Deviation	20° Deviation	30° Deviation
RMSE_{before}	X(m)	0.575	0.521	0.511	0.458
					0.516
	Z(m)	0.26	0.254	0.255	0.231
RMSE_{after}					0.239
	Y(m)	0.099	0.101	0.106	0.121
					0.133
Percent Improvement	X(%)	100	90	82	61
					95
	Z(%)	97	91	88	75

4.3.3 Performance of the Quasi-Rigorous/Quasi-Simplified (*QRQS*) Calibration with Non-Parallel Flight Lines

In contrast to the \mathcal{S} calibration approach, the *QRQS* calibration approach does not have an assumption that the flight lines should be parallel. The results in Table 4-10 show the ability of the *QRQS* calibration approach to handle non-parallel flight lines. The results in Table 4-10 contrast the results shown in Table 4-9 where the estimated parameters from the \mathcal{S} calibration differ from the simulated parameters as flight lines are deviated from parallel. Furthermore, the RMSE analysis shown in Table 4-11 shows that the percent improvement values after the *QRQS* calibration for all non-parallel scenarios are within the 97-100% range, confirming that the *QRQS* calibration approach does effectively calibrate scenarios that have flight lines which are deviated from being parallel.

Table 4-10: The Estimated **QRQS** Calibration Parameters with Parallel and Non-Parallel Flight Lines

		Parallel	Non-Parallel		
		0° Deviation	10° Deviation	20° Deviation	30° Deviation
Simulated Biases		Estimated Biases			
$\delta\Delta X_b$ (m):	0.200	0.203	0.207	0.210	0.204
$\delta\Delta Y_b$ (m):	0.200	0.196	0.190	0.193	0.201
$\delta\Delta\omega_b$ (°):	36.000	36.215	35.201	35.817	36.504
$\delta\Delta\phi_b$ (°):	36.000	35.959	36.502	35.993	35.993
$\delta\Delta\kappa_b$ (°):	36.000	34.852	35.521	34.608	35.025
δS_b :	0.00100	0.00099	0.00099	0.00099	0.00099

Table 4-11: RMSE Analysis of **QRQS** Calibration Results with Parallel and Non-Parallel Flight Lines

		Parallel	Non-Parallel		
		0° Deviation	10° Deviation	20° Deviation	30° Deviation
RMSE_{before}	X(m)	0.575	0.575	0.573	0.572
					0.565
	Z(m)	0.26	0.265	0.268	0.265
RMSE_{after}					0.105
	Y(m)	0.100	0.101	0.100	0.096
					0.104
Percent Improvement	X(%)	100	100	99	99
					100
	Z(%)	97	98	98	98

4.3.4 Deviating from the Low Terrain Relief Assumption

To test the low terrain relief with respect to the flying height assumption from the \mathcal{S} approach, results from a scenario that follows the assumption (100m range in terrain elevation variation) were compared to one that does not (300m range in terrain elevation variation). The estimated biases are shown in Table 4-12 and it is observed that the test with low terrain relief results in estimated biases that are similar to the simulated ones, while the 300m range terrain relief test shows degraded estimation in several of the estimated biases.

Table 4-12: The Estimated \mathcal{S} Calibration Parameters Before and After Deviation from the Low Terrain Relief Assumption

	Non-deviation	Deviation
	100m Range Terrain Relief	300m Range Terrain Relief
Simulated Biases	Estimated Biases	
$\delta\Delta X_b$ (m): 0.200	0.205	0.230
$\delta\Delta Y_b$ (m): 0.200	0.189	0.116
$\delta\Delta\omega_b$ (°): 36.000	37.013	43.869
$\delta\Delta\phi_b$ (°): 36.000	35.993	37.437
$\delta\Delta\kappa_b$ (°): 36.000	34.653	24.910
$\delta\mathcal{S}_b$: 0.00100	0.00096	0.00132

Table 4-13 shows the RMSE analysis on the adjusted coordinates between these two scenarios. As expected, the RMSE after calibration in the 100m range case is at or below the 10cm evaluated/expected accuracy values in Table 4-7, and the *Percent Improvement* is close to 100. For the 300m range case, the RMSE after calibration is slightly larger than 10cm, and therefore we also see a lower *Percent Improvement* when compared to the scenario that follows the assumption. In conclusion, even when the terrain relief is not low with respect to the flying height, the after calibration RMSE improves by 87%-100%, showing that the calibration performs well in this non-ideal scenario.

Table 4-13: RMSE Analysis of the \mathcal{S} Calibration Procedure Before and After Deviation from the Low Terrain Relief Assumption

		Non-deviation	Deviation
		100m Range Terrain Relief	300m Range Terrain Relief
RMSE_{before}	X (m)	0.575	0.336
	Y(m)	0.565	0.453
	Z(m)	0.26	0.177
RMSE_{after}	X(m)	0.093	0.131
	Y(m)	0.099	0.094
	Z(m)	0.105	0.108
Percent Improvement	X(%)	100	87
	Y(%)	100	100
	Z(%)	97	90

When the terrain relief is not low with respect to the flying height, as is the case in the scenario with a 300m variation, it is observed that the lever arm bias in the flight direction, $\delta\Delta y$, the bias in the boresight pitch, $\delta\Delta\omega$, the bias in the boresight heading, $\delta\Delta\kappa$, and the bias in the scan angle scale factor, $\delta\mathcal{S}$, estimations are significantly different from their simulated values. This behavior is expected because the \mathcal{S} calibration math model does not account for high variation in the terrain. In Table 4-13, the after calibration RMSE of the X coordinate slightly increased due to the inaccurate bias estimations in the scan angle scale factor bias, $\delta\mathcal{S}$. The inaccurate bias estimations in the lever arm in the flight direction, $\delta\Delta y$, and the heading bias, $\delta\Delta\kappa$, both affect the Y coordinate accuracy, but a decreased accuracy is not observed for Y in Table 4-13 because their impacts have canceled each other out due to having a similar magnitude but the opposite sign. In conclusion, even though the terrain relief varies by 300m, the comparison of the RMSE values in Table 4-13 between the before and after calibration shows that the after calibration RMSE improves by 87%, 100%, and 90% for the X , Y , and Z coordinates, respectively.

4.3.5 Deviating from the Vertical Scanner Assumption

All three of the *Pseudo-rigorous* calibration approaches (*S*, *QR*, and *QRQS*) require the scanner to be vertical in order for the calibration math model to be valid. The tables below compare results from a vertical scanner to a non-vertical scanner (the platform pitch and roll were at 8° instead of $\sim 0^\circ$). For the *S*, *QR*, and *QRQS* approaches, Table 4-14, Table 4-16, and Table 4-18 show the estimated calibration parameters, respectively, for the vertical and non-vertical scenarios. In each of the three tables, a similar pattern is observed; namely, the estimated biases from the vertical scanner are very similar to the simulated biases and the non-vertical scanner estimated biases show a deviation from the simulated biases. In the lever arm biases, the $\delta\Delta y_b$ is impacted the most, and in the boresight biases, the $\delta\Delta\phi_b$ bias is impacted the most.

The RMSE analyses for the *S*, *QR*, and *QRQS* calibration approaches are shown in Table 4-15, Table 4-17, and Table 4-19, respectively. For the vertical scanner scenario in these tables, the after calibration RMSE is very close to the 10cm evaluated/expected accuracy, and the *Percent Improvement* is at or close to 100. For the non-vertical scenario, the after calibration RMSE value for the *X* coordinate accuracy is degraded, the *Y* coordinate accuracy does not degrade, and the *Z* coordinate accuracy degrades but not as much as *X*. As for the *Percent Improvement* in the non-vertical scenarios, Table 4-15 shows that it was 52%-100% for the *S* approach, Table 4-17 shows that it was 57%-99% for the *QR* approach, and Table 4-21 shows that it was 56%-100% for the *QRQS* approach. Although the performance of these approaches for the non-vertical scanner scenario is not ideal, there is still a significant improvement in the accuracy for all three of the *Pseudo-rigorous* calibration approaches.

Table 4-14: The Estimated \mathcal{S} Calibration Parameters Before and After Deviation from the Vertical Scanner Assumption

Non-deviation		Deviation	
		Vertical Scanner	Non-Vertical Scanner (pitch, roll=8°)
Simulated Biases		Estimated Biases	
$\delta\Delta X_b$ (m):	0.200	0.205	0.197
$\delta\Delta Y_b$ (m):	0.200	0.189	0.144
$\delta\Delta\omega_b$ (°):	36.000	37.013	40.289
$\delta\Delta\varphi_b$ (°):	36.000	35.993	2.785
$\delta\Delta\kappa_b$ (°):	36.000	34.653	33.539
δS_b :	0.00100	0.00096	0.00098

Table 4-15: RMSE Analysis of the \mathcal{S} Calibration Procedure Before and After Deviation from the Vertical Scanner Assumption

Non-deviation		Deviation	
		Vertical Scanner	Non-Vertical Scanner (pitch=8°, roll=8°)
$RMSE_{before}$	X(m)	0.575	0.478
			0.492
	Z(m)	0.26	0.286
$RMSE_{after}$	X(m)	0.093	0.283
	Y(m)	0.099	0.101
	Z(m)	0.105	0.133
Percent Improvement	X(%)	100	52
	Y(%)	100	100
	Z(%)	97	82

Table 4-16: The Estimated **QR** Calibration Parameters Before and After Deviation from the Vertical Scanner Assumption

Non-deviation		Deviation	
		Vertical Scanner	Non-Vertical Scanner (pitch=8°, roll=8°)
Simulated Biases		Estimated Biases	
$\delta\Delta X_b$ (m):	0.200	0.201	0.182
$\delta\Delta Y_b$ (m):	0.200	0.198	0.157
$\delta\Delta\omega_b$ (°):	36.000	35.959	40.139
$\delta\Delta\phi_b$ (°):	36.000	36.120	3.666
$\delta\Delta\kappa_b$ (°):	36.000	35.946	30.273
δS_b :	0.00100	0.00100	0.00100

Table 4-17: RMSE Analysis of the **QR** Calibration Procedure Before and After Deviation from the Vertical Scanner Assumption

		Non-deviation	Deviation
			Non-Vertical Scanner (pitch=8°, roll=8°)
RMSE_{before}	X(m)	0.575	0.478
			0.492
	Z(m)	0.26	0.286
RMSE_{after}			0.261
	Y(m)	0.099	0.102
			0.131
Percent Improvement	X(%)	100	57
			99
	Z(%)	97	83

Table 4-18: The Estimated **QRQS** Calibration Parameters Before and After Deviation from the Vertical Scanner Assumption

Non-deviation		Deviation	
		Vertical Scanner	Non-Vertical Scanner (pitch=8°, roll=8°)
Simulated Biases		Estimated Biases	
$\delta\Delta X_b$ (m):	0.200	0.203	0.189
$\delta\Delta Y_b$ (m):	0.200	0.196	0.161
$\delta\Delta\omega_b$ (°):	36.000	36.215	39.870
$\delta\Delta\varphi_b$ (°):	36.000	35.959	3.843
$\delta\Delta\kappa_b$ (°):	36.000	34.852	30.900
δS_b :	0.00100	0.00099	0.00100

Table 4-19: RMSE Analysis of the **QRQS** Calibration Procedure Before and After Deviation from the Vertical Scanner Assumption

Non-deviation		Deviation	
		Non-Vertical Scanner (pitch=8°, roll=8°)	
RMSE_{before}	X(m)	0.575	0.478
			0.492
	Z(m)	0.26	0.286
RMSE_{after}			0.267
	Y(m)	0.100	0.101
			0.131
Percent Improvement	X(%)	100	56
			100
	Z(%)	97	83

4.3.6 Investigating the Number of Control Points

The **QR**, **QRQS**, and **R** calibration approaches have the option to incorporate control, which is used to estimate the bias in the range measurement. The tables below compare the results that had 15 control points, versus results that had 100 control points. Table 4-20, Table 4-22, and Table 4-24 show the calibration results for the **QR**, **QRQS**, and **R** calibration approaches, respectively. The corresponding RMSE analysis are shown in Table 4-21, Table 4-23, and Table 4-25, respectively.

For the **QR** calibration, the results are shown in Table 4-20, and Table 4-21 shows the RMSE analysis of those results. For the **R** calibration, the results are shown in Table 4-24, and Table 4-25 shows the RMSE analysis of those results.

Table 4-20: **QR** Calibration Results While Varying the Number of Control Points

	15 Control Points	100 Control Points
Simulated Biases	Estimated Biases	
$\delta\Delta X_b$ (m): 0.200	0.205	0.211
$\delta\Delta Y_b$ (m): 0.200	0.196	0.194
$\delta\Delta\omega_b$ (°): 36.000	36.888	37.095
$\delta\Delta\phi_b$ (°): 36.000	36.423	36.498
$\delta\Delta\kappa_b$ (°): 36.000	34.703	35.425
δS_b : 0.00100	0.00099	0.00100
$\delta\Delta\rho_b$ (m): 0.300	0.314	0.305

Table 4-21: RMSE Analysis of **QR** Calibration Results While Varying the Number of Control Points

		15 Control Points	100 Control Points
RMSE_{before}	X(m)	0.597	0.598
	Y(m)	0.498	0.496
	Z(m)	0.246	0.239
RMSE_{after}	X(m)	0.092	0.092
			0.100
	Z(m)	0.107	0.105
Percent			100
	Y(%)	100	100
			96

Table 4-22: **QRQS** Calibration Results While Varying the Number of Control Points

		15 Control Points	100 Control Points
$\delta\Delta X_b$ (m):	0.200	0.206	0.208
$\delta\Delta\omega_b$ (°):	36.000	35.522	35.807
$\delta\Delta\kappa_b$ (°):	36.000	35.624	35.420
$\delta\Delta\rho_b$ (m):	0.300	0.316	0.304

Table 4-23: RMSE Analysis of *QRQS* Calibration Results While Varying the Number of Control Points

		15 Control Points	100 Control Points
<i>RMSE_{before}</i>	X(m)	0.596	0.598
	Y(m)	0.496	0.495
	Z(m)	0.242	0.236
<i>RMSE_{after}</i>	X(m)	0.092	0.092
	Y(m)	0.099	0.100
	Z(m)	0.107	0.105
Percent Improvement	X(%)	100	100
	Y(%)	100	100
	Z(%)	95	96

Table 4-24: *R* Calibration Results While Varying the Number of Control Points

		15 Control Points	100 Control Points
Simulated Biases		Estimated Biases	
$\delta\Delta X_b$ (m):	0.200	0.198	0.195
$\delta\Delta Y_b$ (m):	0.200	0.205	0.196
$\delta\Delta\omega_b$ (°):	36.000	35.084	36.654
$\delta\Delta\varphi_b$ (°):	36.000	35.817	35.941
$\delta\Delta\kappa_b$ (°):	36.000	37.136	37.136
δS_b:	0.00100	0.00101	0.00100
$\delta\Delta\rho_b$ (m):	0.300	0.296	0.308

Table 4-25: RMSE Analysis of **R** Calibration Results While Varying the Number of Control Points

		15 Control Points	100 Control Points
RMSE_{before}	X(m)	0.595	0.597
	Y(m)	0.496	0.496
	Z(m)	0.233	0.236
RMSE_{after}	X(m)	0.092	0.092
	Y(m)	0.100	0.100
	Z(m)	0.107	0.105
Percent Improvement	X(%)	100	100
	Y(%)	100	100
	Z(%)	95	96

Table 4-20 and Table 4-22 shows that the **QR** and **QRQS** calibration results do not significantly change between the case with 15 control points and the case with 100 control points. Similarly, it can be observed from the calibration results in Table 4-24 that the **R** calibration is not sensitive to the amount of control either. The RMSE results after calibration from the **QR**, **QRQS**, and **R** approaches meet the expected accuracy of 10cm (Table 4-7). When comparing the before RMSE with the after RMSE in Table 4-21 for the **QR**, Table 4-23 for the **QRQS**, and Table 4-25 for the **R**, the RMSE values improved by 100%, 100%, and 96% for the **X**, **Y**, and **Z** coordinates, respectively, after all calibration approaches.

4.3.7 Summary of Performance Tests

This series of tests on the individual *Pseudo-rigorous* approaches demonstrated that they are robust under non-ideal conditions, and a 52-100 *Percent Improvement* was observed even in the extreme cases. This demonstration is important because it allows one to see the capability of the calibration approaches to improve point cloud accuracy even when it is not possible to meet a certain assumption in the data collection phase.

4.4 Results of the Stability Analysis

The stability analysis should be performed throughout the lifespan of a LiDAR system in order to understand how the parameters vary over time and to establish the optimal calibration frequency for a specific LiDAR mapping system. The results shown here demonstrate how performing a stability analysis at different times is necessary in order to ensure consistent accuracy of derived point clouds. The data used here is the same data that was used in section 4.3 which was simulated by ray tracing techniques over terrain defined by a USGS DEM. The dates are hypothetical in order to demonstrate the developed strategy and the application of stability analysis as QA tool.

There results from the three different calibration implementations are shown in Table 4-26. The first implementation of the stability analysis will be between set-1 and set-2, and the second implementation of the stability analysis will be between set-1 and set-3.

Table 4-26: Calibration Results from Hypothetical Times

	Set-1	Set-2	Set-3
	Estimated Biases		
$\delta\Delta X_b$ (m):	0.20	0.18	0.28
$\delta\Delta Y_b$ (m):	0.22	0.20	0.18
$\delta\Delta\omega_b$ (°):	-0.33	-0.30	-0.47
$\delta\Delta\phi_b$ (°):	-0.24	-0.27	-0.19
$\delta\Delta\kappa_b$ (°):	0.02	0.01	-0.13
δS_b :	0.001	0.001	0.002
$\delta\Delta\rho_b$ (m):	0.33	0.33	0.35

4.4.1 Stable Stability Analysis Results

The RMSE results from the stability analysis between set-1 and set-2 calibration results are shown in Table 4-27. There were three strip-pairs used in total for these calibration results, and Table 4-28 shows a breakdown of the RMSE by individual strip-pair. In Table 4-27, the RMSE values do not exceed the error propagation results shown in Table 4-7 and therefore the system is considered to be stable at the time of the set-2 calibration. More specifically, any differences between the calibration results are not large enough to have impacted the final point cloud significantly.

Table 4-27: Stability Analysis RMSE Values of all Point Clouds from a Stable LiDAR System

Coordinate	RMSE of all Point Clouds
X(m)	0.018
Y(m)	0.014
Z(m)	0.017

Table 4-28: Stability Analysis RMSE Values of Individual Point Clouds from a Stable LiDAR System

Strip-pair	Coordinate	RMSE of Point Cloud A	RMSE of Point Cloud B
1	X(m)	0.011	0.011
	Y(m)	0.016	0.013
	Z(m)	0.009	0.008
2	X(m)	0.011	0.027
	Y(m)	0.016	0.012
	Z(m)	0.009	0.026
3	X(m)	0.027	0.011
	Y(m)	0.012	0.017
	Z(m)	0.026	0.009

4.4.2 Unstable Stability Analysis Results

The RMSE results from the stability analysis between set-1 and set-3 calibration results are shown in Table 4-29, and Table 4-30 shows a break down of the RMSE by individual strip-pair. In Table 4-29, the Y coordinate RMSE value exceed the error propagation results shown in Table 4-7, and therefore the system is considered to be unstable at the time of the set-3 calibration.

Table 4-29: Stability Analysis RMSE Values of all Point Clouds from an Unstable LiDAR System

Coordinate	RMSE of all Point Clouds
X(m)	0.081
Y(m)	0.140
Z(m)	0.041

Table 4-30: Stability Analysis RMSE Values of Individual Point Clouds from an Unstable LiDAR System

Strip-pair	Coordinate	RMSE of Point Cloud A	RMSE of Point Cloud B
1	X(m)	0.085	0.095
	Y(m)	0.098	0.095
	Z(m)	0.017	0.018
2	X(m)	0.081	0.075
	Y(m)	0.126	0.158
	Z(m)	0.017	0.069
3	X(m)	0.074	0.079
	Y(m)	0.157	0.136
	Z(m)	0.067	0.017

Comparing the results from set-1, set-2, and set-3 with the stability analysis tool provides a way to define the optimal calibration period and essentially illustrates the process of utilizing the developed stability analysis strategy as a QA tool. Given the knowledge that the LiDAR system is stable between set-1 and set-2, but not stable between set-1 and set-

3, the optimal calibration frequency would be the timeframe that spanned between set-1 and set-2.

5. CONCLUSIONS, CONTRIBUTIONS, AND RECOMMENDATIONS FOR FUTURE WORK

5.1 Research Conclusions

This dissertation focuses on airborne LiDAR system calibration and the development of a new *Quasi-Rigorous/Quasi-Simplified* approach which simultaneously addresses the many challenges in LiDAR calibration, as well as the development of a stability analysis strategy for LiDAR calibration. In addition to these developments there is a performance assessment on the *Quasi-Rigorous/Quasi-Simplified* and existing approaches in non-ideal scenarios.

The experimental results for the *Quasi-Rigorous/Quasi-Simplified* approach compares it to *rigorous* approaches which are used when all raw measurement available, as well as *pseudo-rigorous* approaches which synthesize the raw measurements when there is a full or partial absence of raw measurements. After inspecting the point cloud alignment and adjusted coordinates against *rigorous* approaches using data collected from a UAV platform, it was shown that the *Quasi-Rigorous/Quasi-Simplified* approach is successful in significantly reducing the impact of systematic errors even though it makes several assumptions. Furthermore, it was demonstrated that the *Quasi-Rigorous/Quasi-Simplified* approach is suitable for calibration in the full absence of raw measurements, and when compared to the existing *Simplified* and *Quasi-Rigorous pseudo-rigorous* approaches it provides maximum capability while maintaining minimal assumptions and no requirements for raw measurements. Using simulated data, the performance analysis on the new and existing *pseudo-rigorous* approaches demonstrated that the *pseudo-rigorous* approaches (*Simplified*, *Quasi-Rigorous*, and *Quasi-Rigorous/Quasi-Simplified*) are robust under non-ideal conditions that deviate from their assumptions, and a 52-100 *Percent Improvement* after calibration was observed even in the extreme cases.

In the experimental results showing the application of the stability analysis strategy, it was demonstrated with simulated data how to use the strategy as a Quality Assurance tool for

consistently producing accurate point clouds throughout the lifespan of a LiDAR mapping system. This section performed a stability analysis twice between three sets of calibration results from the same LiDAR system. After quantifying the impact of the variation in system parameters on the point cloud it was determined that the system is stable between set-1 and set-2 but unstable between set-1 and set-3, and with this information one would set the optimal calibration frequency to be the time spanned between set-1 and set-2.

In addition to the development of the *Quasi-Rigorous/Quasi-Simplified* approach and the strategy for stability analysis, the new calibration approach, and previous *pseudo-rigorous* calibration approaches, were successfully used to calibrate a multi-beam spinning LiDAR (VLP-16). This has not previously been done since the *pseudo-rigorous* calibration methods are developed specifically for single-beam linear scanning LiDAR systems.

5.2 Research Contributions

The most prominent contribution of this dissertation is the development of the *Quasi-Rigorous/Quasi-Simplified* LiDAR system calibration approach. This new approach is generic for many types of users and holds the following characteristics:

- Operates without access to raw measurements,
- Uses point primitives to preserve the link to the sensor model,
- Has an automated procedure that accounts for the irregularity of LiDAR point clouds,
- Has a reliance on overlapping strips instead of expensive control surfaces,
- Is ground cover independent (does not require urban settings with various geometric shapes from buildings and other man-made features),
- Estimates all system parameters; which includes both the linear and angular mounting parameters as well as the internal characteristics of the LiDAR unit, and
- Able to incorporate control into the calibration math model.

To summarize this, Table 5-1 scores the rigor of this new calibration approach, as well as the existing *rigorous* approach proposed by Kersting (2011) and *pseudo-rigorous* approaches proposed by Bang (2010). Then, the scores are shown in the graph of Figure 5.1 which demonstrates how the *Quasi-Rigorous/Quasi-Simplified* maintains the maximum rigor of the existing *pseudo-rigorous* approaches while having less requirements. In conclusion, the *Quasi-Rigorous/Quasi-Simplified* LiDAR system calibration approach has the necessary rigor (by preserving the link to the sensor model) and generality in terms of data availability and type of terrain used (urban or non-urban) for the wide range of users in the LiDAR community.

Table 5-1: Calibration Rigor Score of Existing Calibration Approaches (Red) and the New *Quasi-Rigorous/Quasi-Simplified* Approach (Blue)

	Can Incorporate Control	Can Handle any type of Terrain	1-Step Process	Does not Synthesize Measurements	Rigor Score
Simplified	0	0	0	1	1
Quasi-Rigorous	1	1	1	0	3
Rigorous	1	1	1	1	4
Quasi-Rigorous/ Quasi-Simplified	1	1	1	0	3

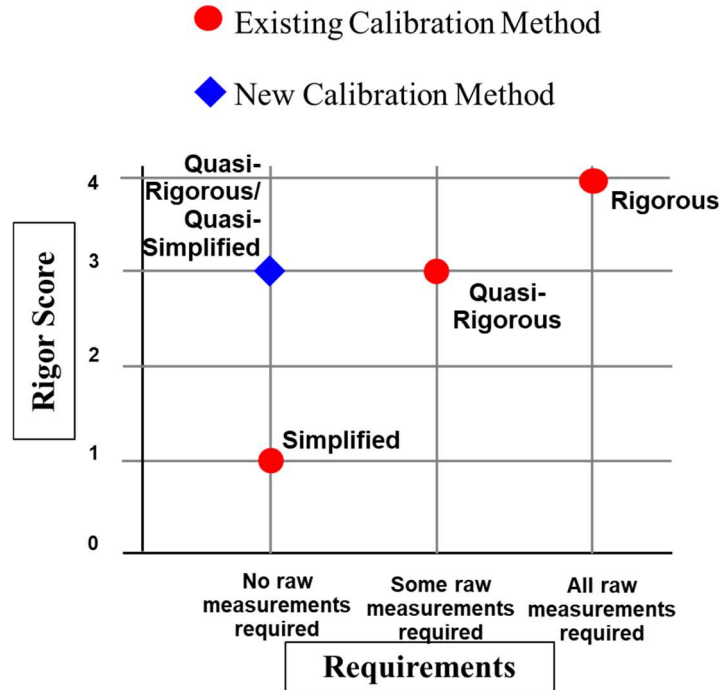


Figure 5.1: Requirements vs Rigors Score of the New and Existing Calibration Methods

Another contribution of this work is in the performance assessment of the new and existing *pseudo-rigorous* approaches under non-ideal conditions. In each of the non-ideal conditions there is a deviation from one of the underlying assumptions pertaining to the *pseudo-rigorous* calibration math models. This assessment demonstrates that the *pseudo-rigorous* approaches can significantly improve point cloud accuracy even when all assumptions are not met. More specifically, the performance assessment individually inspects each assumption deviation with the following tasks:

- Side by side comparison of the estimated system parameters/biases before and after deviating from the specific assumption,
- RMSE of the difference between the resulting point cloud coordinates and true coordinates for the following 4 cases:
 - Non-deviated, before calibration,
 - Non-deviated, after calibration,
 - Deviated, before calibration,
 - Deviated, after calibration, and

- Quantify the percent improvement after calibration for the non-deviated and deviated scenario to understand the impact that the non-ideal scenario has on the ability of the calibration algorithm to improve the accuracy of the data.

The final contribution of this dissertation is in the development of a stability analysis strategy. The stability analysis strategy is an important contribution because LiDAR mapping systems are no longer considered a commodity and are being used more often and for more types of engineering projects. The stability analysis strategy serves as a QA tool for consistent production of accurate point clouds over the lifespan of a LiDAR mapping system. The developed stability analysis strategy has the following characteristics:

- Quantifies variation of system parameters over time,
- Guides the process of determining optimal calibration frequency, and
- Operates with or without access to raw measurements (by synthesizing the measurements in the latter case).

5.3 Recommendations for Future Work

Recommendations for future work related to the LiDAR system calibration and the specific research done here are as follows:

- The *Quasi-Rigorous/Quasi-Simplified* calibration approach could be tested with other types of real data, such as data from a high-altitude LiDAR mapping system.
- The *Quasi-Rigorous/Quasi-Simplified* approach could be expanded to handle multi-LiDAR systems.
- The *Quasi-Rigorous/Quasi-Simplified* approach could be expanded to simultaneously adjust GPS/INS errors along with the determination of system parameters. This would entail modelling the full variance-covariance matrix to appropriately represent correlations/decorelations over time.

- The *Pseudo-rigorous* approaches could be tested with various real datasets that deviate from their assumptions.
- The stability analysis strategy developed for airborne LiDAR systems could be tested and validated with various real datasets. This should include defining the optimal calibration frequency for low-altitude and high-altitude systems, as well as systems with industrial and consumer grade lasers.
- The stability analysis strategy could be extended to include terrestrial based applications such as mobile mapping.
- A stability analysis for multisensor systems could be developed.

REFERENCES

- Alharthy, A., Bethel, J., and Mikhail, E., 2004. Analysis and accuracy assessment of airborne laser-scanning system, *International Archives of the Photogrammetry, Remote Sensing and Spatial Information Sciences*, 35(B2): 144–149.
- Baltsavias, E.P., 1999. Airborne laser scanning - basic relations and formulas, *ISPRS Journal of Photogrammetry and Remote Sensing*, Vol. 54, No. 2-3, pp. 199-214.
- Bang, K.I., Habib, A.F., Kersting, A., 2010. Estimation of Biases in LiDAR System Calibration Parameters Using Overlapping Strips, *The Canadian Journal of Remote Sensing*, (accepted 2010).
- Bang, K., 2010. *Alternative Methodologies for LiDAR System Calibration*, Ph.D. dissertation, Department of Geomatics Engineering, University of Calgary, Canada, 160 p.
- Bretar, F., Pierrot-Deseilligny, M., Roux, M., 2004. Solving the strip adjustment problem of 3D airborne LiDAR data, *Proceedings of the IEEE IGARSS*, pp. 4734-4737, 2004-Sep. 20-24.
- Burman, H., 2002. Laser strip adjustment for data calibration and verification, *Photogrammetric Computer Vision (ISPRS Commission III Symposium)*, 9-13 September, Graz, Austria. Vol. 34, No. 3, A-67-72.
- Coren, F., and P. Sterzai, 2006. Radiometric correction in laser scanning, *International Journal of Remote Sensing*, 27(15):3097–3014.
- Crombaghs, M.J.E., Brügelmann, R., and Min E.J. de, 2000. On the adjustment of overlapping strips of laser altimeter height data, *International Archives of Photogrammetry and Remote Sensing*, 16-22 July, Amsterdam, the Netherlands. pp. 230-237.
- Csanyi, N., Toth, C., 2007. Improvement of LiDAR data accuracy using LiDAR-specific ground targets, *Photogrammetric Engineering and Remote Sensing*, Vol. 73, No. 4, pp. 385-396.
- Csanyi, N., 2008. *A Rigorous Approach to Comprehensive Performance Analysis of State-of-the-Art Airborne Mobile Mapping Systems*, Ph.D. dissertation, The Ohio State University, 217 p.

- Dolloff, J.T., (2013). The full multi-state vector error covariance matrix: Why needed and its practical representation, *Proceedings of the SPIE*, Volume 8747, id. 874702 18 p.
- Filin, S., 2001. *Calibration of Spaceborne and Airborne Laser Altimeters Using Natural Surfaces*, Ph.D. dissertation, Department of Civil and Environmental Engineering and Geodetic Science, the Ohio-State University, Columbus, OH, 129 p.
- Filin, S., Vosselman, G., 2004. Adjustment of airborne laser altimetry strips, *International Archives of Photogrammetry, Remote Sensing and Spatial Information Sciences*, vol. B3, pp. 285-289.
- Friess, P., 2006. Toward a rigorous methodology for airborne laser mapping, *Proceedings of EuroCOW*, Castelldefels, Spain, unpaginated CD-ROM.
- Ghanma, M., 2006. *Integration of Photogrammetry and LiDAR*, Ph.D. Dissertation, Department of Geomatics Engineering, the University of Calgary, Calgary, Canada.
- Glennie, C., 2007. Rigorous 3D error analysis of kinematic scanning LiDAR systems, *Journal of Applied Geodesy*, Vol. 1, No. 3, pp. 147-157.
- Habib, A., Pullivelli, A., and Morgan, M., 2005. Quantitative Measures for the Evaluation of Camera Stability. *Optical Engineering* 44(3) 033605(8 pages), March 2005.
- Habib, A.F., Cheng, R.W.T., Kim, E.M., Mitishita, E.A., Frayne, R., and Ronsky, J.L., 2006. Automatic surface Matching for the registration of LiDAR data and MR imagery, *ETRI Journal*, Vol. 28, No. 2, pp. 162-174.
- Habib, A. F., Kersting, A. P., Ruifang, Z., Al-Durgham, M., Kim, C., and Lee, D. C., 2008. LiDAR strip adjustment using conjugate linear features in overlapping strips. *International Archives of Photogrammetry, Remote Sensing and Spatial Information Sciences*, 3-11 July, Beijing, China. Vol. XXXVII, Part B1, pp. 385–390.
- Habib, A. F., Bang, K.I., Kersting, A., and Lee D.C., 2009a. Error budget of LiDAR systems and quality control of the derived data, *Photogrammetric Engineering and Remote Sensing*, Vol. 75, No. 9, pp. 1093-1108.

- Habib, A. F., Kersting, A., Bang, K.I., Zhai, R., and Al-Durgham, M., 2009b. A strip adjustment procedure to mitigate the impact of inaccurate mounting parameters in parallel LiDAR strips, *The Photogrammetric Record*, Vol 24, No. 126, pp. 171-195.
- Habib, A., A. P. Kersting, K. Bang, and D. C. Lee, 2010a. Alternative methodologies for the internal quality control of parallel LiDAR strips, *IEEE Transactions on Geoscience and Remote Sensing*, 48(1): 221–236.
- Habib A., K. Bang, A. P. Kersting, and J. Chow, 2010b. Alternative Methodologies for LiDAR System Calibration, *Remote Sensing*, 2(3): 874–907.
- Habib, A., Bang, K., Kersting, A. 2010c. Impact of LiDAR System Calibration on the Relative and Absolute Accuracy of Adjusted Point Cloud, *Proceedings of the 2010 European Calibration and Orientation Workshop*, (EuroCOW), Castelldefels, Spain, February 10 – 12, 2010.
- Habib A., Datchev, I. & Bang, K., 2010d. A Comparative Analysis of Two Approaches for Multiple Surface Registration of Irregular Point Clouds. *International Archives of the Photogrammetry, Remote Sensing and Spatial Information*, XXXVIII (Part 1).
- Habib, A., Kersting, A., Shaker, A., Yan, W., 2011. Geometric Calibration and Radiometric Correction of LiDAR Data and their Impact on the Quality of Derived Products, *Sensors*, Vol. 67, No. 9, pp. 9069-9097.
- Habib, A., Datchev, I., and Kwak, E., 2014. Stability Analysis for a Multi-Camera Photogrammetric System. *Sensors* 2014, 14, pp. 15084-15112; doi: 10.3390/s140815084.
- Habib, A. F., 2015. *Laser Scanning (CE 597)*, Course Notes of Department of Geomatics Eng., Purdue University, United States.
- Habib, A., & Lin, Y. J. (2016). Multi-class simultaneous adaptive segmentation and quality control of point cloud data. *Remote Sensing*, 8(2), 104.
- Habib, Ayman & Lin, Y-J & Lari, Zahra. (2017). Geometric Processing: Active Sensor Modeling and Calibration (LiDAR). *Reference Module in Earth Systems and Environmental Sciences*. 10.1016/B978-0-12-409548-9.10335-5.

- Hamza, E. and Habib, A., 2013. Smart Identification of Overlapping Strip Pairs/Regions for Optimized LiDAR System Calibration. International Conference on Aerospace Sciences and Navigation Technology, Egypt, May 21st – 25th, 2013.
- Hodgson, M. E., Bresnahan, P., 2004. Accuracy of airborne LiDAR derived elevation: Empirical assessment and error budget, *Photogrammetric Engineering and Remote Sensing*, Vol. 70, No. 3, pp. 331-339.
- Huising, E.J. and Gomes Pereira, L.M. G., 1998. Errors and accuracy estimates of laser data acquired by various laser scanning systems for topographic applications, *ISPRS Journal of Photogrammetry and Remote Sensing*, Vol. 53, No. 5, pp. 245-261.
- Kager, H. and K. Kraus, 2001. Height Discrepancies between Overlapping Laser Scanner Strips, *Optical 3-D Measurement Techniques V* (A. Grün and H. Kahmen, editors), Vienna, Austria, pp.103–110.
- Kager, H., 2004. Discrepancies between overlapping laser scanning strips - simultaneous fitting of aerial laser scanner strips, *International Archives of Photogrammetry, Remote Sensing and Spatial Information Sciences*, Vol. 35, Part B1, pp. 555–560.
- Kersting, A., 2011. *Quality Assurance of Multi-Sensor Systems*, Ph.D. dissertation, Department of Geomatics Engineering, University of Calgary, Canada, 265 p.
- Kersting, A., Habib, A., K. Bang, Skaloud, J., and 2012. Automated Approach for Rigorous Light Detection and Ranging System Calibration without Preprocessing and Strict Terrain Coverage Requirements, *Optical Engineering*, 51(7), pp.076201-1.
- Lichti, D., Habib, A., Detechev, I., 2009. An Object-Space Simulation Method for Low-Cost digital Camera Stability Testing. *Photogrammetric Engineering and Remote Sensing Journal*, vol. 75, no. 12, pp. 1407 – 1414.
- Maas H. G., 2002. Approach for measuring height and planimetry discrepancies in airborne laserscanner data, *Photogrammetric Engineering and Remote Sensing*, 68(9):933–940.
- May, N. C. and Toth, C. K., 2007. Point positioning accuracy of airborne lidar systems: a rigorous analysis, *International Archives of Photogrammetry, Remote Sensing and Spatial Information Sciences*, Vol. 36, Part 3/W49B, pp. 107-111, 2007.

- McGlone, J.C., Mikhail, E.M., Bethel, J., and Mullen, R., 2004. *Manual of Photogrammetry (5th Edition)*, American Society for Photogrammetry and Remote Sensing, Bethesda, US, 1151p.
- Mikhail, E. M. and Ackerman, F., 1976. *Observations and Least Squares*, University Press of America, Lanham, US, 497p.
- Morin, K.W., 2002. Calibration of Airborne Laser Scanners, M.S. thesis, Department of Geomatics Engineering, the University of Calgary, Calgary, Canada.
- Pfeifer, N., Elberink, S. O., Filin, S., 2005. Automatic tie elements detection for laser scanner strip adjustment", *Int. Arch. Photogrammetric Remote Sensing*, vol. 36, pp. 1682-1750.
- Rodarmel, C., Lee, M., Gilbert, J., Wilkinson, B., Theiss, H., Dolloff, J., O'Neill, C., 2015. The Universal LiDAR Error Model, *Photogrammetric Engineering and Remote Sensing*, 81(7):543–556.
- Ravi R., Shamseldin T., Elbahnasawy M., Lin Y-J, Habib A. Bias Impact Analysis and Calibration of UAV-Based Mobile LiDAR System with Spinning Multi-Beam Laser Scanner. *Applied Sciences*. 2018; 8(2):297.
- Shan, J. and Toth, C. K., 2009. *Topographic Laser Ranging and Scanning*, CRC Press, Boca Raton, US, 590p.
- Skaloud, J., 1999. *Optimizing Georeferencing of Airborne Survey Systems by INS/DGPS*, Ph.D. dissertation, Department of Geomatics Engineering, University of Calgary, Calgary, Canada, 179 p.
- Skaloud, J. and Lichti, D., 2006. Rigorous approach to boresight self-calibration in airborne laser scanning, *ISPRS Journal of Photogrammetry and Remote Sensing*, Vol. 61, No. 6, pp. 47-59.
- Toth, C. K., 2002. Calibrating airborne LiDAR systems, *Proceedings of ISPRS Commission II Symposium*, 20-23 August, Xi'an, China, pp. 475-480.
- Vosselman, G., 2002. Strip offset estimation using linear features, *Proceedings of the 3rd Int. Workshop Mapping Geo-Surficial Processes Using Laser Altimetry*, pp. 1-9, 2002-Oct.7-9.

- Wang, M. and Tseng, Y. H., 2004. LiDAR data segmentation and classification based on octree structure, *XXth International Society for Photogrammetry and Remote Sensing (ISPRS) Congress*, Istanbul, Turkey
- Wehr, A. and Lohr, U., 1999. Airborne laser scanning - an introduction and overview, *ISPRS Journal of Photogrammetry and Remote Sensing*, Vol. 54, No. 2-3, pp. 68-82.
- Wotruba, L., Morsdorf, F., Meier, E., Nuesch, D., 2005. Assessment of sensor Empirical characteristics of an airborne laser scanner using geometric reference targets, *Proceedings of the ISPRS Working Group III/3 Workshop Laser Scanning*, vol. 36, pp. 1-6.